TOPICAL REVIEW • OPEN ACCESS

The ELI-ALPS facility: the next generation of attosecond sources

To cite this article: Sergei Kühn *et al* 2017 *J. Phys. B: At. Mol. Opt. Phys.* **50** 132002

OPEN ACCESS
IOP Publishing
Journal of Physics B: Atomic, Molecular and Optical Physics
J. Phys. B: At. Mol. Opt. Phys. **50** (2017) 132002 (39pp)
https://doi.org/10.1088/1361-6455/aa6ee8

Topical Review

The ELI-ALPS facility: the next generation of attosecond sources

Sergei Kühn[1], Mathieu Dumergue[1], Subhendu Kahaly[1], Sudipta Mondal[1], Miklós Füle[1], Tamás Csizmadia[1], Balázs Farkas[1], Balázs Major[1], Zoltán Várallyay[1], Eric Cormier[1], Mikhail Kalashnikov[1], Francesca Calegari[2,3,4], Michele Devetta[2], Fabio Frassetto[5], Erik Månsson[2], Luca Poletto[5], Salvatore Stagira[2,6], Caterina Vozzi[2], Mauro Nisoli[2,6], Piotr Rudawski[7], Sylvain Maclot[7], Filippo Campi[7], Hampus Wikmark[7], Cord L Arnold[7], Christoph M Heyl[7], Per Johnsson[7], Anne L'Huillier[7], Rodrigo Lopez-Martens[1,8], Stefan Haessler[8], Maïmona Bocoum[8], Frederik Boehle[8], Aline Vernier[8], Gregory Iaquaniello[8], Emmanuel Skantzakis[9], Nikos Papadakis[9], Constantinos Kalpouzos[9], Paraskevas Tzallas[1,9], Franck Lépine[1,10], Dimitris Charalambidis[1,9], Katalin Varjú[1], Károly Osvay[1] and Giuseppe Sansone[1,2,6,11]

[1] ELI-ALPS, ELI-Hu Kft., Dugonics tér 13, H-6720 Szeged Hungary
[2] Institute of Photonics and Nanotechnologies (IFN)–Consiglio Nazionale delle Ricerche (CNR), Piazza Leonardo da Vinci 32, I-20133 Milano, Italy
[3] Center for Free-Electron Laser Science, DESY, Notkestr. 85, 22607 Hamburg, Germany
[4] Physics Department, University of Hamburg, Luruper Chaussee 149, 22761 Hamburg, Germany
[5] Institute of Photonics and Nanotechnologies (IFN)–Consiglio Nazionale delle Ricerche (CNR), Via Trasea 7, I-35131 Padova, Italy
[6] Dipartimento di Fisica Politecnico di Milano, Piazza Leonardo da Vinci 32, I-20133 Milano, Italy
[7] Department of Physics, Lund University, 221 00 Lund, Sweden
[8] Laboratoire d'optique Appliquée, ENSTA, ParisTech, CNRS École Polytechnique, Université Paris-Saclay, 828 bd des Marchaux F-91762 Palaiseau Cedex, France
[9] Foundation for research and Technology Hellas (FORTH-IESL) PO Box 1385, 711 10 Heraklion, Greece
[10] Institut Lumière Matière, Université Lyon 1, CNRS, UMR 5306, 10 rue Ada Byron, F-69622 Villeurbanne Cedex, France
[11] Physikalisches Institut, Albert-Ludwigs-Universität Freiburg, Stefan-Meier-Str. 19, D-79104 Freiburg, Germany

E-mail: giuseppe.sansone@eli-alps.hu

Received 28 December 2015, revised 27 February 2017
Accepted for publication 24 April 2017
Published 13 June 2017

Abstract

This review presents the technological infrastructure that will be available at the Extreme Light Infrastructure Attosecond Light Pulse Source (ELI-ALPS) international facility. ELI-ALPS will offer to the international scientific community ultrashort pulses in the femtosecond and attosecond domain for time-resolved investigations with unprecedented levels of high quality characteristics. The laser sources and the attosecond beamlines available at the facility will make attosecond technology accessible for scientists lacking access to these novel tools. Time-resolved

investigation of systems of increasing complexity is envisaged using the end stations that will be provided at the facility.

Keywords: attosecond physics, ultrafast phenomena, generation of attosecond pulses, application of extreme ultraviolet radiation

(Some figures may appear in colour only in the online journal)

1. Introduction

Resolving dynamical processes in time and observing complex structures in space are two fundamental approaches to understanding the internal evolution and fundamental constituents of physical, chemical and biological systems. The time-resolved observation of physical phenomena is a key approach to understanding the correlation between different degrees of freedom in a system. The pioneering work of Muybridge [1] started the quest for technological tools to resolve dynamical processes occurring on ever shorter timescales. This has driven impressive technological developments, culminating with the development of femtosecond (1 fs $= 10^{-15}$ s) laser pulses at the end of the twentieth century. These pulses have been used to investigate the dynamics of atoms in molecular systems, and the scientific relevance of these achievements was recognized by awarding the Nobel prize to Ahmed Zewail for the foundation of femtochemistry [2].

The attosecond domain (1 as $= 10^{-18}$ s) [3] is the current frontier for reliable reproducible time-based events. This domain classically corresponds to the timescale of electronic motion within an atom, and in quantum mechanics the attosecond timescale is the typical timescale on which dynamics of coherent superpositions of broadband electronic wave packets evolve in the core and valence shells. The possibility to excite and probe the dynamics of such wave packets is linked to the availability of trains and isolated attosecond laser pulses, which can be generated by high-order harmonic generation (HHG)—either in gases or on solid surfaces. The applications of these pulses in pioneering experiments in atoms [4], molecules [5] and surfaces [6] have shown that the observation of electronic dynamics on the attosecond timescale can have a potentially large impact in understanding and controlling electronic correlation processes in simple systems [7], ultrafast charge migration in molecules [8, 9], and signal processing at an unprecedented speed [10]. The technology enabling these investigations still remains very challenging, and access is limited to the ultrafast laser community [11, 12]. However, time-resolved experiments of ever increasingly complex systems for fundamental research purposes and the intertwined potential technological impact calls for a more widespread use and easy access to attosecond technology, in particular for scientific communities such as chemists, biochemists, condensed matter physicists and, more generally, materials scientists.

The primary mission of the *Extreme Light Infrastructure Attosecond Light Pulse Source* (ELI-ALPS) facility in Szeged, Hungary is to provide the international scientific community with attosecond sources beyond the current state-of-the-art in terms of repetition rate, intensity and reliability. This will be realised by using novel primary laser sources having unprecedented characteristics in terms of average power, pulse duration and repetition rate. These primary sources will drive high-order harmonic generation in gases and on solid surfaces, and will deliver attosecond light pulses in the extreme ultraviolet (XUV) and soft x-ray region at high repetition rates and high intensities. pump–probe capabilities using these pulses and a fraction of the driving fields will be offered with temporal synchronization in the attosecond regime. The scaling of well established approaches, and novel schemes and targets will be investigated to generate attosecond pulses. The application of such pulses for a large community of specialists and non-experts will be made available at the facility by means of permanently installed end stations, and will facilitate experiments on atoms, molecules, complex structures, and solid and liquid interfaces.

This review presents the new primary laser sources that will be installed at ELI-ALPS in section 2. In section 3, the secondary sources, which will be driven by the primary laser sources for the generation of trains and isolated attosecond pulses by HHG in gases or on surfaces will be reviewed in detail. The application of the primary as well as secondary radiation will be briefly discussed in section 4, along with the user end stations that will be operational at the facility. Conclusions will be presented in section 5.

2. Primary sources at ELI-ALPS

The research infrastructure at ELI-ALPS is based on four main laser sources: three operating in the 100 W average power regime in the near-infrared (IR), and one at 15 W in the mid-IR (MIR). These systems, operating at different repetition rates and peak powers, are designed to deliver pulses with unique parameters—e.g. unmatched fluxes and extreme bandwidths—yet to provide stable and reliable operation so that the facility can perform frontier research in attophysics as well as serving the user community. The specifications of the lasers, especially their ultrabroad bandwidth, high peak power and high stability, have induced a strong change of paradigm in laser front end architecture. None of the laser systems are based on Kerr-lens mode-locked titanium-sapphire (Ti:Sa) oscillators and regenerative amplifiers. Instead, sub-ps fiber oscillators are employed, and the resultant pulses are then amplified in fibers, generating white light pulses, which exhibit passive carrier-envelope phase (CEP) stability. Such solutions are combined with very extensive and sophisticated engineering so that all systems are able to run continuously for at least eight hours on a daily basis.

Table 1. Parameters of the HR laser system in phase 1 and phase 2.

Parameters	HR 1	HR 2 (targeted)
Center wavelength λ_c	1030 nm	1030 nm
Repetition rate	100 kHz	100 kHz
Average power	>100 W	>500 W
Pulse energy	>1 mJ	>5 mJ
Pulse duration (@λ_c)	<6.2 fs (<1.85 cycles)	<6.2 fs (<1.85 cycles)
Output energy stability	<0.8% (rms)	<0.8% (rms)
Beam quality (Strehl ratio)	>0.9	>0.9
CEP stability	<100 mrad (rms)	<100 mrad (rms)
Beam pointing instability	<2.5% (diffr. limited div.)	<2.5%
Trouble-free uninterrupted operation	>8 h	>8 h

All laser systems will be run from their own oscillator and front end. Sub-fs accuracy timing will be provided by synchronizing the oscillators to the facility clock along with direct timing of the amplified pulses at the target through balanced optical cross correlators. The high repetition rate (HR) system is designed to run with coherently combined fiber lasers and non-linear optical pulse compressors, offering TW peak power from <6 fs pulses at 100 kHz. The system will feed the gas high-harmonic sources with sub-cycle controlled laser pulses (1 mJ, sub-6 fs) from late 2017. The ultimate specification will be available for attosecond source developers by the end of 2019.

The 1 kHz repetition rate single cycle (SYLOS) system has been generating 4.5 TW, sub-10 fs pulses since late 2016, and will serve the future XUV and soft x-ray attosecond pulse sources based on high-harmonic generation from gaseous and solid targets. The performance of SYLOS will be upgraded in two steps over two years to 20 TW peak power at sub-6 fs, whilst maintaining a CEP stability better than 250 mrad.

The petawatt power class laser has two arms. The first arm (HF-PW, high field petawatt) is the high field (HF) laser, which will deliver sub-20 fs optical pulses of 2 PW peak power with ultra-high temporal contrast (C $\sim 10^{11}$) at 10 Hz by mid 2019. The second arm (HF-100, high field 100 Hz) provides a reduced peak power (50 TW) but at a higher repetition rate (100 Hz). The HF laser sources will enable research on novel attosecond sources going beyond the keV photon level, which can be based on surface harmonics as well as Thomson scattering. These lasers would also facilitate regional radiobiological research with ion beams.

2.1. High repetition rate laser system

The HR laser is an optical fiber based system that operates at 100 kHz repetition rate and delivers pulses with sub-2 cycle duration at 1 mJ (phase 1, June 2017) and 5 mJ (phase 2, late 2018). The HR laser system relies on optical fiber technology [13, 14] featuring coherent combination [15] with subsequent non-linear compression [16, 17], which enables highly efficient amplification and compression to TW pulse peak powers

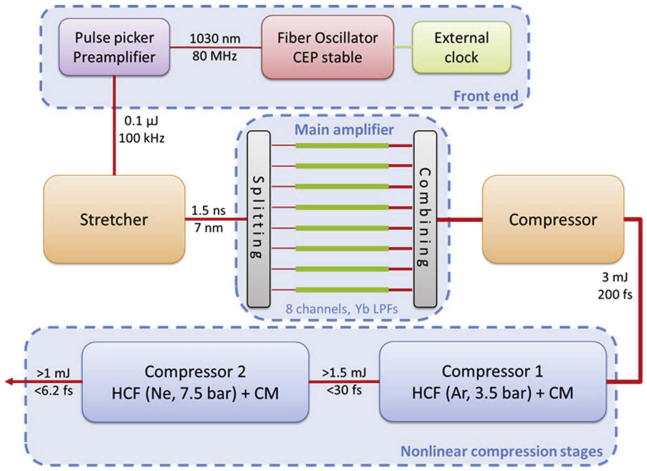

Figure 1. Scheme of the HR laser system with three major subsystems: the front end, the main amplifier and the non-linear compression stages. (CM: chirped mirror stage).

centered around 1030 nm [18]. The primary application of this laser system is in gas higher harmonic generation (GHHG), in order to achieve high quality, coherent attosecond pulses in the XUV spectral region. The expected parameters of the HR laser in phase 1 and phase 2 are listed in table 1.

Figure 1 shows a schematic of the HR laser system. The laser system is based upon a CEP stable fiber oscillator emitting pulses around 1030 nm with 20 nm bandwidth. The repetition rate of the 80 MHz oscillator is reduced to 100 kHz using two acousto-optic modulators. Two subsequent preamplifier systems, consisting of large pitch fibers (LPFs, 65 μm core diameter, 1 m length), enhance the average power to 20 W. The front end is completed by a double-pass grating stretcher, providing enough dispersion to stretch the pulses to 2 ns.

The output pulse from the front end is divided to eight channels, and each channel is coupled to a separate LPF amplifier pumped by high-power CW diodes, each with a pump power of 80 W. Three diodes can be coupled into one fiber; therefore the maximum applicable pump power would be 240 W. However, safety and long-term stability reasons limit pumping of a single fiber channel to 100 W, which results in amplifying the nanosecond pulses up to 60 W average power per channel without any spectral and spatial distortion. The amplified pulses are then coherently combined with 90% efficiency, resulting in a 100 kHz repetition rate pulse train of 440 W average power. Phase-locking is achieved using piezo actuators and Hänsch–Couillaud detectors to measure the phase difference of each channel relative to a reference channel. A compressor is used after the main amplifier, to shorten the pulses close to the transform limit (~200 fs). The pulses are compressed below two optical cycles in a two-stage non-linear hollow core fiber (HCF) compressors, each filled with a noble gas in order to achieve a high nonlinearity of the propagation medium. The residual dispersion is compensated by chirped mirrors after each HCF stage. To maintain the CEP of the total system, an f-to-2f

Table 2. Current (SYLOS 1) and targeted major parameters for the SYLOS laser system.

Parameters	SYLOS 1	SYLOS 2 (targeted)
Peak Power	4.5 TW	20 TW
Pulse duration	<4 cycles	<2 cycles
Center wavelength	820 nm	900-1000 nm
Repetition rate	1 kHz	1 kHz
CEP stability	250 mrad	<200 mrad
Energy stability	<1.5%	<1.5%
ASE contrast	$>10^{10}$	$>10^{10}$
Strehl ratio	>0.85	>0.85
PPL pulse duration	75 ps	<75 ps

interferometer measures the CEP error at the laser output and this error is fed back to a phase shifter before the pre-amplifier stages.

The HR 1 laser will be further enhanced by increasing the pulse energy to 5 mJ. The expected parameters of the final HR laser system (HR 2) are listed in table 1. Development of the HR 2 laser will start in early 2017, while the installation is scheduled for late 2018.

2.2. Single cycle laser system

The SYLOS laser system will be the ELI-ALPS laser workhorse, combining near-single-cycle pulse duration and multi-TW peak power at 1 kHz repetition rate. Present limitations in laser technology have forced the development of SYLOS to be concurrent with the removal of technical bottlenecks, so that the final target parameters of 20 TW peak power and sub-two-cycle pulse duration can be realized. The current and targeted major parameters of SYLOS are listed in table 2. The initial SYLOS system (SYLOS 1), developed in phase 1, is designed with a double-CPA configuration for high temporal contrast ($C > 10^{10}$), and relies on non-collinear optical parametric chirped pulse amplification (NOPCPA) technology seeded by white light, developed by Light Conversion Ltd., to achieve final amplified spectral bandwidths supporting sub-10 fs compressed pulse duration at 820 nm central wavelength. The different NOPCPA stages are pumped by a state-of-the-art frequency doubled diode pumped Nd:YAG picosecond pump laser (PPL, EKSPLA Ltd.), delivering >350 W of average power in four separate beams at 532 nm.

Figure 2 shows the block design of SYLOS 1. The front end features a modified PHAROS femtosecond chirped pulse amplifier system (fs-CPA, Light Conversion Ltd.), consisting of an Yb-based oscillator (synchronized to the ELI-ALPS master clock) and a regenerative amplifier, producing >1.5 mJ pulses at 1030 nm wavelength. A fraction of the oscillator output is filtered out to provide a 1064 nm seed beam for the PPL chain. Approximately 10% (100-150 μJ) of the regenerative amplifier output is sent into a passive CEP locked pulse generator (fs-OPA-CEP), where it is temporally compressed, frequency doubled and split. The passively CEP stable 1.3–1.5 μm idler pulses from the OPA (optical parametric amplifier) stage are compressed and used to drive white light generation (WLG) and provide broadband seed pulses around 800 nm wavelength for the next stage (fs-NOPA, non-collinear OPA). The 600–1000 nm signal is amplified up to >50 μJ in a series of NOPA stages pumped by the compressed and frequency doubled remainder of the PHAROS output. The amplified signal is then sent into a grism-based stretcher and dazzler (by FASTLITE) to provide >0.5 μJ, 75 ps seed pulses for the NOPCPA power stages. The 750–1000 nm stretched pulses are amplified up to >50 mJ in four consecutive BBO-based NOPA stages (BBO: beta-barium borate) pumped by the different beams of the PPL. Finally, the amplified pulses are compressed using a combination of mixed glass blocks (bulk) in air and chirped mirrors under vacuum to produce <10 fs pulses with >45 mJ energy and stable CEP at 1 kHz.

2.3. High field laser system

The HF laser of ELI-ALPS consists of two laser systems fed by a common front end (figure 3). The HF-PW arm, being built by Amplitude Technologies Inc., will deliver optical pulses at the PW peak power level with an ultra-high temporal contrast ($C > 10^{11}$) as well as the shortest pulse duration and the highest repetition rate achievable by the state-of-the-art laser technology. In numbers this means sub-20 fs pulses with 2 PW peak power at 10 Hz repetition rate. The major parameters of the laser pulses delivered by the HF laser are listed in table 3.

The system will have a second arm (HF-100) with sub-four-cycle pulses, with a reduced peak power of 50 TW but a higher repetition rate of 100 Hz. A common front end seeding of both arms ensures a high level of synchronization between both beams.

The HF-PW arm is based on a Ti:Sapphire and OPCPA hybrid architecture. The front end will provide millijoule level pulses with a bandwidth supporting 10 fs pulses at a high temporal contrast ($C > 10^{12}$). This is achieved in a novel combination of fiber oscillator, non-linear frequency conversion and OPCPA, which has been never used before in PW lasers. A portion of the 2 mJ, 1030 nm pulse from the sub-picosecond fiber based pump laser is used to generate white light. The difference frequency generation stage (DFG) assures high-accuracy passive CEP stability. These pulses are frequency doubled to a central wavelength of 1600 nm. The pulses are recompressed after optical parametric amplification, and once more frequency doubled, providing seed pulses at the central wavelength of 800 nm. These pulses are split to seed the HF-PW and HF-100 arms. An amplification to ~2 mJ pulse energy is then introduced to the high repetition rate arm seed. Finally, cross-phase modulation (XPW) is applied in each arm to reach the required bandwidth, smooth spectral profile, high quality spatial mode and high temporal contrast before the pulse enters the stretchers.

The preamplifiers and the power amplifier stages (figure 3) of the HF-PW laser rely on Ti:sapphire technology. In this case the total gain and thus the gain narrowing are low enough to support pulses with duration below 20 fs. Additional bandwidth correction is accomplished with dielectric coated spectral filters installed between the amplification

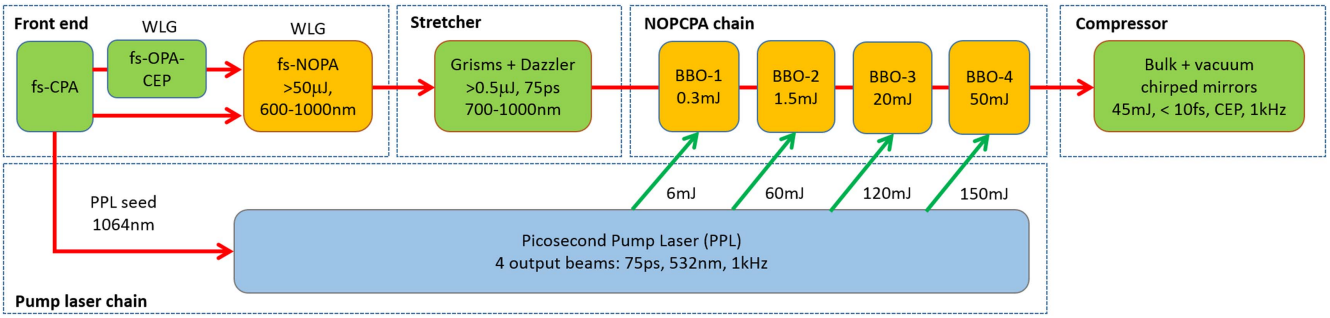

Figure 2. Block diagram for SYLOS 1 laser system.

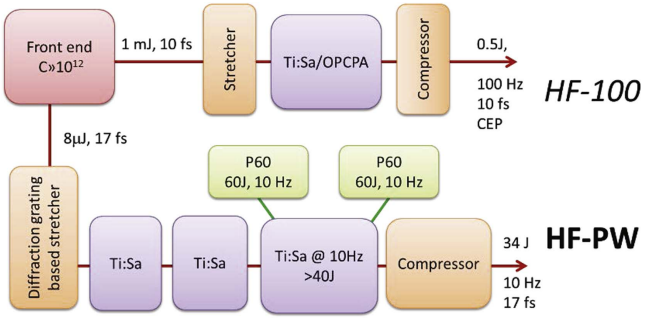

Figure 3. Block scheme of the HF laser system.

Table 3. Major parameters of the HF laser system.

Parameters	HF-PW arm	HF-100 arm (targeted)
Peak Power	2 PW	50 TW
Pulse duration	<17 fs	<10 fs
Center wavelength	800 nm	800–850 nm
Repetition rate	10 Hz	100 Hz
CEP stability	NA	<250 mrad
Energy stability	<1.5%	<1.5%
ASE contrast	$>10^{11}$	$>10^{11}$
Strehl ratio	>0.85	>0.85

stages, similarly to the Apollon laser [19]. The final amplifiers are pumped by two P60 lasers (60 J, 532 nm, 10 Hz) using Twin Amplifier Technology (Amplitude Technologies).

The HF-100 arm is under design at ELI-ALPS. The specified 50 TW at 10 fs pulses require a greater bandwidth than the HF-PW arm, and will most likely use a combination of OPCPA, the newly-developed polarization encoded CPA scheme [20] and thin disk Ti:Sapphire [21, 22] technologies.

2.4. Mid-infrared laser system

The MIR laser will produce radiation in the mid infrared domain (figure 4), where efficient laser materials are not currently available and thus is specified very differently from the other ELI-ALPS laser systems in many respects. For example, an average power of 15 W may appear rather low when compared to the HR and SYLOS (100 W) or HF (300 W) systems. The MIR laser has been designed to operate at a repetition rate compatible with coincidence experiment and the HR laser (see section 2.1). The technology used is suitable for producing few-cycle pulses with intrinsic CEP stability. Typical parameters targeted for the MIR laser are given in table 4. The MIR laser provides femtosecond mid infrared pulses in a OPCPA architecture at a repetition rate of 100 kHz (figure 5). The OPCPA is optically pumped by two intense industrial grade lasers, based on diode pumped Ytterbium-doped laser materials operated at 100 kHz repetition rate. Both pumps are injected by splitting the output of a commercial femtosecond fiber oscillator delivering 200 fs pulses. This seed laser is frequency stabilized and synchronized to the ELI-ALPS master clock, allowing synchronization of the MIR output pulses with other systems (HR or SYLOS) with a timing jitter of only a few fs. The first pump laser consists of a 20 W fiber CPA system delivering 300 fs pulses with a pulse energy of 200 μJ. The second pump laser (Yb:YAG CPA) provides 200 W, 1 ps pulses with a pulse energy up to 2 mJ with excellent beam quality and stability. Both pumps are actively synchronized to ensure a very limited timing jitter between the pump pulses, which enhances CEP stability as well as leading to a better pulse-to-pulse amplitude stability. A small fraction of the 20 W system generates a stable and ultra-broadband supercontinuum, which is further amplified in OPA stages. The amplified signal is then tailored with an acousto-optic pulse shaper. The 3 μm idler beam is generated in a difference frequency generation (DFG) stage. The 200 W pump laser amplifies the 3 μm beam in a series of OPAs. The non-linear crystals used in this setup vary depending on the OPA stage. For example, broad gain bandwidths could be obtained with thin periodically poled crystals, and higher energy amplification may result from wave mixing in potassium titanyl arsenate (KTA) crystals. All delays are controlled by motorized translation stages. Finally, a compression setup compensates for the accumulated dispersion to deliver few-cycle pulses close to the transform limit.

A third beam is also generated at a wavelength ranging from 1400 nm up to 1750 nm due to the three-wave-mixing process involved in the amplification. Unfortunately, this beam is not CEP stable but can still be compressed below 100 fs. This beam has similar energy (150 μJ) to that of the MIR beam and may turn out to provide a precious additional radiation source for pump–probe experiments.

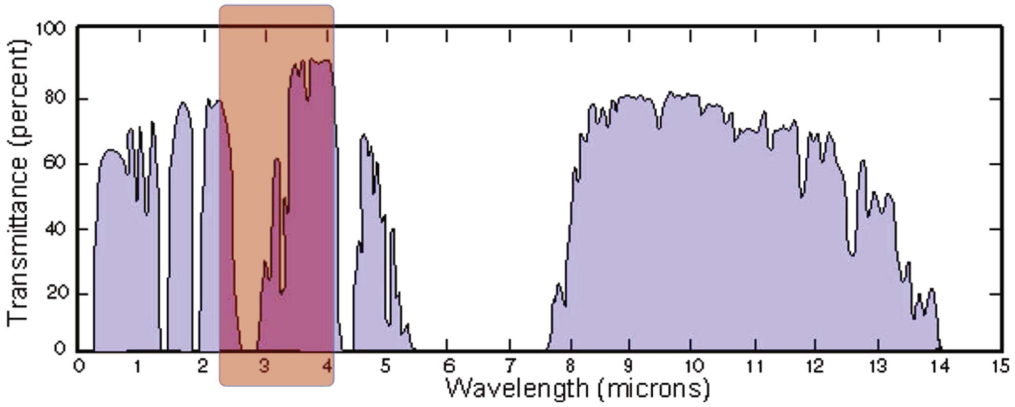

Figure 4. Atmospheric transmittance and the MIR laser emission band.

Table 4. Major parameters of the MIR laser system.

Parameters	MIR Laser
Center wavelength	3.1 μm
Average Power	15 W
Pulse duration	<4 cycles
Pulse energy	<150 μJ
Repetition rate	100 kHz
CEP stability	<100 mrad
Energy stability	<1.0%
Tunability	2.4 μm–3.9 μm
Strehl ratio	>0.5

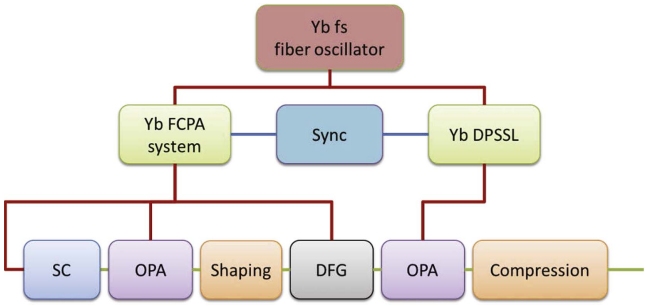

Figure 5. Block diagram of the MIR laser system. (DPSSL: diode pumped solid state laser, FCPA: fiber CPA, SC: supercontinuum, DFG: difference frequency generation).

3. Attosecond sources at the ELI-ALPS facility

3.1. Introduction

The radiation from the lasers introduced in the previous section constitutes a rich experimentation field in its own right, especially for strong-field physics or novel schemes of particle acceleration. However, the primary goal of ELI-ALPS is to provide the scientific community with sources of XUV attosecond pulses that are superior to any currently available sources. In this section, these secondary sources will be introduced with an overview of conceptual and technological innovations, their designated range of operations, and compared and constrasted with other XUV and sub-fs pulse sources. An in-depth discussion of the construction and capabilities of each beamline will also be given in the subsequent sections.

ELI-ALPS will initially host five beamlines for the generation of attosecond light pulses based on two distinct physical processes. Four beamlines will utilize the well established GHHG, and one novel surface high-harmonic generation (SHHG) by coherent wake emission in surface plasmas. GHHG is a process of highly non-linear frequency upconversion, in which the laser field tunnel ionizes a noble gas atom or molecule, accelerates the liberated electron, and finally recollides it at high kinetic energy with the parent ion, thereby emitting bursts of XUV and soft x-ray pulses [3]. Two GHHG beamlines will be driven by the HR laser, and two by the SYLOS laser. The SHHG beamline will be operated by the SYLOS laser.

In the HR beamlines, pulse energies are moderate but the high repetition rate results in a very high average power, and as a result of the large coherent bandwidth of the HR pulse, mirrors with metallic coatings cannot be completely avoided. These mirrors will experience a high thermal load as a consequence of the finite absorption, requiring an efficient cooling scheme. Traditional water-cooled mirror mounts could lead to excessive CEP fluctuations due to mechanical vibrations. Alternative approaches such as special heat conductive substrates are also being currently investigated. Custom tailored, matched dielectric coatings will be applied in other parts of the beamline that are compatible with the large bandwidth and maintain a minimal overall GDD. One beamline will be dedicated to experiments in atoms and molecules in the gas phase, and will be indicated as GHHG HR GAS. The other beamline has been designed for experiments on surfaces and solid state targets, and will be indicated as GHHG HR CONDENSED. This beamline will also include a time-preserving monochromator, making it particularly suitable for condensed matter physics.

The upscaling of the pulse energy in the GHHG beamlines is not straightforward, and generates several physical and technological challenges—especially the fundamental limitations of GHHG by the ionization of the generation medium. The first challenge is to design a GHHG beamline

that can efficiently use high pulse energies from the primary sources—especially SYLOS—and two different approaches will be implemented at ELI-ALPS. One SYLOS-driven beamline (GHHG SYLOS LONG) will employ an extremely loose focusing scheme, and will be coupled with a long interaction cell and very low gas pressures. This combination obeys geometrical scaling predictions and pressure related phase matching considerations governing GHHG in extended media [23–25]. The other SYLOS-driven beamline (GHHG SYLOS COMPACT) will also rely on loose focusing, but will utilize a high-pressure medium where phase matching is ensured by the short interaction length [26]. Both beamlines will apply multiple generation regions to increase the output power by quasi-phase-matching and/or multicolor schemes.

Another more technical issue is how to separate the residual IR light from the generated XUV light without causing damage to the optics, filters and detectors. Again, two different strategies are followed in the SYLOS GHHG LONG and COMPACT beamlines. The former relies on long propagation distances to sufficiently reduce the fluence impinging on the dichroic optics. The latter uses a radially structured generating beam and a complementary spatial filter (pinhole) to remove most of the IR light while admitting the on-axis propagating XUV light to the experimental section.

Thought has also to be given to the phase stability of the interferometers that are present in each beamline to permit cross-correlation and two-color schemes with attosecond resolution. Several innovative strategies to avoid vibrations are already realized in the building architecture. Furthermore, active path length stabilization is implemented in the Mach–Zehnder interferometers of the HR beamlines, whereas an intrinsically stable in-line phase delay interferometer will be integrated into the COMPACT beamline. This approach offers less flexibility in IR beam parameters—but the main emphasis of this beamline is on non-linear XUV interactions and XUV-XUV pump–probe experiments.

As a consequence of the cutting edge nature of the primary lasers of ELI-ALPS, an intense research program will be devoted to the further advancement of the attosecond source performance and also used for exotic pulse parameters requested for special user experiments. Similarly, diagnostics of attosecond pulses must also keep pace with the evolving pulse production, and a dedicated group will pursue corresponding activities on all beamlines. The SHHG beamline will be initially dedicated to the development of this new generation technique, and an extension to SHHG by the relativistically oscillating mirror (ROM) process is also planned.

The remainder of the current section will be used for a brief comparison with other XUV and attosecond sources currently available.

Strong XUV and x-ray pulses have for a long time been almost exclusively associated with third and fourth generation radiation sources—synchrotrons and free electron lasers (FELs)—respectively. In terms of output power and maximum photon energy, HHG will not be a competitor in the near future, but power is not the sole prerequisite for many of the experiments that are the focus of current atomic, molecular and optical (AMO), condensed matter surface and plasma science. The envisioned research topics of ELI-ALPS (section 4 and [27]) and its users will consider parameters including pulse duration, tunability, peak intensity, stability, repetition rate and coherence as well as the synchronization to other sources. Synchronization on the sub-fs time scale can only be achieved if an optical laser is involved already in the pulse generation process. Ultrafast lasers thus play a crucial role in the generation of sub-fs pulses from synchrotrons and FELs, with the immediate consequence that the repetition rate is also ultimately limited to the kHz regime. The attosecond domain remains out of reach, despite seeded FELs (e.g. FERMI@Elettra, European XFEL) overcoming the stochastic temporal pulse structure [28] and high jitter—two major shortcomings of earlier SASE FELs (SASE: self-amplified spontaneous emission)—and delivering Fourier-limited pulses with a well controlled time structure and synchonization [29, 30]. In response to strong interest from the scientific community, serious efforts are under way to break the attosecond barrier. Innovative generation schemes promise future pulse durations of 50–500 as [31, 32] that are already available today with HHG [33, 34]. Comparing the peak power, the appropriate metric for non-linear experiments, shows that current FELs are not that far ahead of state-of-the-art GHHG [35] (table 5). Also, the different generation methods address quite different interactions with matter, as the photon energy of the proposed attosecond FELs lies in the 10 keV range while GHHG is in 10–120 eV range [36].

The waveform synthesizer (WS) has emerged as another potential sub-fs source [37, 38]. One scheme is based on multiplexed solid state laser technology or non-linear propagation to achieve multi-octave coherent bandwidth. Another one uses Raman processes to generate modulations of the medium on the molecular scale, to achieve a similar bandwidth [39]. Although some schemes have shown TW peak powers, the main limitation is a center wavelength restricted to a few eV, precluding it from most AMO experiments. However, the WS has proven to be an invaluable and exciting tool for the investigation of sub-fs dynamics in solids [40, 41].

In summary, there has been a constant growth of sub-fs pulse sources based on quite different technologies, each with a distinction of the working photon energy range. HHG will continue to serve the AMO and condensed matter surface communities, and venture further into the non-linear interaction regime, whilst the field of excellence for FELs will be in non-linear core electron dynamics and single-shot structural imaging. Strong-field, non-linear and sub-fs dynamics in, for example, dielectrics, may become the domain of the high-power waveform synthesizer.

How does ELI-ALPS stand out against existing attosecond pulse sources that are operated in various research laboratories and facilites worldwide? To put it into a simple catchphrase, ELI-ALPS seeks to provide the shortest pulse durations, in the widest spectral range with the highest repetition rates and the highest pulse energies. Realistically, these superlatives will not be achievable all at the same time; this is in fact not even desirable for the experimenter. But the

Table 5. Parameters defining the different XUV photons sources available.

	Rep. rate (Hz)	Pulse duration (fs)	Pulse energy (μJ)	Peak power (GW)	Tuning range (eV)
Synchrotrons	$\geqslant 10^6$	$>10^2$	$\approx 10^{-9}$[a]	$\leqslant 10^{-9}$[a]	10^{-3}–10^5
SASE FEL[b]	1–5000	30–300	1–500	0.03–16	28–295
Seeded FEL[c]	10	$\approx$100	20–100	0.2–1	12–60
GHHG	10^3–10^5	0.07–0.5	$<$0.01	$\leqslant 10^{-3}$	10–120
	10–100	0.07–0.5	0.1–10	10^{-3}–1	10–120
GHHG HR[d]	10^5	$\leqslant$ 0.6–1.3	(0.01–0.1)x10^{-3}	$< 2\ 10^{-4}$	17–90
GHHG SYLOS[d]	10^3	$\leqslant$ 0.5	0.005-0.5	$\leqslant$ 1	10–70
SHHG SYLOS[d]	10^3	$\leqslant$ 1	$\leqslant$ 3	$\leqslant$ 3	8–60

[a] Estimated from peak brilliance relative to FELs.
[b] Values for FLASH.
[c] Values for FERMI at ELETTRA.
[d] Conservative values, improved operating values expected.

facility will thus be able to address a diversity of user experiments at the extremes of state-of-the-art technology like no other installation at this time. For instance, 100 kHz attosecond pulses will significantly improve the data quality and information content of coincidence based measurement schemes or surface solid state experiments. The possibility to combine pulses originating from a single driving source, ranging from the THz all through to the soft x-ray spectrum, coherently and with sub-femtosecond accuracy is a novelty that permits highly selective targetting of specific excitations and their dynamics in the systems under study. High pulse intensities from the 1 kHz attosecond beamlines are a starting point for eagerly awaited studies of non-linear interactions in the XUV spectral range that to date cannot be performed at any other installation with adequate statistics. It is the combination of repetition rate, pulse energy and operational stability (i.e. reliability) which will yield benchmark experimental data on multi-photon, multi-electron photoionization dynamics and correlations, as well as on electronic, vibronic and photofragmentation dynamics in atoms and molecules. The determined effort to develop SHHG will further broaden the range of such experiments through the even higher pulse energies that could be achieved in the future, including photon-hungry applications like structural and 4D imaging while at the same time providing experimental insights into the fundamentals of plasma dynamics on the attosecond time scale. High photon energies compatible with atomic and molecular core excitations will give insight into related dynamics of inner shell electron excitation and the further extension of the energy range to the water window by the use of the MIR driver will provide access to charge dynamics in biologically relevant systems, once again with the unique flexibility of the available multicolor sub-fs high-repetition sources. Granted, a specialized laser system with streamlined features for a particular experimental investigation could also be built at any other laboratory; but ELI-ALPS will be the place where these studies can be taken one step further, providing at least one order of magnitude better parameters than what can be routinely achieved with common state-of-the-art technology. In the near future ELI-ALPS will also commission two PW class lasers with associated particle beamlines and thus become a focus point for the study of relativistic and plasma dynamics through the unique combination of sub-fs resolution capabilities and ultra-high light field intensities. A few planned experiments and major research areas are briefly mentioned in section 4. For an in-depth account of the envisioned research directions the reader is referred to the 'Scientific Case' of ELI-ALPS [27].

3.2. GHHG HR GAS and GHHG HR CONDENSED

The target of the GHHG HR GAS (GAS in the following) and GHHG HR CONDENSED (CONDENSED in the following) beamlines is the generation and application of attosecond pulses at a repetition rate of 100 kHz using HHG in noble gases. These secondary sources will be driven by the HR laser, and will provide users with attosecond and auxiliary pulses to perform ultrafast XUV-pump-IR-probe experiments. The beamlines will feature a double interaction region geometry with the first interaction region dedicated to the temporal characterization of the XUV radiation and followed by the refocussing of the XUV and IR pulses in a second interaction region, where different user-defined interchangable end stations will be placed. It will be possible to perform at least two experiments at the same time.

The two beamlines are designed to probe different samples or targets: the GAS beamline is intended for experiments in transparent targets such as gaseous species, while the CONDENSED beamline will probe non-transparent samples such as solid targets. Figure 6 shows that both beamlines have a similar layout, consisting of five main sections:

Section 1: IR splitting, IR gating and XUV generation
Section 2: first XUV-IR recombination chamber and focusing section for the first target area
Section 3: time-of-flight (TOF) electron spectrometer placed in the first target area to measure the XUV pulse duration
Section 4: second XUV-IR recombination chamber and focusing section for the second target area
Second target area: user end station
Section 5: intensity monitor and XUV photon spectrometer.

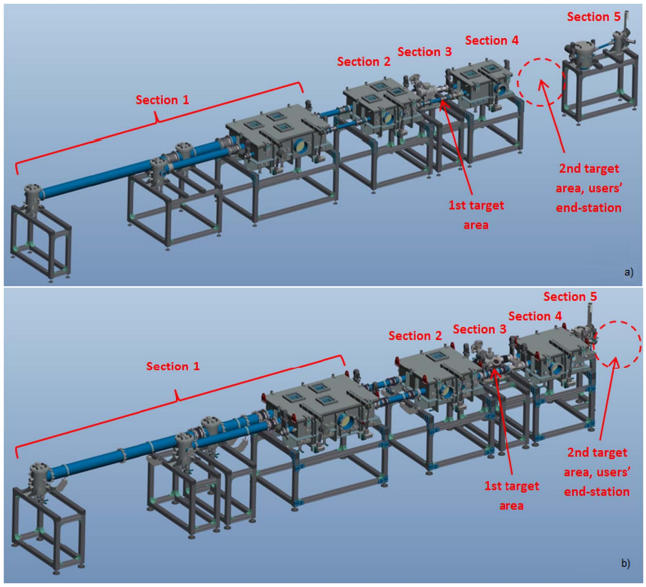

Figure 6. Layout of the two GHHG HR beamlines: (a) GAS, the diagnostic section is in-line; (b) CONDENSED, the diagnostic section is in-line (the spectral diagnostics if off-line).

All sections (1–4) before the user end station are placed on the same optical table (not shown), in order to improve the mechanical stability of the beamline. The optical elements for handling the XUV attosecond beam and the IR femtosecond beams are mounted on breadboards rigidly anchored to that optical table. The vacuum chambers are mounted on external frames, and are mechanically isolated from the optical table to improve the isolation of the attosecond section from the external vibrations.

Test samples in the GAS beamline are totally or partially transparent to XUV radiation, and thus a diagnostic section is inserted after the second target area for simultaneous in-line monitoring of the spectral features and intensity stability of the XUV radiation.

However, the majority of CONDENSED beamline test samples are intended to be solid. Therefore, the diagnostic section cannot be inserted after the second target area but has to be inserted on a separate optical path with non-concurrent spectral and intensity monitoring.

3.2.1. General optical layout. The optical design of the beamlines is particularly challenging, especially because of the extremely high IR average thermal load. The generating laser has an average power of 100 W in phase 1, i.e. 1 mJ/pulse at 100 kHz, and 500 W in phase 2, i.e. 5 mJ/pulse at 100 kHz. Experiments with attosecond pulses require special attention for the mechanical stability in the optical paths.

The portion of the IR beam that generates the XUV attosecond radiation co-propagates with the XUV pulses, and has to be stopped so as to avoid damaging of the XUV optics by the high thermal load. The use of plates at Brewster angle to stop the p-polarized component of the IR beam [42] is not applicable in the case of generation of isolated attosecond pulses with the polarization gating technique [43], as the IR beam is elliptically polarized. The use of any cooling recirculating liquid in vacuum should be avoided, because vibrations may be transmitted directly to the optical elements handling attosecond pulses. These considerations lead to the adoption of annular geometry to generate XUV pulses [44]. Owing to the difference in divergence between the co-propagating IR beam and the generated XUV beam, efficient IR rejection can be accomplished by a suitable annular beam stop. The optical layout of the beamlines in phase 1 is shown in figures 7 and 8. The optical layout of section 1 in phase 2 is shown in figure 9.

The IR beam entering into the first vacuum chamber is immediately split by a holey mirror into beam 1 and beam 2. Beam 1 is the external component, has an annular section, and is used to generate attosecond pulses in the annular geometry. Beam 2 is the central part, and propagates toward the recombination chamber.

Beam 1 is sent to the optical stage for the polarization gating, then to the focusing spherical mirror. A short-focal mirror will be used for phase 1, while in phase 2, a long-focal mirror will be used. After attosecond pulse generation, beam 1 propagates collinearly with the XUV towards CH-02, and is stopped by a suitable beam dump. The XUV beam passes through a metallic filter, located after the beam dump, and is finally focused by a grazing incidence ellipsoidal mirror in the first target area where the TOF electron spectrometer is located.

The XUV-IR relative delay of beam 2 is created by an optical delay stage; then the beam propagates to the recombination chamber. Beam 2, the central part of the IR beam, has dimensions comparable to the XUV beam and has to be increased in size, through a telescope arrangement realized with two concave mirrors in CH-02, before the XUV-IR recombination. The enlarged beam is focused by a spherical mirror and recombined with the XUV by a holey mirror. After the TOF chamber, the XUV and IR beams propagate to the second recombination chamber. Two optical configurations of the XUV-IR recombination may be realized in order to provide the final XUV and IR beams to the users:

Configuration 1: the XUV and IR beams recombine in CH-02 and then, after the TOF chamber, propagate collinearly to a grazing incidence toroidal mirror hosted in CH-04, which focuses both beams in the second target area.

Configuration 2: the XUV and IR beams can be recombined in either chamber CH-02, in case of measurements with the TOF, or chamber CH-04, for measurements in the second target area. A moveable plane mirror in CH-02 is inserted in the optical path to choose between the two options.

The choice of the configuration has to be taken during the commissioning phase of the beamline and depends on the actual performance, as both configurations have advantages and drawbacks. The first configuration is easier to align and

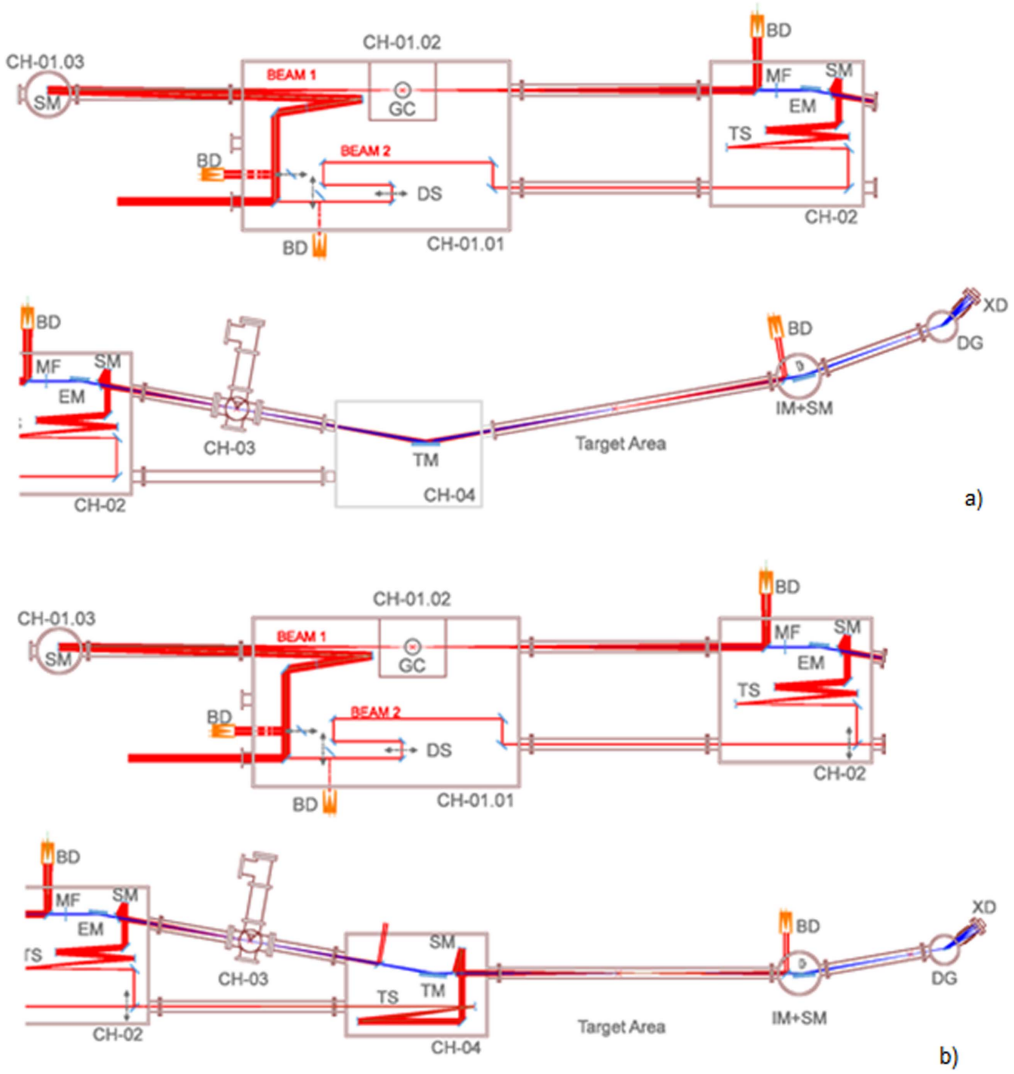

Figure 7. Optical layout of the phase 1 GAS beamline with IR (red) and XUV (blue) paths. The vacuum chambers are divided in sections and numbered consecutively, e.g. CH-01.03 is the third chamber of section 1. Two possible configurations are presented: (a) IR and XUV are recombined once just before the first target area and then propagate collinearly up to the users target area; (b) IR and XUV are recombined either in the first recombination chamber for the measurements in the first target area using the time-of-flight spectrometer or in the second recombination chamber for the measurements in the users target area. Legend: BD, beam dump; DS, delay stage; SM, spherical mirror; PM, plane mirror; GC, gas cell; MF, metallic filter; EM, ellipsoidal mirror; TS, telescope section; TM, toroidal mirror; IM+SM, intensity monitor + spectrometer mirror; DG, diffraction grating; XD, XUV detector.

the two target areas can be operated simultaneously. In the second configuration, there is a higher XUV photon flux as the last focusing mirror can be operated at a lower grazing angle.

The last section consists of an XUV intensity monitor and a photon spectrometer. The XUV absolute intensity is measured by a calibrated metallic photodiode that is completely blind to IR. The XUV photon spectrometer adopts an established design with high flexibility [45–47], that allows the measurement of either spectrum and divergence simultaneously, or the spectrum only with better signal-to-noise ratio. In the GAS beamline, the diagnostic section is inserted in the main optical path after the second target area, which is intended for experiments in transparent targets such as gaseous species. In the CONDENSED beamline, the diagnostic section is on a different optical path, and is operated alternatively to the users experiments, by inserting a suitable deflecting mirror.

3.2.2. Detailed layout. The optical layout of the two beamlines are now discussed in greater detail; a fundamental beam with a central wavelength of 1030 nm and a FWHM diameter of 12 mm is assumed. Figures 7 and 8 show that the IR beam is initially split by a holey mirror at 45° into the annular external part, used to generate attosecond pulses (beam 1), and the central part that is later recombined with the XUV (beam 2). The diameter of the central hole that gives a 70:30 ratio is 8.5 mm, although mirrors with holes of various diameters will be tested to optimize the IR/XUV ratio for pump–probe experiments. A central hole with 8 mm diameter is assumed. Immediately after the splitting mirror, two systems can independently stop the two IR beams. The

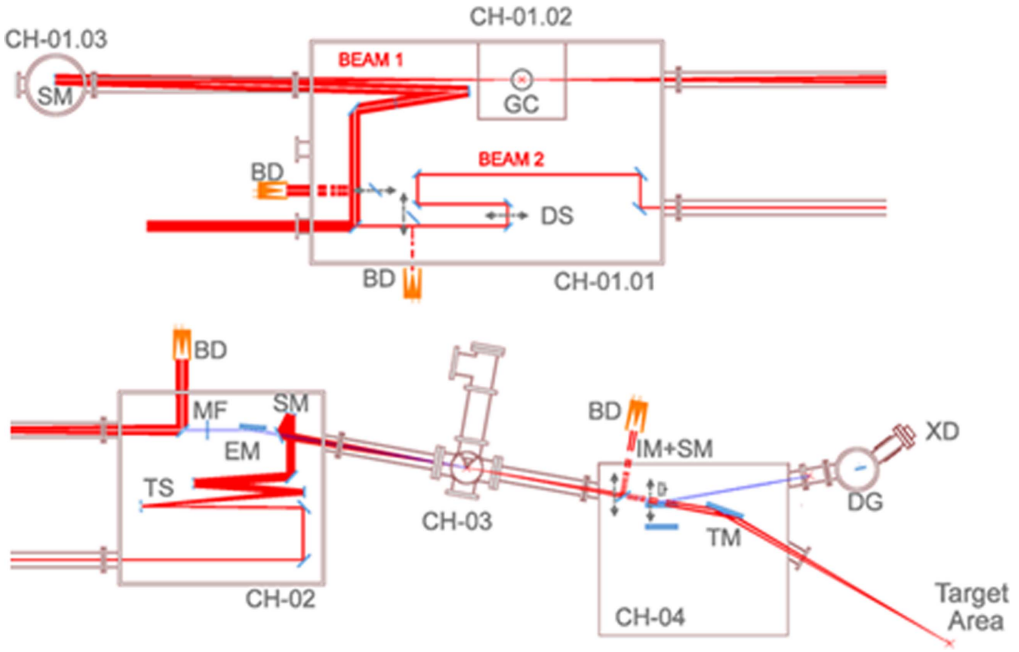

Figure 8. Optical layout of the CONDENSED beamline with IR (red) and XUV (blue) paths, phase 1. Only configuration 1 is presented: IR and XUV are recombined once just before the first target area.

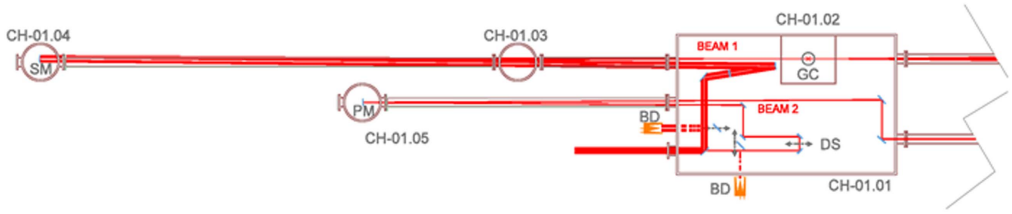

Figure 9. Optical layout of the section 1 of the two beamlines in phase 2. Two accessory chambers are added to the layout to host: respectively, a long-focal spherical mirror to generate XUV attosecond pulses, and a folding mirror to realize a longer path for beam 2. The subsequent sections of the beamlines are unchanged.

beam stop is a mirror at 45° with a broadband coating centered at 1030 nm, deflecting the laser beam 90° toward a high average power beam dump mounted externally to the vacuum chamber through a window with anti-reflection coating centered at 1030 nm. The beam dump is water-cooled, and thus mechanically separated from the optical tables to isolate from potential vibrations.

Beam 1 initially propagates through two wedges, used to compensate for dispersion and to change the relative phase between beam 1 and beam 2, and then passes through two ultra-broadband birefringent plates, used to realize the polarization gating for the generation of isolated attosecond pulses. The beam is finally focused by a spherical mirror at almost normal incidence, located in either the auxiliary chamber CH-01.03 for phase 1 or in CH-01.04 for phase 2. Assuming a laser peak intensity in the gas cell of the order of 10^{15} W cm^{-2} results in estimated focal lengths of 2.2 m (phase 1) and 5.7 m (phase 2). The actual focal length to be used for the XUV generation will be determined during beamline commissioning.

Attosecond pulses are generated in a gas cell containing noble gases, with a length ranging from 2 to 10 mm. These cells are located in a small generation chamber inside the main chamber in order to have a restricted volume that is independently pumped with a high gas load and at relatively high pressure, (figure 10). The only apertures between the two chambers are the two holes that let the IR and XUV beams propagate and act as differential stages. After the generation, XUV and annular IR propagate collinearly, with a different divergence and beam shape.

Beam 2 propagates through two wedges that compensate for dispersion and change the relative phase. The beam is delayed by a motorized optical delay stage and finally propagates toward the recombination chamber. If the optical path of the beam 2 has to be increased to match the XUV and IR path lengths, it can be sent to a folding plane mirror placed in the auxiliary chamber CH-01.05. The use of this chamber is required only for phase 2, where the expected focal length of the spherical mirror is in the 5.5–6 m range.

Upon entering section 2, the annular IR beam, that generates XUV pulses is blocked by a suitable beam stop—a deflecting holey mirror placed in vacuum, a window and an external beam dump placed in air. This mirror has a central hole to allow the XUV to further propagate; this hole's diameter is the same as that of the hole of the beam splitting

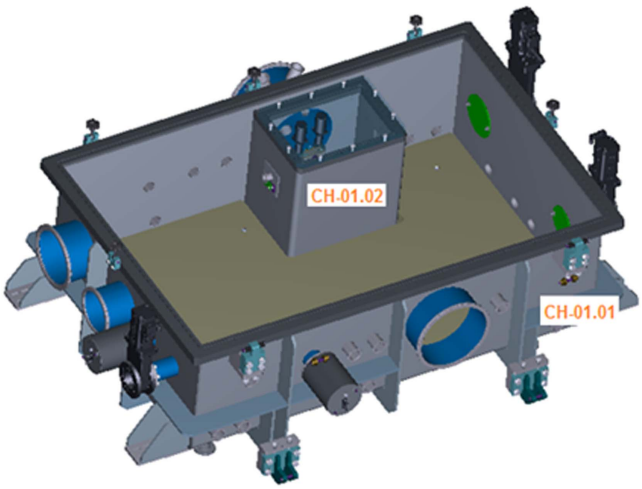

Figure 10. 3D layout of the main chamber of section 1. CH-01.01 hosts the optical elements and motorized movements to split and handle the two IR beams. The gas cell for the generation of attosecond pulses is hosted in CH-01.02, and is independently pumped to increase the differential pumping capabilities. The IR focusing mirror is mounted on an external chamber.

mirror projected by the spherical focusing mirror. For phase 1, the hole is assumed to be 6 mm and small enough to stop the annular IR portion and possible IR diffracted light. An XUV full divergence of 2.7 mrad is acceptable in this case. The XUV is then filtered by a metallic thin foil (typically aluminum) to block any residual IR light, and to introduce the required group delay-dispersion to correct for the XUV pulse chirp.

The XUV beam is then focused by an ellipsoidal mirror at grazing incidence (5°) giving 2.5 demagnification at the output, i.e. 2.5 m entrance arm and 1 m exit arm. As the entrance and exit arms are different, a toroidal mirror would give unacceptable distortions of the wavefront due to coma and higher-order aberrations leading to temporal pulse broadening as high as 0.8 fs FWHM according to simulations. Therefore, an ellipsoidal mirror, which theoretically gives no distortion, is employed.

Beam 2, entering in CH-02, has a cross-section comparable to the XUV, and therefore has to be magnified before recombination through the holey mirror. This is realized by a suitable telescope realized with two mirrors in CH-02. Finally, the beam is focused by a spherical mirror and recombined with the XUV by a holey mirror at 45° that reflects only an annular portion of the IR and lets the XUV propagate through its central hole. The position and the focus of the spherical mirror have to be chosen in order to ensure that the IR and XUV focus overlaps with the necessary intensity to permit electron streaking.

Simulations of the focusing conditions for the IR beam show that, assuming an IR focal length of 1.5 m, a magnification of the IR beam by a factor 1.5 (e.g. obtained by a defocusing mirror, $f = -1$ m and focusing mirror, $f = 1.5$ m, separated by 0.5 m) and recombination using a mirror with a central hole of 6 mm, an intensity at the IR focus of more than 10^{13} W cm^{-2} is achievable—which is sufficient for streaking effects. The actual magnification factor of beam 2 before recombination will be determined during commissioning.

The temporal duration of the attosecond pulses will be measured in the first target area by a TOF electron spectrometer [48] applying the FROG-CRAB (frequency resolved optical gating for complete reconstruction of attosecond burst) technique as discussed in detail in [33].

In configuration 1, both XUV and IR beams are propagating collinearly to CH-04 to a moderate grazing incidence (10°) toroidal mirror in 1:1 configuration, i.e. 1.2 m entrance and exit arms, that focus both beams in the second target area. In the 1:1 configuration, the toroidal mirror gives negligible aberrations, as all the terms up to the third order are corrected—in particular, defocusing, coma and astigmatism [49]. In the geometry here discussed, the distortion of the wavefront due to the residual aberrations has been simulated to be ideally 0.015 fs FWHM for the central XUV beam having 1.5 mrad divergence, being therefore totally negligible. For the IR beam, the wavefront distortions have been calculated with different magnifications in CH-02, resulting in 0.08 fs for $M = 1.5$ (12-mm IR cross-section), 0.17 fs for $M = 2$ (16-mm IR cross-section) and 1.0 fs for $M = 3$ (24-mm IR cross-section), again almost negligible when compared to the duration of the IR pulse.

The toroidal mirror is assumed to have a 40 nm gold coating, a standard value for XUV coatings. The average XUV reflectivity is 0.7 in s-polarization and 0.5 in p-polarization. In the 700–1300 nm band, the average mirror reflectivity, absorbance and transmission are respectively 0.99, 0.005 and 0.005 for s-polarized light; 0.84, 0.08, 0.08 for p-polarized light. The mirror mounting will be provided with a cooling option and a beam dumping system immediately behind it.

In case of configuration 2, the IR-XUV recombination occurs either in CH-02 or in CH-04. The XUV beam is focused by a toroidal mirror at grazing incidence (5°) in 1:1 configuration, i.e. 1.2 m entrance and exit arms. The mirror is used at a lower grazing angle than configuration 1, i.e. 5° versus 10°, to increase the XUV reflectivity. In the geometry here discussed, the distortion of the wavefront due to the residual aberrations has been simulated as 0.03 fs FWHM, therefore is negligible. The average XUV reflectivity is 0.85 in s-polarization and 0.70 in p-polarization.

Finally, both XUV and IR are focused in the second target area, where the user end station can be placed.

Section 5 is dedicated to spectral and intensity diagnostics of the XUV attosecond beam. The XUV absolute intensity is measured by a metallic calibrated photodiode, that is completely blind to any contribution possibly coming from the IR diffused light. The XUV spectrum is measured through a spectrometer equipped with a pre-focusing concave mirror, a flat field variable-line-spaced grating and a microchannel-plate detector with phosphor screen and CCD camera. Two different pre-focusing mirrors can be inserted. The first is a toroidal mirror with its tangential focus on the virtual entrance slit in front of the grating and its sagittal focus on the detector, to obtain a stigmatic spectrum and therefore

Table 6. Main characteristics of the attosecond pulses from the GAS and CONDENSED beamlines.

	Phase 1		Phase 2	
	Trains of attosecond pulses	Isolated attosecond pulses	Trains of attosecond pulses	Isolated attosecond pulses
Spectral range (eV)	17–30 eV (generating gas: xenon or krypton, aluminum filter)			
Output energy at the end station interaction point (pJ)	15–50	5–15	85–250	25–90
Spectral range (eV)	25–55 eV (generating gas: argon, aluminum filter)			
Output energy at the end station interaction point (pJ)	5–25	3–8	35–125	10–35
Spectral range (eV)	70–90 eV (generating gas: neon, zirconium filter)			
Output energy at the end station interaction point (pJ)	3–10	1–3	15–45	4–15

the best signal-to-noise ratio, even when measuring faint signals. The alternative is a cylindrical mirror having its tangential focus on the virtual entrance slit in front of the grating, to obtain an astigmatic spectrum that may be useful to measure the divergence of the XUV beam as altered by the XUV-target interaction [50].

3.2.3. Auxiliary system for interferometric stabilization. The relative paths between the IR and the XUV beams have to be stabilized by interferometric measurements, in order to be able to perform measurements with attosecond time resolution and long-term stability. The aim of the auxiliary system is to compensate for any residual mechanical instability that could affect the temporal resolution in the experiments. The fine variations of the relative path between the IR and XUV arms are compensated by a piezo-driven delay stage mounted in the IR delay line. The system is realized with a frequency stabilized He-Ne laser, which travels a few centimeters above the main laser beams. The He-Ne beam is split in two by a beam splitter rigidly mounted above the holey IR split mirror and then propagates in two directions following the same path as the IR and XUV beams, being reflected by mirrors that are rigidly mounted above the same supports holding the main optics. The beams are finally recombined and extracted just before the XUV-IR recombination and the interference fringes are measured on a 2D camera. A suitable software program calculates and maintains the constant phase of the fringes by applying a proper correction to the piezo-driven delay stage of the IR beam delay line. The speed for the feedback loop is in the range 2–10 Hz.

3.2.4. Attosecond pulse specifications. The main characteristics of the attosecond pulses from the two beamlines are summarized in table 6.

3.2.5. Beamline parameters. The beamline parameters are finally summarized in table 7.

3.2.6. Future developments: monochromator. The aim of this section is to show how the CONDENSED beamline could be possibly modified in order to add a monochromator for the selection of a single harmonic or a sub-band. The design discussed here is preliminary, and can be tailored to users' specific requirements. The main requirements are listed here:

- The monochromator has to be tunable over the whole spectral range of the beamline.
- The monochromator section has to be inserted without any modifications to the main chambers. Additional chambers and optical tables can be inserted, keeping the total length of the beamline within the available space in the laboratory.
- The beamline has to maintain both operating conditions: attosecond pulses, as in the broadband design, or monochromatic pulses in the few-to-several femtosecond time scale using HHG.
- The loss of flux in the broadband beamline due to the insertion of the monochromator section has to be almost negligible with respect to the original configuration.

A grating-based monochromator is proposed here, given the extended range of tunability (17–90 eV). Grating monochromators for ultrafast pulses are divided in two main categories. The first group are conventional monochromators with a single diffracting stage for monochromatization resulting in a pulse-front tilt [51]. The second class are time-delay compensated monochromators with two diffracting stages. The first stage provides monochromatization and the second stage compensates for the pulse-front tilt [52]. The double-stage monochromator is more complex than the single-stage but gives extremely high temporal resolution: time responses shorter than 10 fs have already been measured in existing beamlines [53].

Given the available space in the laboratory and the actual length of the CONDENSED beamline, a double-stage monochromator with temporal response in the femtosecond time scale (typically shorter than 20 fs) and high spectral resolution (bandwidth in the range from several tens to few hundreds of eV) is proposed; in the following, it will be referred to as section 6.

The monochromator uses plane reflection gratings illuminated at grazing incidence and mounted in off-plane geometry [54]. It has been shown that the efficiency of such a mounting is much higher than the classical configuration—the

Table 7. The beamline parameters.

SECTION 1	Phase 1	Phase 2
IR splitting	≈70% (annular), ≈30% (central)	
XUV generation (beam 1)	IR annular beam	
IR energy (70:30 splitting ratio)	<0.7 mJ/pulse	<3.5 mJ/pulse
IR focusing	2.0–2.5 m	5.5–6 m
IR beam size	12-mm FWHM diameter, 8 mm central hole	
IR secondary beam (beam 2)		
Energy (70:30 splitting ratio)	<0.3 mJ/pulse	<1.5 mJ/pulse
Beam size	8 mm full diameter	
SECTION 2		
XUV focusing	Ellipsoidal mirror	
Grazing angle	5°	
Entrance arm	2.5 m	
Exit arm	1 m	
XUV coating	Gold, 40 nm	
XUV reflectivity (13–73 nm)	0.85 (s-polarization) 0.70 (p-polarization)	
XUV spot size in the 1st target area	⩽100 μm	
XUV pulse-front-tilt	<0.03 fs	
IR focusing	Telescope, spherical mirror, holey mirror	
Telescope magnification	1.5 (12 mm IR section) ÷3 (24 mm IR section)	
IR coating	Enhanced silver (negligible GDD) or dielectric (if low-GDD available)	
Focal length	⩾1 m	
IR spot size in the 1st target area	⩽200 μm	
SECTION 3	Time-of-flight electron spectrometer	
Minimum electron energy	≈20 eV	
Time-of-flight resolution	$T/\Delta T \approx 100$	
Field-free drift tube	350 mm standard length, μ-metal shielded	
Microchannel-plate detector	Two-stage chevron geometry, 40 mm active diameter	
SECTION 4 CONFIGURATION 1		
XUV and IR focusing	Toroidal mirror	
Grazing angle	10°	
Entrance/exit arm	1.2 m	
Coating	Gold, 40 nm	
XUV reflectivity (13–73 nm)	0.70 (s-polarization) 0.50 (p-polarization)	
XUV spot size in the 2nd target area	⩽100 μm	
XUV pulse-front-tilt	<0.03 fs	
IR reflectivity (700–1300 nm)	0.99 (s-polarization) 0.84 (p-polarization)	
IR spot size in the 2nd target area	⩽200 μm	
IR pulse-front-tilt	<1 fs	
SECTION 4 CONFIGURATION 2		
XUV focusing	Toroidal mirror	
Grazing angle	5°	
Entrance/exit arm	1.2 m	
Coating	Gold, 40 nm	
XUV reflectivity (13–73 nm)	0.85 (s-polarization) 0.70 (p-polarization)	
XUV spot size in the 2nd target area	⩽100 μm	
XUV pulse-front-tilt	<0.03 fs	
IR focusing	Telescope, spherical mirror, holey mirror	
Telescope magnification	1.5 (12 mm IR section) ÷3 (24 mm IR section)	
IR coating	Enhanced silver or dielectric (if low-GDD available)	
Focal length	⩾1.2 m	
IR spot size in the 2nd target area	⩽200 μm	
SECTION 5	XUV diagnostics	
Intensity diagnostic	Absolutely calibrated metallic photodiode	
Spectral diagnostics	Flat field spectrometer	
Spectral range	13–73 nm	
Resolving element	≈0.03 nm/pixel at 40 nm (30 μm pixel size on the phosphor screen)	

diffraction efficiency of a single grating can be as high as 0.70 [55]. The design requires two toroidal mirrors and one plane grating for each of the two stages. The first mirror collimates the light coming from the entrance source point, the grating is operated in parallel light, then the second mirror focuses the diffracted light on the output focal plane. A slit is placed in the intermediate focal plane between the two sections to perform the spectral selection. The wavelength scanning is provided by rotating the two gratings around an axis passing through the grating center and parallel to the groove direction.

The geometry of the modified CONDENSED beamline as shown in figure 11 with the additional vacuum chamber, CH-06, and the slit block, CH-07. The total length of the beamline is increased by ≈3 m but is still within the bounds of the laboratory.

Figure 11(a) shows the monochromatic case. The IR generating annular beam is blocked by a suitable beam dump when entering in CH-06. The XUV radiation is monochromatized by the first stage on the output slit, then enters the second stage of the monochromator, to compensate for the pulse-front tilt and focus the XUV monochromatic light on the TOF electron spectrometer. The input and output arms of the first stage have to be 2 m long to have enough space to accommodate the beam dump after the generation chamber.

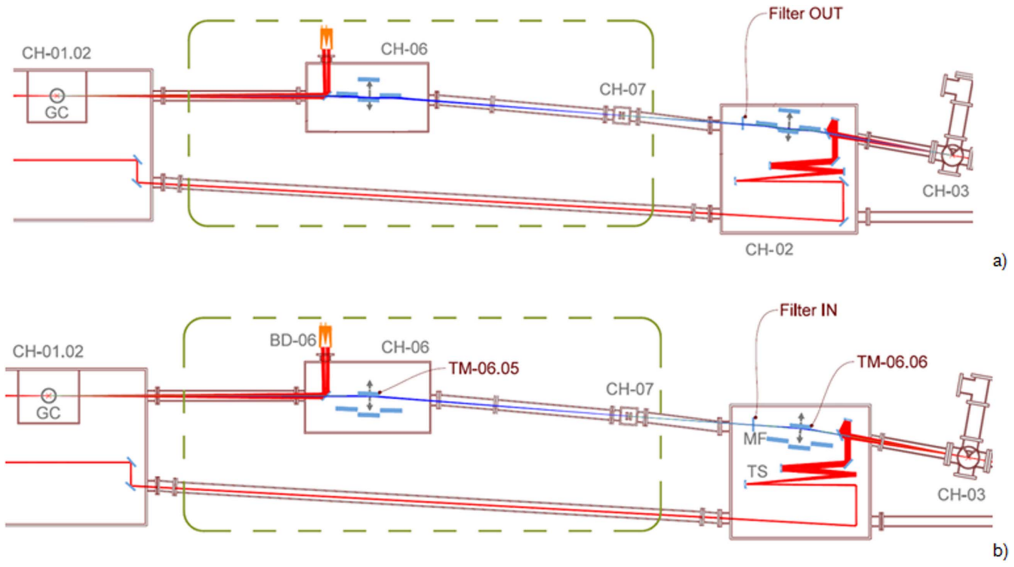

Figure 11. Geometry of the modified CONDENSED beamline to accommodate the double-stage grating monochromator: (a) monochromatic case; (b) broadband case. The section to be added (first stage of the monochromator and slit) is that within the dashed rectangle.

The second stage is more compact, with 1 m arms, to have the same focal length toward the TOF as in the original design. Therefore, to compensate the pulse-front tilt, the groove density of the gratings in the second stage has to be twice that of the first stage. Depending on the performance requirements, the monochromator may accommodate several gratings optimized in different spectral regions, with different energy resolution, temporal resolution, energy of peak efficiency.

The monochromator is assumed to be used with harmonic pulses generated from laser pulses centered at 1030 nm. The harmonics are separated by 2.4 eV; therefore, a resolution of 1 eV FWHM is sufficient to separate adjacent harmonics. Figure 12(a) shows an example of possible performance of energy resolution in the 100 meV–1 eV range. Note that the compensation of the pulse-front tilt is typically in the 1–5 fs range and below 10 fs.

It is worth mentioning that, depending on the requirements from the users, the monochromator may be used either as a double-stage instrument with ultrafast response in the femtosecond range, (figure 12(c)) or as a single-stage with longer temporal response in the 50–200 fs range, (figure 12(b)). In the latter scenario, only the first section monochromatizes the light, that is later focused on the TOF spectrometer by the same toroidal mirror used to focus the attosecond pulses. Having a single diffracting section inserted in the optical path, the photon flux is increased at the expense of a longer temporal response.

The broadband case is shown in figure 11(b). The two stages of the monochromator are removed from the optical path, the slit is completely open and the XUV light is focused on the TOF by two toroidal mirrors used in 1:1 configuration respectively at 2° and 3° grazing angles. With respect to the original design, an additional focusing mirror has been added to the configuration, i.e. two toroidal mirrors instead of a single ellipsoidal mirror. The loss of flux due to the additional reflection is almost totally compensated by the increase of

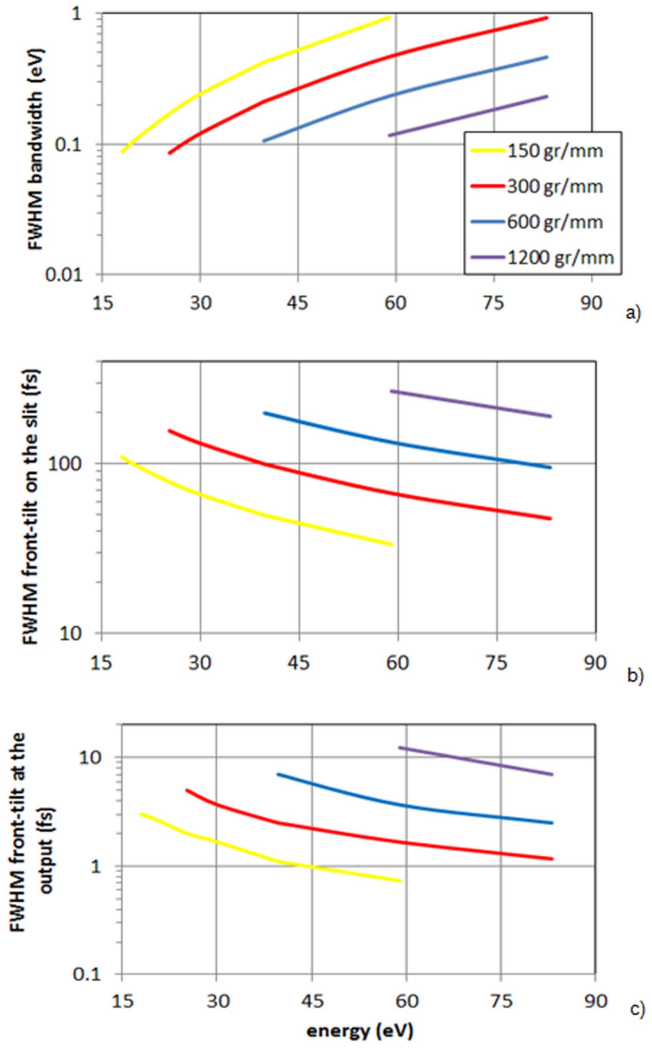

Figure 12. Monochromator performance with four different gratings: (a) bandwidth on 100 μm slit; (b) front-tilt on the slit; (c) front-tilt at the output.

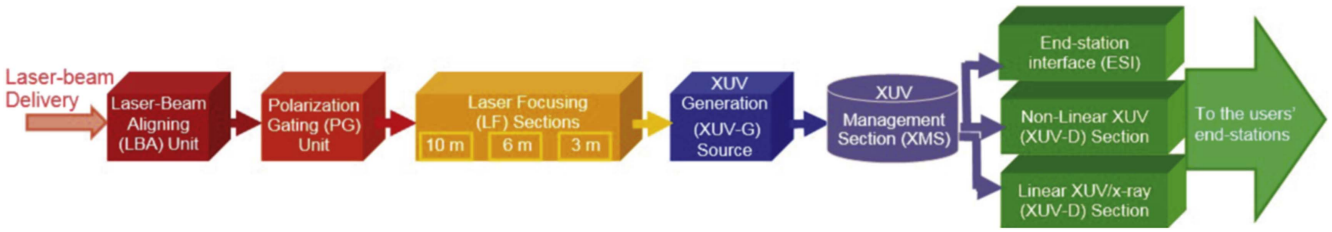

Figure 13. Block diagram of the SYLOS-driven users HHG beamline. The beamline consists of LBA, collinear waveplate PG, LF supporting three different focal lengths, XUV-G based on a gaseous non-linear medium, XUV-BS, steering and spectral-range-selecting section (XMS), XUV-D with subsections for XUV-CC and XUV-AC measurements, as well as a number of other diagnostics, and the end station interfacing (ESI) branch.

reflectivity with the grazing angle. Therefore, the expected throughput for the broadband option is unchanged with respect to the original configuration.

3.3. GHHG SYLOS COMPACT

3.3.1. General considerations. In this section, the compact attosecond beamline operating a HHG-based source in gas media [56, 57] driven by the SYLOS laser chain of the ELI-ALPS facility is described. Besides the HHG source, the beamline includes laser beam manipulation setups, XUV radiation diagnostics and instrumentation relevant to the experimental exploitation of the attosecond pulses by the users.

The beamline targets optimized vacuum ultraviolet (VUV)/XUV photon fluxes, pulse durations, multiple operational spectral regions ranging from the VUV to XUV, reliable diagnostics, versatility, and long-term operational stability. The instrumentation, relevant to the realization of experiments, is aimed to serve general user purposes. Dedicated user end stations will satisfy the specialized needs of users; these will be provided by ELI-ALPS (section 4) or by end stations brought to the facility by the users. One of the exit ports of the beamline is explicitly designed to accept these custom user end stations.

A block diagram of the beamline is shown in figure 13 and the optical layout is presented in figure 14. The beamline consists of: SYLOS beam delivery system, 1st polarization gating chamber (PG1), compressor (CM), laser beam aligning (LBA) unit, 2nd polarization gating (PG2) chamber, IR steering unit (IR-st), laser focusing (LF1-3) sections, differential pumping (DP), XUV generation gas target (XUV-G) chamber, XUV beam separation/splitting/steering (XUV-BS), XUV beam manipulation (XUV-BM) chambers, XUV diagnostics (XUV-D) unit based on non-linear XUV autocorrelation (XUV-AC) temporal beam characterization, XUV diagnostics unit based on IR-XUV cross-correlation (XUV-CC) temporal beam characterization, interface to user end station (End St.) for gas phase experiments, and interface to user end station for condensed matter experiments.

It is well established that optimization of GHHG conversion efficiency, i.e. the source output, depends on a balance between maximum possible driving intensity, saturation effects, target gas properties and propagation effects (phase matching). Given the high pulse energy of the SYLOS laser chain at full driving laser energy, operation just below target ionization saturation intensity, and thus avoiding unwanted ionization saturation effects, is only possible in the loose focusing geometry. The diameter of the XUV radiation has to be expanded to at least a few mm in order to ensure these operating conditions. Loose focusing, together with the required XUV beam expansion, forces the beamline length to be in the order of several meters to tens of meters, according to optimization studies that have been presented in the literature [26, 58–60]. The highest XUV photon energy of the source can be controlled through the target gas type.

The phase 1 SYLOS laser chain will deliver pulses too long for isolated attosecond pulse generation; for this reason, a polarization gating device (PGD) has to be included in the described layout in order to confine the attosecond pulse train (APT) to a single pulse. The PGD may become redundant in phase 2 where the laser pulse duration is expected to be $\leqslant$5 fs.

Diagnostics of the XUV radiation refer to the spectrum, pulse energy, spatial beam profile and coherence, and pulse duration; the most demanding diagnostic setup is the temporal characterization of the attosecond pulses. Currently, there are very few—and by far uncompleted—comparative studies between existing temporal characterization approaches [61, 62]. Moreover, advanced versions of the existing approaches are envisaged for improved attosecond source parameters. The present beamline incorporates the two main options used today in attosecond pulse duration metrology, i.e. IR-XUV/x-ray cross-correlation and non-linear autocorrelation based approaches.

In those beamline areas where non-linear XUV processes are to be observed, high XUV intensities are required. These branches of the beamline are designed to minimize losses. In other areas which are intended for IR-XUV cross-beams, maximization of the XUV intensities is less important. Hence, further XUV reflecting elements can be introduced to increase the versatility of the branch to serve a larger number of experiments. Most of the instruments and setups used for the temporal pulse characterization contain general purpose instrumentation that can serve for user experiments.

Figure 14 shows the schematic layout of the beamline and the estimated parameters of the proposed beamline at the source are summarized in table 8.

3.3.2. VUV/XUV photon flux optimization. The aim of the high-order harmonic source in the COMPACT beamline is the most efficient conversion of the radiation from a few-cycle

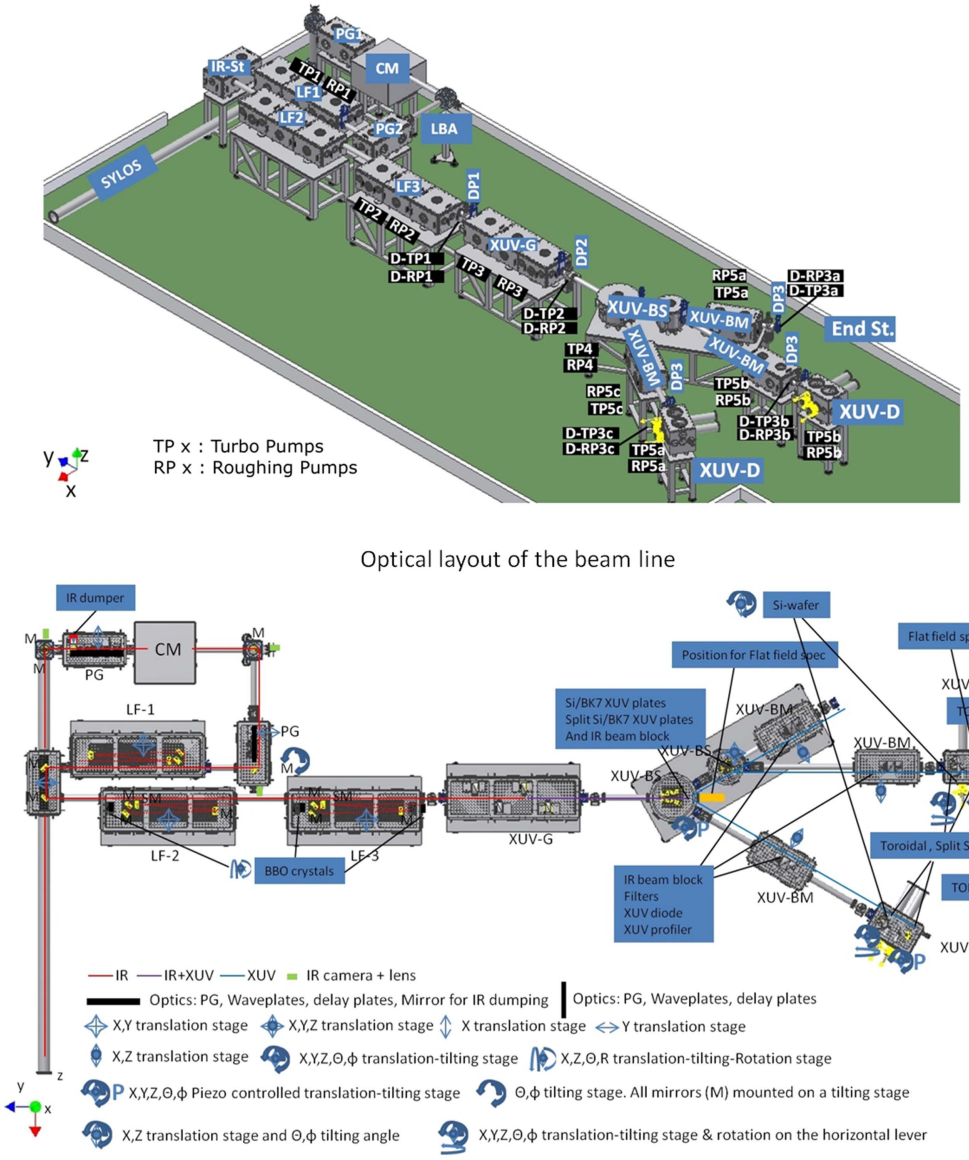

Figure 14. Schematic 3D layout of the beamline and top view of the optical layout.

Table 8. Ideal source parameters derived from fundamental laws. APT: Attosecond Pulse Trains; PG: Polarization Gating; FTL: Fourier Transform Limited.

Target gas	Xe		Kr		Ar		Ne		He	
Phase	1	2	1	2	1	2	1	2	1	2
APT cut-off maximum photon energy (eV)	38	40	54	57	56	59	136	145	291	308
PG maximum photon energy (eV)	42		60		62		154		325	
APT conversion efficiency/eV ($\times 10^{-6}$)	85	280	27.5	85	17.5	55	0.325	0.95	0.15	0.48
PG conversion efficiency/eV ($\times 10^{-6}$)	17	110	5.5	34	3.5	22	0.065	0.38	0.03	0.19
FTL APT pulse duration (as) (for $I_p < \hbar\omega < E_{cut\_off}$)[a]	>70	>64	>45	>42	>45	>42	>16	>15	>7	>6
FTL PG pulse duration (as) (for $I_p < \hbar\omega < E_{cut\_off}$)[a]	>60		>40		>40		>15		>6	

[a] *As pulse durations are not known for all cases the FTL values are given here as a lower limit.*

high-power IR laser into the XUV or soft x-rays; its design requires the consideration of the coherence length L_{coh} and the absorption length L_{abs} in relation to the length of the interacting medium L_{med}. The optimal conditions are $L_{med} > 3L_{abs}$ and $L_{coh} > 5L_{abs}$ [63], where $L_{coh} = \pi/(k_q - qk_0)$ with k_q and k_0 the wavevectors of the qth harmonic and the fundamental respectively, and L_{abs} the length where the qth harmonic is absorbed by a factor e^{-1}. Thus, the optimum condition is different for different harmonic order, and requires the design of the harmonic source to be flexible enough to allow for the

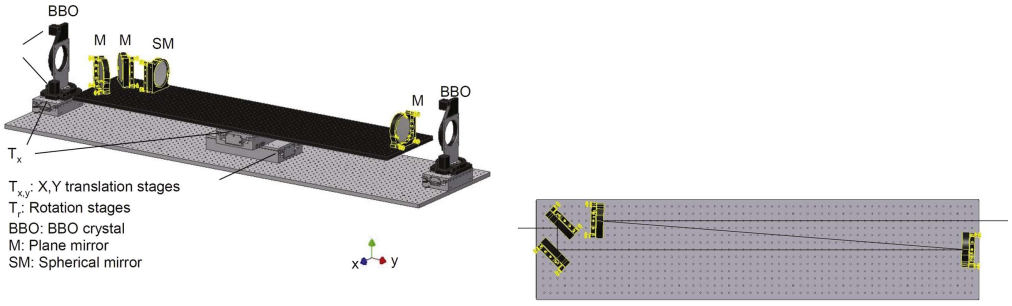

(a) Perspective view (b) Top view of the upper breadboard

Figure 15. IR beam focusing setup of the LF1 chamber.

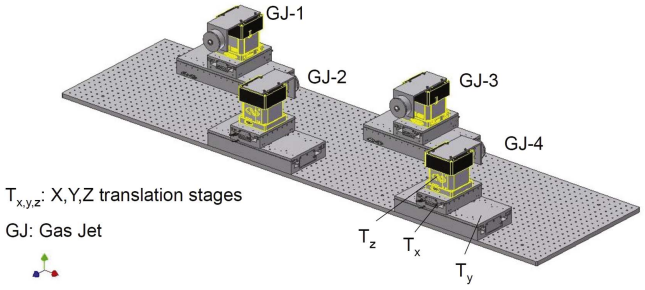

Figure 16. x,y,z translation stage setup on which four gas jets (GJ-1,2,3,4) can be fixed and remotely positioned with respect to the laser focus.

optimization of different harmonics for different applications. It has also been shown that when the coherence length is longer than both the absorption and medium lengths, the photon yield at the qth harmonic is proportional to $((1-\eta)I_0^5)^2 S_{\text{spot}} (PL_{\text{med}})^2$ [64, 65] where P is the gas pressure, η is the ionization probability, I_0 and S_{spot} are the laser intensity and spot area at the interaction region. Three important conclusions can be derived from this formula. The first is that the ionization rate should be low enough to avoid depletion of the medium. For noble gases, this condition limits the laser intensity to the range of $1 \times 10^{14} - 1 \times 10^{15}$ W cm^{-2}. The second conclusion is that an increased spot area increases the photon yield, and finally that a constant product (PL_{med}) results in the same photon yield. This last condition gives some flexibility in the source design. The objective to use the maximum possible laser power whilst keeping the intensity below a certain value dictates working with the loose focusing geometry. The focal lengths depend on the ionization saturation intensities of the non-linear medium and the driving pulse duration.

The highest photon energies emitted by an atom are given by the cut-off law [66] $E_{\text{cut-off}} = I_p + 3.17U_p$, $E_{\text{cut-off}}$ being the cut-off photon energy, I_p the ionization energy and U_p the ponderomotive energy. For rare gases the I_p increase with decreasing atomic number results in lighter atoms emitting higher photon energies but with a lower conversion efficiency. Thus, the optimum combination of photon energies and conversion efficiencies requires the use of different gases, which in turn have different ionization saturation intensities and thus require different focal lengths. For this reason, three different focal lengths (3, 6 and 10 m) are considered in the present beamline with the corresponding optical focusing setups in the three vacuum chambers LF1, 2 and 3 as shown in figure 14.

The short laser pulse duration and high pulse energies do not allow the use of refractive optics so reflecting optics are used, which force folding of the laser beam. Figure 15(a) shows the optical setup in the LF3 chamber. The incident laser beam is translated sidewise by two flat mirrors (twice 90° reflection) towards a third flat mirror, which reflects the beam towards the focusing concave spherical mirror. The angle of incidence is kept as small as possible ≈2° in order to avoid aberrations due to the departure from the normal incidence. With this setup, the focused beam is propagating on the same axis as the incident beam. The mirrors are fixed on remotely adjustable mirror mounts, which are placed on a breadboard that can be translated in the x and y directions by a remotely controllable xy translation stage. The translation stage is fixed on a second breadboard. Figure 15(b) is a top view of the upper breadboard and the mirror setup, showing a ray trace. This upper breadboard is the same in all three chambers (LF1, 2 and 3). Translation in the x direction controls the position of the focal spot with respect to the gas jet. Translation in the y direction brings the focusing setup in and out of the laser beam, depending upon the focal length to be used, i.e. which of the three focusing setups must be in the laser beam. Mounts for BBO crystals and waveplates are also placed in chambers LF2 and 3.

Two configurations of gas targets, a pulsed gas jet nozzle and a gas filled cell with pinholes for laser access, have been considered for the loose focusing geometry. Pulsed gas nozzles consume less gas, and offer the possibility of partial control over the contribution of the short and long electron trajectories [66, 67] to the HHG. The enhancement of the harmonic yield is also possible through quasi-phase-matching (QPM) techniques to counter the phase mismatch and increase the effective interaction length. QPM has been demonstrated in a multi gas cell target [68] and other arrangements [69]. A multi gas cell or multi gas jet target arrangement benefits from the loose focusing geometry as the Rayleigh range is long, and thus relative distances between the cells or nozzles can be easily selected and adjusted. A setup for multi jet operation is shown in figure 16. Four gas jets will be placed on four xyz translation stages, through

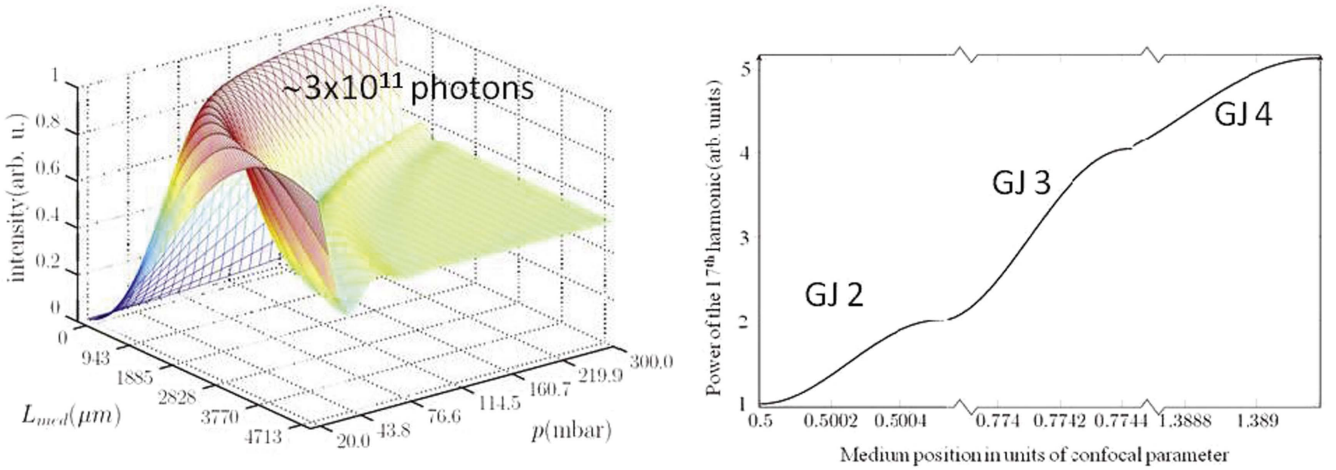

Figure 17. (a) Numerical simulations of the atomic response and phase matching in one argon jet showing the photon number of the 17th harmonic as a function of the argon gas length and pressure. The laser parameters are: pulse duration ≈5 fs, energy ≈100 mJ/pulse, carrier wavelength ≈800 nm and the focal length 10 m. (b) Demonstration of the 17th harmonic energy enhancement by additional gas jets (GJ 2–4) with argon gas at 50 mbar.

which appropriate positioning and selection of the jets can be remotely achieved.

The photon flux will be optimized by measuring the XUV pulse energy as a function of the position of the laser beam focus with respect to the gas jets and the gas pressure. Optimization of the photon flux should be performed in conjunction with the optimization of the XUV pulse duration. The trade-off between pulse energy and pulse duration depends upon the application. It is well known [62] that preferential harmonic emission by long electron trajectories may lead to an enhanced photon flux but at the cost of the pulse duration and attosecond confinement. If attosecond confinement is required, phase matching should be chosen so that the long trajectory contribution to the HHG process is minimized at the cost of the photon flux. The XUV pulse energy and pulse duration diagnostics are described in a separate section.

Figure 17(a) shows the numerical calculations including phase matching for the photon number of the 17th harmonic in a single argon jet as a function of the gas medium length and the gas pressure. The laser parameters considered in this calculation are pulse duration ≈5 fs, energy ≈100 mJ/pulse, carrier wavelength ≈800 nm and focal length 10 m. The optimized photon number for a constant product of gas length and pressure is $\approx 3 \times 10^{11}$photons per pulse, i.e. ≈1 μJ. Figure 17(b) shows the ≈5 times enhancement of the photon number in case of using a four gas jet configuration.

3.3.3. Generation of isolated attosecond pulses. The emission of isolated attosecond pulses for driving pulse durations >5 fs requires gating techniques that confine the XUV emission to less than one optical cycle. Thus, for the initial phase of the beamline operation, where the driving laser pulses will have a duration of about 10 fs, polarization gating (PG) [70] will be applied in order to confine attosecond emission to one pulse per driving pulse. The required CEP stability of the driving laser is fulfilled through the design of SYLOS. Two alternative positions in the beamline have been considered for the polarization gating, either before the laser pulse compressor, thus avoiding high laser intensities, or after, avoiding any possible polarization modification by the compressor. The two PG chambers are shown in figure 14. A wave plate PG (WPPG) [33] setup is used for the polarization gating that has similar configuration to [71], which is robust and suitable for 10 fs pulses. Figure 18 shows the WPPG configuration with the polarization control and polarization gating arrangements in the PG1 and PG2 chambers. In both cases, a pair of zero-order $\lambda/2$ and $\lambda/4$ waveplates define the initial polarization state. Then, a multiple order $\lambda/4$ waveplate and a zero-order $\lambda/4$ waveplate create a time-dependent polarization which is linear only during one half-cycle. A polarizing beam splitter (p-BS) controls the relative amplitudes of the two polarization components.

An alternative method is double optical gating (DOG) [72], which adds a second harmonic field to reduce the number of attosecond pulses to one per laser cycle, thus relaxing the gate width requirements. To this end a BBO crystal is utilized. Gating may become redundant in Phase 2, when the driving pulse becomes sufficiently short.

3.3.4. XUV beam separation, steering and manipulation. Figure 14 shows the optical layout of the XUV separation, steering and manipulation system, which is part of the beamline optical layout. The XUV radiation, co-propagating with the IR beam, enters the first beam steering XUV-BS chamber, where the annular IR component is blocked by a conical mirror aperture (CMA) while letting the XUV radiation pass through the central opening. The resulting beam is separated by a Si plate, which reflects the XUV whilst absorbing the IR radiation. AR coated fused silica will be used should silicon be damaged by the high power of the residual IR. The separated XUV is reflected either towards the

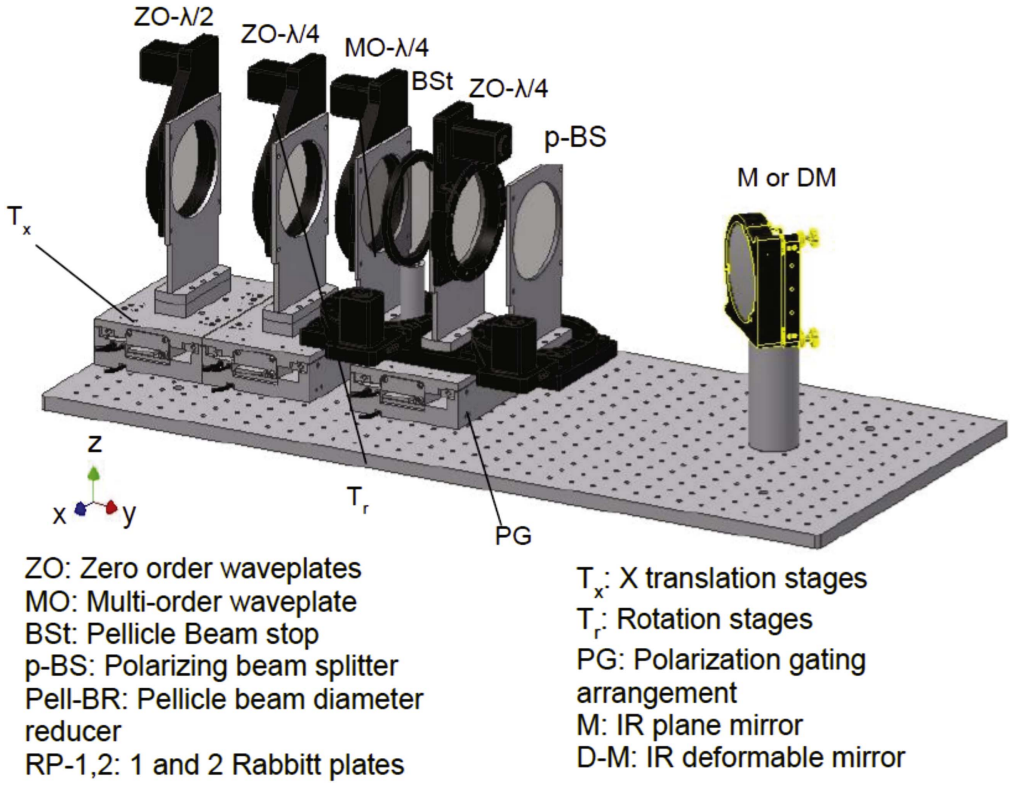

Figure 18. Polarization control and gating setup (PG2 chamber).

lower or upper branch, by selection of the appropriate reflecting plates.

The lower branch leads to one of the diagnostic chambers (XUV-D). Before entering this chamber, the radiation passes through a beam manipulation chamber (XUV-BM)—where another IR beam block (iris) removes residual IR more efficiently than was possible with the insufficiently expanded beam closer to the laser focus—and metal filters to select the XUV spectral region and absorb the remaining IR radiation.

For the diagnostics and use of the XUV radiation, the XUV beam is focused—either by a bisected spherical mirror or by the double toroidal mirror system—into a gas jet. A variable delay between the two XUV wavefronts is introduced by translating one half of the spherical mirror, which thus acts as a delay line on one half of the XUV beam for pulse duration measurements or XUV-pump-XUV-probe experiments. The spherical mirror is either a gold coated mirror or a multilayer mirror depending on the desired wavelength of the XUV radiation.

When the double toroidal mirror system is used, the Si (BK7) plates in the first XUV-BS chamber will be bisected plates mounted on translation stages including piezoelectric translation with few nm resolution of the one half plate. This alternative setup consists of two plates positioned side by side with a 50–100 μm gap between them. By translating the setup on the z axis, one can chose whether the XUV/IR beam will impinge on only one of the plates or both with the gap positioned at the center of the beam, thereby selecting either single plate or split plate operation. The delay is controlled by a piezo with attosecond resolution.

XUV radiation that is reflected into the upper branch can pass directly into an XUV-BM chamber that hosts a further beam block and filters and propagate further towards an end station. Alternatively, it can be deflected in the second XUV-BS chamber towards the second diagnostics chamber (upper XUV-D chamber in figure 14). This XUV-BS chamber is similar to the lower chamber but does not contain the split plate delay line.

3.3.5. XUV diagnostics and experimental areas. In figure 14, the lower right branch leads to the non-linear XUV diagnostics chamber XUV-D, the middle branch to the linear XUV-D.

Before entering the non-linear branch (XUV-D chamber), radiation passes through an XUV-BM chamber, where an XUV diode and an XUV profiler can be moved into the XUV beam in order to measure the pulse energy and the spatial intensity distribution of the XUV beam. The optical layout in the XUV-BM chambers is shown in figure 19. A CMA removes residual IR that was not previously blocked. Different XUV filters for different spectral ranges are selected by a remotely rotatable filter wheel. The XUV photodiode (XUV-PD) is calibrated for the absolute measurement of the XUV pulse energy and an XUV beam profiler (XUV-BP) consisting of a microchannel-plate detector (MCP) equipped with a phosphor screen anode can be used instead of the XUV-PD. A mirror reflects the image of the phosphor screen of the beam profile so that it can be observed from outside the chamber by a CCD camera.

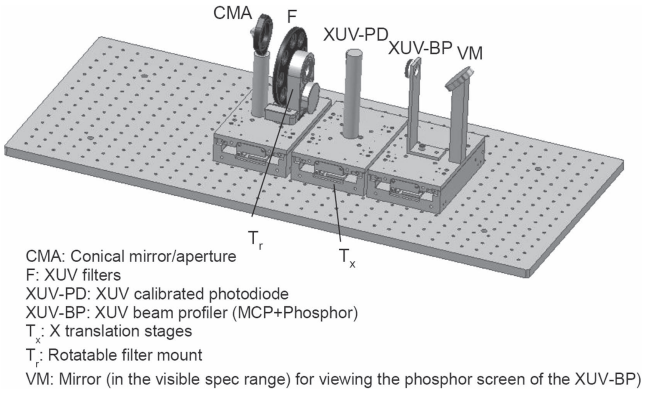

Figure 19. The optical layout of the XUV-BM chambers.

The duration of XUV pulses is measured in the XUV-D chamber through 2nd order intensity volume autocorrelation (2nd IVAC) measurements [73, 74], counting m/q resolved ions resulting from two-photon ionization as a function of the delay between two XUV pulses. At a later stage, through photoelectron spectroscopy, energy (and angularly) resolved 2nd IVAC can also be performed with the same experimental setup for a FROG type measurement.

In the linear diagnostic branch (middle branch in figure 14), a further XUV reflection from a second Si (or BK7) plate can be afforded because the IR-XUV cross-correlation measurements, such as reconstruction of attosecond beating by interference of two-photon transitions (RABITT) [75] or attosecond streaking type [76], can be carried out at lower XUV intensities since they depend only linearly on XUV flux. The delay is set between the XUV and IR pulse, which is achieved using a concentric plate arrangement described in [62].

A TOF spectrometer will be attached at two distinct chamber flanges corresponding to different focal positions of the spherical mirror or the toroidal mirror system. The focus of the spherical mirrors is close to the axis of the incident beam, whilst the focus of the toroidal system is higher since the system deflects the beam upward by 30°.

The XUV spectrum can be measured either before or after the spectral selection by the filter. Pre-filter measurements use a flat field XUV spectrometer placed in the first XUV-BS chamber directly in the XUV beam (orange box in figure 14), and for this measurement the Si (or BK7) plate is moved out of the beam. Post-filter measurements are made by the flat field XUV spectrometer attached to one of the two XUV-D chambers. The XUV radiation is deflected towards the spectrometer entrance either by the double toroidal mirror system (in which case it diverges when entering the spectrometer after going through a focus in the gas target) or by a Si wafer, located next to the toroidal mirror system just before the bisected mirror.

A detailed optical layout in top view and perspective view of the diagnostic chambers is shown in figure 20(a) and (b) respectively. The toroidal mirror system is placed near the entrance of the chamber on remotely controlled (x, z) translation and (θ, ϕ) tilting stages, allowing remote alignment of the focusing system. A Si (or BK7) plate, fixed in the x translation stage can be moved into the XUV beam reflecting it towards the flat field XUV spectrometer. The split spherical mirror setup is located at the end of the chamber. The setup provides the possibility of remote control of many degrees of freedom, as it can be (x, y) translated and (θ, ϕ) tilted. One half of the spherical mirror is attached to a feedback controlled long range (total movement $>400\,\mu$m) piezoelectric translator, allowing movement of this half on the z axis with <3 nm resolution. The other half is attached to two feedback controlled piezo tilting (θ, ϕ) and translation (z) stages with resolution $\leqslant 5$ mrad and $\leqslant 1$ nm.

Two pulsed gas jets oriented along the TOF spectrometer axes serve as gas targets. Their position is remotely controlled through xyz high vacuum manipulators. The gas jet nozzle also functions as the TOF repeller plate. For this purpose, the gas jet must be biased to the repeller potential and consequently the gas jet assemblies and piezo drivers have to be electrically floating. The two TOF spectrometers are shown attached to each chamber for the two focusing cases in figure 20.

The setups dedicated to the measurement of the spectrum and pulse duration can also be used in experiments including XUV-pump-XUV-probe ion or electron spectroscopy, XUV-IR or IR-XUV pump–probe experiments and transient absorption spectroscopy.

3.4. GHHG SYLOS LONG

The LONG GHHG beamline driven by SYLOS laser was designed to provide a single attosecond pulse (SAP) or an attoseond pulse train (APT) with the highest flux. The beamline's flexibility allows for easy reconfiguration between the two operation modes, and benefits from the optimized parameters of the driving laser (phase 1 and phase 2). It offers the possibility to perform pump–probe experiments with attosecond time synchronization between the pump and probe pulses and includes diagnostics for the complete temporal, spatial, and spectral characterization of the generated attosecond pulses.

The design of the GHHG beamline relies on a scaling concept, described in detail in [24, 77, 78], which scales up laboratory sized high-energy HHG beamlines, driven by commercially available laser systems [59, 79, 80], to the SYLOS parameters. A design based on a loose focusing geometry together with a long, non-guiding generation medium with low density is used. A block diagram of the beamline is presented in figure 21.

A switch between the operation modes is accomplished by changing the focal length, i.e. radius of curvature, of a deformable mirror implemented in the beamline as the focusing element, and gas cell length, whilst adjusting the beam size (by a variable aperture or by a telescope). The focused laser beam is folded in order to allow for a very loose focusing geometry, while limiting the total size of the system. Further reduction of the length is not possible due to the damage threshold of broadband high-reflective optics, critical in case of the last optical element before the focus. The beamline crosses four rooms. The IR beam manipulation and HHG cells are placed in the first three rooms (starting from

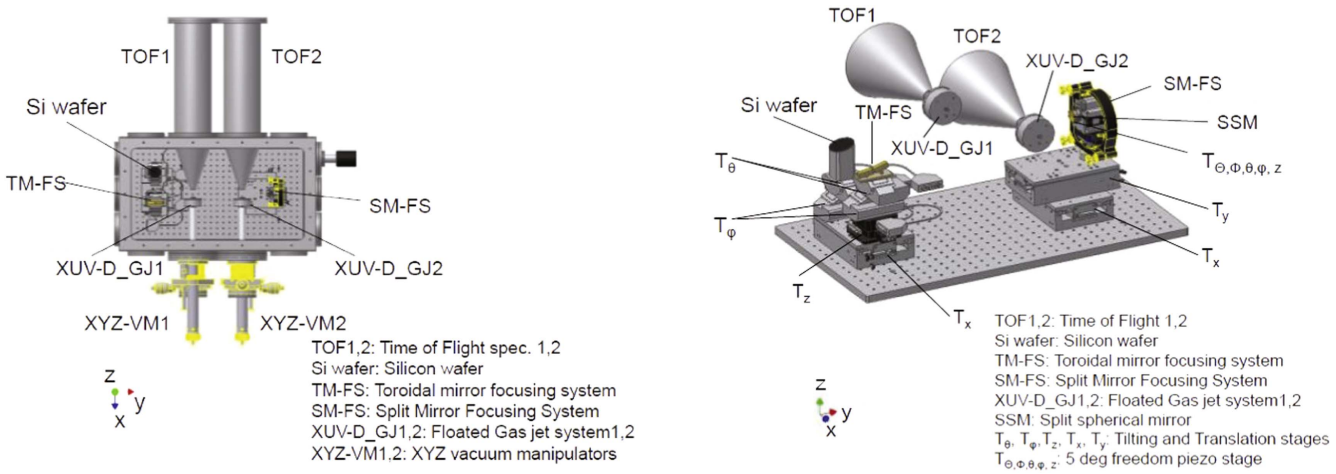

(a) Top view (b) Perspective view

Figure 20. Graphic representation of the components arranged inside the diagnostic chamber.

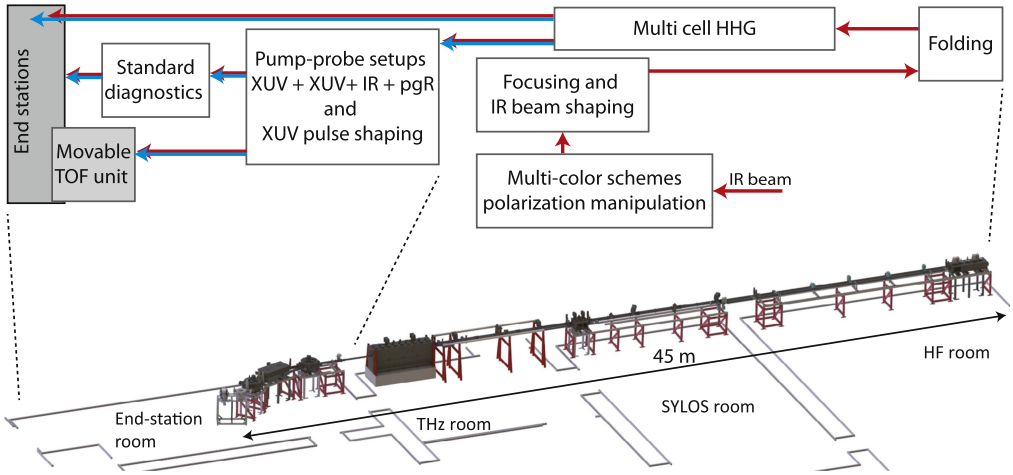

Figure 21. The GHHG beamline for development purposes. Multicolor schemes and polarization manipulation: interferometers for multicolor HHG and single attosecond pulse gating; pump–probe setup: a Mach–Zehnder interferometer (XUV/IR) combined with an XUV wavefront splitting unit (XUV/XUV) and a post-generation setup (pgR); Standard diagnostics: XUV and VUV spectrometers, XUV CCD camera; Movable TOF unit: electron and ion time of flight spectrometer mounted in a CAMP chamber together with a gas source and XUV refocusing optics.

right: HF, SYLOS, and THz room) whereas the pump–probe setup and diagnostics are located in an end station room.

An interferometric setup can be placed before the beamline entrance and used for IR spectral, temporal or spatial modification. The setup can be used for multicolor HHG or for testing new gating techniques like the attosecond lighthouse [81] or non-collinear optical gating [82].

High-order harmonics will be generated in a long, modular cell divided into sub-cells either independently filled with noble gases (Xe, Ar and Ne) at low pressure or evacuated. The design will allow us to investigate various generation schemes, including multiple cell generation [83] and quasi-phase-matching [84].

The fundamental and harmonic beams co-propagate to the pump–probe and diagnostic setup. The setup contains interferometers, filters, and IR/XUV diagnostics to separate and later recombine IR and harmonic beams (four pump–probe pulses including two single attosecond pulses or two attosecond pulse trains), adjust the time delay between the pulses, filter the harmonic spectrum and to temporally, spectrally, and spatially characterize the XUV and IR beams. Generated attosecond pulses can be sent from this unit to user end stations.

In the following subsections, the different parts of the setup are described in more detail.

3.4.1. Focusing geometry. Two different operation modes are considered, which imply different optimization parameters in order to achieve efficient SAP or APT generation with the highest possible XUV flux.

APT[12] is the operation mode where the highest conversion efficiency is obtained by broadband phase matching of

[12] APT1/2 refers to trains of attosecond pulses generated in phase 1/2 of the laser development.

the HHG process, operating at a level of ionization of a few % [24], in absorption-limited conditions. Scaling concepts are applied to obtain the highest possible flux, thus using long focal lengths, long media and low generating gas pressure. The driving IR beam is loosely focused into the gas, with intensity at the focus of a few 10^{14} W cm^{-2}.

SAP[13] operation mode requires the confinement of the HHG emission to one half-cycle of the IR field (~1.6 fs). Ionization gating [85] is planned to be used as the main SAP generation technique. The required peak intensity for ionization gating (>10^{15} W cm^{-2}) is well above the saturation intensity, at which most of the generation medium is ionized. In this regime, the field strength increases rapidly at the rising edge of the pulse, resulting in a steep ionization front. Only one half-cycle contributes significantly to HHG, whereas the generation from the following sub-cycles is suppressed due to depletion of the generation medium. There are two main requirements to obtain SAP with the ionization gating technique:

(i) Short pulse duration and high laser intensity in order to allow for efficient HHG during only one half-cycle of the laser.
(ii) Selection by spectral filtering of the continuous part of the HHG spectrum.

The first requirement (i) is easily achieved by the performance of the laser system. In SAP generation the intensity in the gas cell largely exceeds that necessary for APT and the second requirement (ii) can be achieved by using metallic filters.

The DOG technique described in section 3.5.3 will be used as an alternative method for SAP generation.

The generation of SAPs requires an intensity which is approximately one order of magnitude higher than for APT, so different focusing geometries for the two operation modes are considered. Furthermore, different focusing geometries are considered for development phases 1 and 2. An f-number ($f_{\#}$), focal length (f), and beam diameter (D) for each of the operation modes and phases are presented in table 9.

The optical setup is presented in figure 22. The laser beam propagates under vacuum into the THz room where it enters an optical setup (at 1.25 m height), which modifies the beam for different operation modes (telescoping, aperturing and focusing). The beam is first reflected by either two flat mirrors or two curved ones (M1 and M2). The flat mirrors are used for SAP1, APT1, and SAP2. The two curved mirrors (planned for APT2) constitute a telescope, which reduces the initial beam diameter to further increase $f_{\#}$. The angle of incidence on the mirrors is kept small to minimize wavefront distortions (reduced astigmatism). The focusing of the beam is carried out by a deformable mirror, which allows for automatic adjustment of the focal length in addition to compensation of aberrations. The beam is then raised to 1.75 m and this height is preserved in the other parts of the beamline. After focusing, the beam freely propagates in vacuum tubes towards retro-reflecting mirrors (mirrors RM1 or RM2 with each retro-reflector placed on a translation stage) in a chamber either in the SYLOS room or in the HF room. By using a combination of a translation stage and the deformable mirror, the focal length of the focusing system can be changed from 15 m to ∞ (unfocused beam) and can be adjusted by up to 3 m without moving the position of the focus.

[13] SAP1/2 refers to single attosecond pulse generated in phase 1/2 of the laser development.

Table 9. F-number (f #), focal length (f), beam diameter (D), cell length, and gas pressure for each of the operation modes and laser development phases.

	SAP		APT	
	Phase 1	Phase 2	Phase 1	Phase 2
$f_{\#}$	300	600	900	1100
f (m)	20	55	55	55
D (mm)	60	90	60	50
Cell length (m)	0.45	1.6	4	6
Gas pressure (mbar)	15	3.5	1.5	1

3.4.2. HHG cell. High-order harmonic generation is achieved in a cell filled with a noble gas (in particular Ar, Ne) and it is expected that phase matching can be achieved without using quasi-phase-matching techniques or a guiding cell geometry. Therefore, a gas cell geometry with constant pressure and constant diameter that exceeds the size of the focused beam is proposed.

Pressure and gas cell length were estimated by scaling up laboratory scale HHG sources operating at much shorter focusing geometries. The gas pressures in table 9 should be considered as an approximate value which will be optimized once the system is operational. The optimum gas pressure depends not only on the focusing geometry but also on other parameters such as dispersion, laser intensity and spectral range.

Two cell designs are optimized for different operation modes and laser development phases. For generation of high-order harmonics in the operation mode with lowest $f_{\#}$, SAP1, in the THz room (figure 22), the cell is constructed from a standard variable length bellows (range of 400 mm); this setup is called HHG1. To keep the total length constant while changing the cell length, a second bellows is added with the same free and compressed length.

The cell setup for generation in modes APT1, SAP2, APT2 (called HHG2) is divided into 15 sub-cells with a length of 400 mm. Neighboring cells are separated by a gate valve. The valve includes an exchangeable pinhole mounted on a movable part of the valve so that closing the valve introduces differential pumping between the cells and differential pumping conditions can be adjusted by changing the pinhole. The setup can be used as a single cell filled with one type of gas with variable length and position with respect to the laser focus. The cell length can be changed by filling different numbers of cells, whereas the cell position can be moved by filling different groups of cells and keeping the

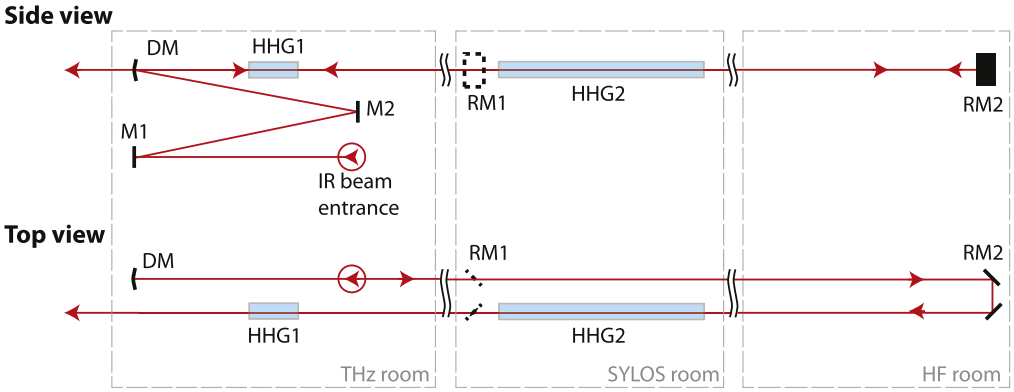

Figure 22. Focusing geometry. DM—deformable mirror, RM1/2—retro-reflecting mirrors for SAP1 and other operation modes, HHG1/2—HHG cell position for SAP1 and other operation modes.

other valves open. The setup provides flexibility to the development beamline, as it will allow scientists to explore new concepts such as quasi-phase matching (by modulation of the gas pressure in each cell) or multicolor and multicell generation (cells in series filled with different gases). All sub-cells of the unit are mounted on a rail system. Each differential pumping hole can be adjusted transversally with respect to the laser beam position.

Both setups, HHG1 and HHG2, have differential pumping sections at the beginning and at the end in order to achieve a pressure difference between the cell and neighboring vacuum sections. The diameter of differential pumping apertures was chosen to avoid clipping of the laser beam (for all modes) independently of the position of the focus with respect to the cell and also taking into account beam pointing fluctuation.

3.4.3. Pump–probe setup. The IR driving laser and the generated XUV radiation co-propagate towards the end station room, where the beams can take several optical paths and be directed towards different characterization instruments or split in pump–probe interferometers.

The beamline can provide various pump–probe schemes. By spectrally selecting particular XUV energy ranges, pump–probe experiments with two XUV pulses (XUV-XUV) at different central energies can be combined with IR radiation (XUV-XUV-IR) or post-generated radiation (XUV-XUV-IR-pgR) with pgR any of IR, second harmonic (SH), third harmonic (TH) or VUV). A multitude of schemes can therefore be envisaged for studies of ultrafast phenomena in biology, chemistry or physics.

The main unit of the sub-system is a Mach–Zehnder (M–Z) interferometer (figure 23), which can be used with a wavefront splitting unit (split-delay-unit, SDU) [86] and an additional arm (colored violet in figure 23). The main setup can be used for XUV-XUV-IR pump–probe experiments. The additional arm has a path length more than 30 cm ($>$ 1 ns) shorter than the interferometer path, which can transport an IR pre-pulse, e.g. for alignment of molecules, the generation of UV-VUV pulses created through second or third harmonic generation in non-linear crystals, or low- and high-order harmonic generation in gases.

The Mach–Zehnder interferometer takes advantage of the different divergence of the IR and harmonic beams, which provides a simple way of separating and recombining them using holey mirrors. The mirror inner hole size of 25 mm is larger than the expected XUV beam size. In one arm of the interferometer, the harmonic beam passes through a hole in the mirror and is reflected off the SDU and an AR coated fused silica plate at grazing incidence (10° grazing angle). This combination ensures suppression of the IR beam in this arm (IR transmission below 1%). The XUV reflectivity of the coated fused silica plates ranges from 50%–30% per reflection in the spectral range of 17 eV to 100 eV at 10° grazing angle. Depending on the application, the harmonic spectra may need further filtering to remove low-order harmonics or to select the cut-off spectral region in order to generate SAPs. This can be achieved using thin metallic filters, whose thickness and material composition determine the transmitted bandwidth. These filters can also provide some temporal compression of attosecond pulses by compensating the intrinsic HHG chirp [87], and remove any residual IR.

The SDU unit is based on wavefront splitting of the incoming radiation, and can serve for pump–probe experiments with XUV/XUV or VUV/VUV pulses. The unit is composed of two AR coated silica plates (optionally two high-reflectivity mirrors), which can be shifted and tilted with respect to each other. A parallel displacement of one of the two mirrors delays the reflected pulse relative to that from the second surface. The unit, at 10° grazing angle, has a scanning range of approximately 50 fs and a step size of 10 as [86].

The IR beam in the transport chamber can be directed towards the diagnostic chamber in order to create a third arm of the M–Z interferometer, using:

- metallic coated mirrors (e.g. gold) with a broad reflection range,
- AR coated plates (described above) to separate the IR and XUV beam or

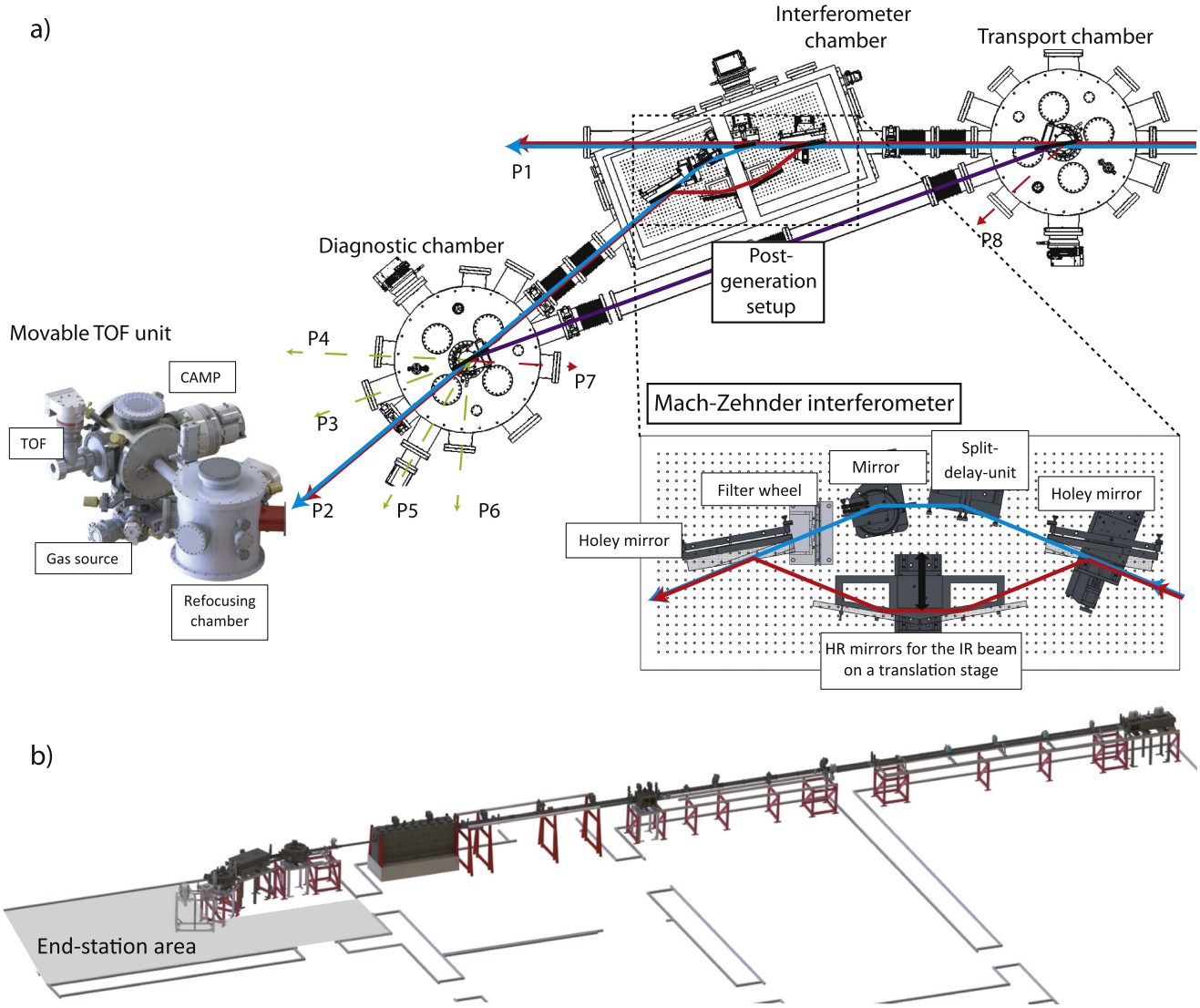

Figure 23. (a) The pump–probe setup: Mach–Zehnder interferometer with a split-delay-unit and additional arm (the violet beam path) for post-generation setups; (b) 3D view of the beamline with indicated space for dedicated and user end stations.

- holey mirrors to split or recombine pulses between the M–Z setup and the third arm.

These elements are placed on translation and rotation stages for remote alignment and adjustment of the incidence angle of the optics.

Depending on requirements, the following post-generation schemes can be added:

- SHG—a combination of a second harmonic generation crystal with a delay compensation quartz plate. Optionally an $\omega/2\omega$ interferometer can be used for the SHG process.
- THG—a combination of a second harmonic generation crystal, a delay compensation quartz plate, and sum frequency generation crystal. An $\omega/3\omega$ interferometer can be used for the THG process like the SHG scenario.
- Low-order Harmonic Generation or HHG. This setup requires an additional chamber, and is not planned at this stage of development. The chamber can be placed on an optical table located close to the setup.

3.4.4. Beamline diagnostics and end station/characterization ports. The arrangements of the mirrors in the diagnostic and transport chambers will redirect or split the incoming VUV, XUV, and IR radiation towards different application and characterization stations. The setup will initially be equipped with a gold mirror and an AR coated plate mounted on a translation and rotation stage.

The beamline offers a total arrangement of eight application and characterization ports. The highest XUV flux can be obtained at port P1 (figure 23) as no deflection is required and the Mach–Zehnder interferometer mirrors are moved out of the beam path. Possible uses of this port include a monochromator, a user end station with an implemented pump–probe setup or an experiment requiring only the IR beam. The second important port of the system is port P2, which uses the combined interferometers. Ports P3-P5 and P4-P6, respectively, are designed symmetrically so that each pair of ports has exactly the same properties. This offers convenience and flexibility to operators and users, e.g. the

XUV radiation sent to experiments in one application port can be characterized by its symmetric counterpart. Finally, two more ports (P7 and P8) are envisioned for the diagnostics of the auxiliary IR beam. The area planned for end stations is presented in an inset in figure 23.

The spectral characterization of the generated pulses in the beamline will be perfomed by two optical spectrometers: a VUV spectrometer (5–20 eV) for low-order harmonics and a high-resolution XUV spectrometer (20–200 eV) for high-order harmonics from different generation gases. Both devices are flat field spectrometers, which will provide valuable insight into the spatial properties of the beam. A CsI-coated imaging MCP is used as the VUV spectrometer detector, and the XUV spectrometer uses an uncoated imaging MCP. A calibrated back-illuminated XUV CCD camera will be used to characterize the spatial beam profile, and to measure the XUV pulse energy. The camera will have a 2048 $\times$ 2048 array of 13.5 μm pixels, to ensure high spatial resolution and ample field-of-view.

The beamline will be equipped with broadband XUV focusing optics, e.g. two toroidal mirrors in Wolter configuration, in order to tightly focus the XUV radiation while maintaining temporal properties. The estimated focal spot is less than 10 μm in diameter, resulting in high intensity ($>10^{13}$ W cm^{-2}) and making it possible to investigate non-linear phenomena in the extreme ultraviolet. Detection will be carried out by an ion/electron TOF spectrometer (electron energy of 20–200 eV and maximum ion mass up to 200 amu). The TOF is installed in a chamber based on the CAMP design [88]. The CAMP chamber standard, promoted by the Center for Free Electron Laser Science, allows users to attach directly compatible equipment, e.g. electron spectrometers, velocity map imaging (VMI) or TOF spectrometers. The TOF unit will be initially installed on port P2 for temporal characterization of APT/SAP. All diagnostics are planned as movable, interchangable units which can be connected to the beamline at different ports.

3.5. SHHG SYLOS development

The interaction of intense ultrashort lasers with solid density plasma reflecting surfaces, commonly called plasma mirrors (PM) can generate XUV high-order harmonics [89–92]. This form of coherent XUV emission from PM surfaces has shown great potential for development into an attosecond source in the time domain either in the form of attosecond pulse trains [93] or isolated attopulses [94–96]. The few-cycle SYLOS laser at ELI-ALPS facility provides a unique opportunity to access new heights of intensity with few-cycle pulses at high repetition rate of 1 kHz for laser PM interaction with controlled CEP. The SHHG SYLOS development beamline at ELI-ALPS aims to tap this unique potential to develop a flexible attosource for accessing diverse attoscience and plasma experiments [97–99].

Within this section, the physical mechanisms that would be utilized for SHHG are briefly mentioned and the relevant development beamline is described with special emphasis on its main features including the potential parameter space for the attosource which will be developed in the initial phase. The physical properties of SHHG will be compared with other HHG approaches (like gas HHG) to show its further development potential. Finally, the main challenges connected to the development of such a beamline for the generation of attosecond pulses on surfaces will be discussed, e.g. accomplishment of high-contrast driving pulses by plasma mirror, high rotation speed targets, collection and refocusing of the XUV radiation, and the temporal characterization of this radiation.

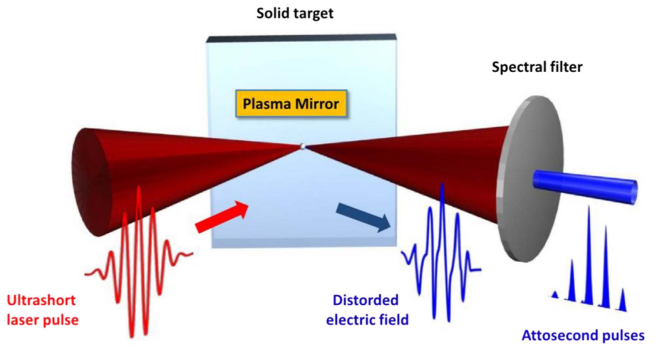

Figure 24. The mechanism of surface high-order harmonics generation from high intensity laser driven plasma mirror.

3.5.1. SHHG from plasma mirrors. Materials start breaking down and losing their distinct electronic structure in favour of more generic ionised collective state in the form of plasma at laser intensities beyond a threshold ($I \gtrsim 10^{12}$ W cm^{-2}). When an intense ($I \gtrsim 10^{17}$ W cm^{-2}) temporally clean [100] femtosecond laser pulse interacts with the surface of an initially flat solid target, it ionises and forms a very thin [92] highly reflective [101] plasma layer, in the rising part of the laser. The main part of the laser drives and interacts non-linearly with the PM [91]. The PM induces strong periodic temporal spikes in the reflected light field due to periodic relativistic electron dynamics [102] and when the fundamental laser carrier is spectrally filtered from the reflected beam, this can be observed as high-order harmonics in the spectral domain [102–105] or as attosecond pulse trains in the temporal domain [91, 93]. This is shown schematically in figure 24.

SHHG from PMs has received significant scientific attention and it has emerged, in addition to GHHG approaches, as a potential candidate for the development of intense coherent XUV attosecond light pulses, providing additional controls and complementary applications. The interaction of PMs with intense light is a highly active area of research due to its interdisciplinary applications in the fields of inertial confinement fusion research [106], laboratory astrophysics [106–109], development of laser-based high-energy particle accelerators [110, 111], highly energetic x-ray [112, 113] and THz [114, 115] photon sources and SHHG [89, 91, 92, 103]. Most importantly, SHHG from PMs has recently been demonstrated as an excellent metrology tool for solid density plasmas [98] providing information which has otherwise been inaccessible, making development of such a

source extremely promising for all the above mentioned studies.

Presently there are two SHHG processes from PMs that have been clearly observed, identified and distinguished both in experiment and simulations [102]. Each of these mechanisms needs p-polarized laser pulses to interact with the PM and will be utilized at ELI-ALPS in the SHHG SYLOS development beamline and these two methods will be briefly discussed.

Coherent wake emission (CWE). This mechanism dominates at relatively lower laser intensities ($I\lambda^2 \sim 10^{14} - 10^{18}$ W cm$^{-2}\mu$m^2). CWE can be visualised as a three step [90, 116] process where surface electron bunches are pulled out and accelerated into the vacuum in the combined laser field and the plasma field and then pulled back into the overdense plasma. Charge density waves are excited across the plasma density gradient in the wake of these returning surface electron bunches, and finally these plasma oscillations re-emit light specularly in the form of sub-cycle pulses. This process occurs periodically once in every optical cycle, and thus the spectrum of the associated emission contains the odd and even harmonics of the fundamental laser beam.

CWE harmonic emission spectrum presents a cut-off determined by the maximum plasma frequency, which depends on the nature of the solid target material [90, 102]. The harmonics extend up to the cut-off order $P_{\mathrm{CWE}} = \sqrt{n_{\mathrm{e}}^{\mathrm{max}}/n_{\mathrm{c}}}$, where n_{c} is the plasma critical density and $n_{\mathrm{e}}^{\mathrm{max}}$ is the maximum plasma electron density in the generating medium, and has also been observed in experiments (figure 25(a)). It has been seen in simulations (figure 25(b)) that CWE signal scales linearly with laser intensity in the regime $I\lambda^2 \sim 10^{14} - 10^{18}$ W cm$^{-2}\mu$m^2 [102].

Relativistic oscillating mirror (ROM). At higher intensities ($I\lambda^2 \gtrsim 10^{18}$ W cm$^{-2}\mu$m^2), electron motion becomes relativistic in the driving laser field [118]. The non-linear relativistic oscillation of the plasma reflecting surface leads to periodic Doppler shifts [104, 105, 119, 120] in the local reflected light field, leading to the generation of phase locked harmonic frequencies in the reflected laser spectrum. The harmonics generated in this process are called ROM harmonics [89, 91], because of the relativistic oscillating nature of the plasma mirror surface.

In the long-pulse petawatt class laser-solid interaction regime, high conversion efficiency ($\eta > 10^{-6}$ per harmonic) and high brightness emission ($>10^{22}$ photons s^{-1}mm^{-2}mrad^{-2}, 0.1% bandwidth) have been observed at wavelengths <4 nm for ROM from PM targets [117]. The initial part of SHHG spectrum includes the power law $I_n \sim n^{-8/3}$ for $n < \sqrt{8\alpha}\gamma_{\mathrm{max}}^3$, followed by exponential decay (figure 26) [103, 105] where γ_{max} is the maximum relativistic γ factor of the plasma surface, and α is the second derivative of the surface velocity at this moment. These studies demonstrate that both the strength (figure 26(i)) and the frequency span (figure 26(ii)) of these newly synthesized frequencies strongly depend on the intensity of the incident laser field. This regime therefore becomes extremely promising for generating intense attosecond pulses in the soft x-ray region

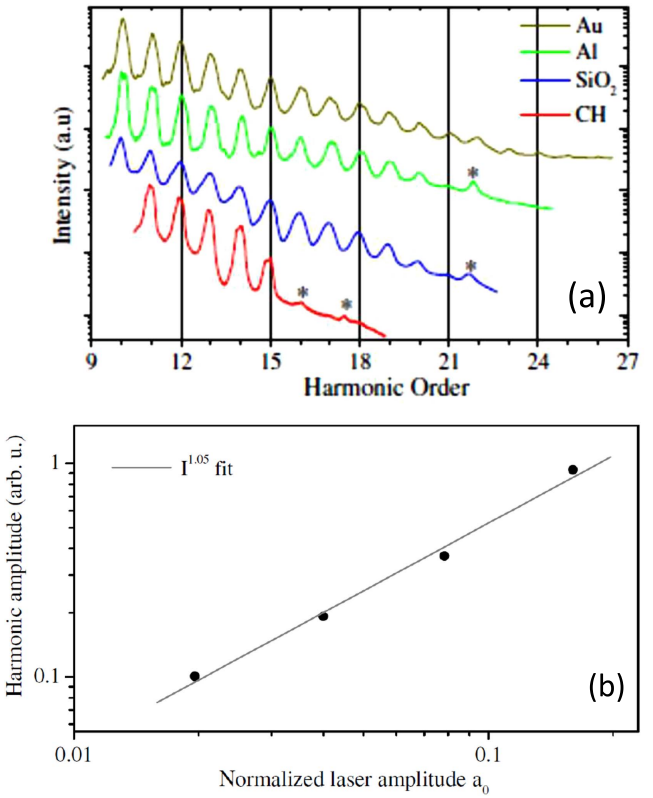

Figure 25. (a) CWE harmonic spectra obtained at an intensity of 3×10^{18} W cm^{-2}, on targets of different initial densities. The stars indicate incoherent plasma line emission. (b) Scaling of harmonic strength integrated between orders 4–10 with laser intensity. The normalized laser amplitude is given by $a_0 = 0.85 \times 10^9 (I\lambda^2)^{1/2}$, where I is laser intensity in W cm^{-2} and λ laser central wavelength in μm. These are results obtained with the 2D3V particle in cell simulation code CALDER for $L/\lambda = 1/30$ and $n_{\mathrm{e}}^{\mathrm{max}} = 110 n_{\mathrm{c}}$. (a) [101] (2017). Figure reprinted with permission of Springer. (b) Reproduced from [102]. © IOP Publishing Ltd. All rights reserved.

if the plasma mirror can be driven at very high intensities using state-of-the-art lasers.

Surface high-order harmonic signals associated with these two mechanisms have distinctive features that can easily be differentiated in experiments. The different properties manifest in the spectral extension [89, 90, 101], intensity dependence and spatio-spectral phase characteristics [91, 98, 102, 116, 129]. These are also the features that in turn determine the divergence of the harmonic signal and its spatial and temporal properties. One of the most important parameters that controls the relative efficiencies of the harmonic generation mechanisms, and hence all the above mentioned distinctive features, is the ratio of plasma density gradient length to the laser wavelength, L/λ. The SHHG process is observed to sensitively depend on the sharpness of the PM [92, 130, 131].

3.5.2. The complementarity of SHHG and GHHG processes.

The brief three step process description of CWE in section 3.5.1 is reminiscent of the Simpleman's model of

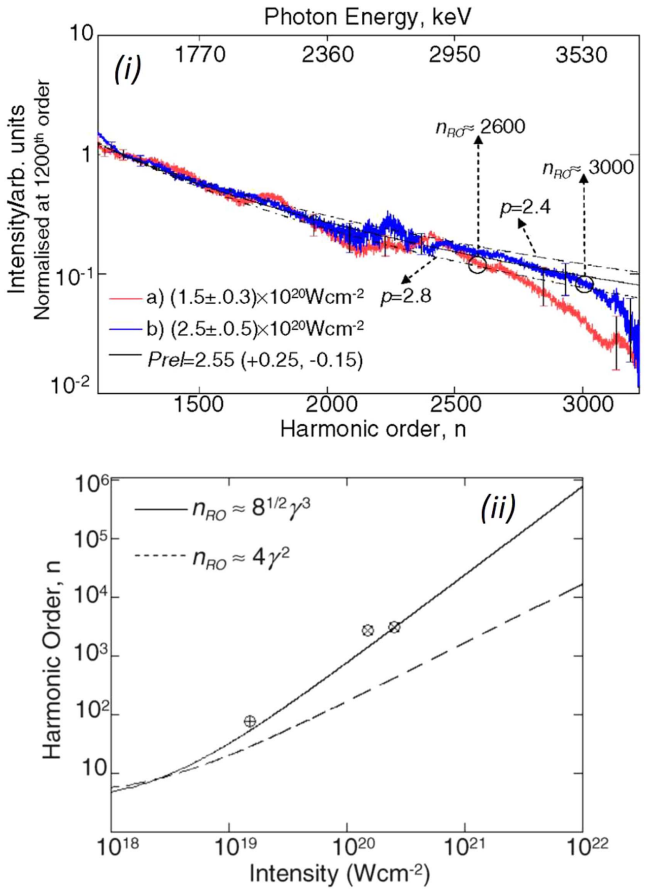

Figure 26. (i) ROM high-harmonic strengths at two different drive laser intensities: (a) $(1.5 \pm 0.3) \times 10^{20}$ W cm^{-2}, gray (red) trace and (b) $(2.5 \pm 0.5) \times 10^{20}$ W cm^{-2}, black (blue) trace. The lines are power law fits to the data such that $I(n)/I(1200) = n^{-p}/1200^{-p}$, with p as the fitting parameter. The best fit (solid line) is achieved for a value of $p_{\rm rel} = 2.55$. (ii) Scaling for the maximum relativistic limit harmonic order $n_{\rm RO}$ with experimentally observed data and better agreement found with $8^{1/2}\gamma^3$ scaling than $4\gamma^2$ scaling. Reprinted figure with permission from [117]. Copyright (2017) by the American Physical Society.

GHHG: ionization, acceleration and recollision. However, there are striking differences between the two approaches because SHHG is inherently a collective plasma mechanism, whereas GHHG works within the single active electron approximation. This intuitive resemblance breaks down further when collective oscillations become relativistic in the case of efficient ROM. The special features of SHHG are discussed below, and this knowledge is a prerequisite for understanding the requirements of a state-of-the-art SHHG development beamline:

- SHHG is most efficient at extreme intensities, and this puts stringent conditions on pulse contrast on spatial (aberration corrected) and temporal (temporally clean) domain, with special attention needed to avoid spurious spatio-temporal couplings that can diminish the effective intensity at focus [132]. This also necessitates stricter target alignment conditions due to the tighter focusing geometry and the target needs to be replenished after each laser shot, unlike GHHG. Active target stabilization at high repetition rate with very high accuracy is a critical feature.
- Surface-generated high-order harmonics contain both odd and even harmonics, due to lack of inversion symmetry [103, 133], unlike GHHG. Consequently, attosecond bursts from plasma mirror are emitted once every cycle of the driving laser [99], whereas the emission occurs twice every cycle in the case of gas harmonics [134]. This may give a slight advantage for generating isolated attosecond pulses using the lighthouse technique, which relies on ultrafast wavefront rotation of the driving laser at the focus [81, 94]. The SHHG implementation is expected to be more effective as the attosecond bursts have greater temporal separation. More details can be found in section 3.5.3.
- Optical control of plasma mirrors (control over plasma density and the plasma density scale length or the steepness of the plasma) allows significant influence on the spectral and spatial properties of SHHG [92]. Even spatial structuring of the plasma mirror is a way to control laser-plasma interactions and thus high-order harmonics generation. Divergence control of the generated surface harmonics by precise control over the curvature of the plasma mirror has already been demonstrated [91]. Further control of the plasma mirror surface by creating optically tunable micro-plasma ripples [135] has created new tools in plasma metrology, and allowed the complete characterization of SHHG source spatial properties [98].
- Electron acceleration in intense coherent laser field is one of the very promising areas of research that has a multitude of applications. Recent observations have demonstrated the feasibility of accelerating nC bunches of electrons to high energy with quasi-monoenergetic features [110] and in plasma mirrors, the same electron dynamics is responsible for SHHG with the harmonics carrying information about the plasma dynamics. Accelerated particles could be used as novel probes to investigate and control attosecond electron dynamics in laser-plasma interaction [98, 99]. There is a striking correlation between accelerated particles and up-shifted SHHG photons [111].

Table 10 summarizes the complementary nature of the GHHG and SHHG processes. An appreciation of these basic differences between the physical processes involved in GHHG and SHHG would facilitate a deeper understanding of the challenges involved in developing a state-of-the-art SHHG beamline, like SHHG SYLOS. It would also illustrate the usefulness and limitations of adapting already existing space-time metrology tools from the GHHG domain to SHHG.

3.5.3. Major challenges in SHHG beamline development.

SHHG driven by few-cycle waveform-controlled high repetition rate laser beam at relativistic intensities offers a few unique challenges, as well as many advantages. Some of

Table 10. Summary of the complementary nature of high-order harmonics generated from a gaseous medium and via relativistic excitation of a plasma mirror, in the case of linearly polarized single color driver.

Properties	Gas HHG (atomic case)	Surface HHG
HHG spectrum	Odd harmonics	Both odd and even harmonics
Attosecond bursts per cycle	Twice in every cycle	Once in every cycle
HHG Cut-off & intensity	Limited by saturation intensity. Harmonic intensity and cut-off drops after saturation intensity [24, 121, 122]	No such limit. Harmonic intensity scales up with laser intensity & harmonic cut-off either depends on the material (CWE) [90, 101] or increases with laser intensity (ROM) [89, 105, 117].
Phase matching	GHHG occurs in transmission mode. Proper phase matching during propagation is needed for intense harmonics. Harmonic properties depend on phase matching condition [123–125].	SHHG takes place in the reflection mode. Phase matching condition is intrinsically satisfied [102].
Spatio-Temporal coupling (STC)	GHHG emission is fundamentally space-time coupled irrespective of the phase matching conditions [126]	There is no fundamental STC in SHHG emission [91]
HHG as a probe of the source	GHHG are being used to extract information about atomic & molecular structures [127, 128]	SHHG have been used in to extract information on attosecond electron dynamics in μ-scale plasma [98, 99, 116]

these challenges need the extension and development of current state-of-the-art technology. Other problems depend upon novel unchartered R&D activities.

Target operation at kHz repetition rates. SHHG at kHz repetition rate requires the rapid motion of a flat solid target (several cm s^{-1}) and there are three conditions that must be fulfilled:

(i) Each consecutive laser pulse must interact with an optical quality surface. The surface has to be continuously refreshed.
(ii) There must be identical and repeatable interaction conditions for each laser shot. The laser Rayleigh length is usually extremely short to reach ultra-high intensity and the surface must be actively stabilized with sub-micrometric precision.
(iii) The target has to have sufficiently large surface area to allow long continuous operation times ($\sim$1 h) at 1 kHz. This is sufficient for performing statistically meaningful parametric studies with attosecond time resolution before the target is replaced.

The minimization of time for target replacement also necessitates the incorporation into the beamline of a vacuum design and pumping assembly that allows for rapid chamber opening and closing. Finally, working at kHz repetition rate for laser-plasma interaction could be challenging because of laser ablation of the target. At high repetition rate, target material would be ablated, and ways have to be found to mitigate undesirable material coating of the precision optics resulting in their degradation.

High temporal contrast for driving laser. To generate collimated good quality harmonics, the interaction should take place with the initial PM surface having roughness significantly less than the wavelength (λ) of the incident light [130, 136] and a very steep step-like density gradient [92]. For this reason, SHHG driving lasers must have very high temporal contrast [102]. Very precise control over the plasma profile, which is already very thin, gives control over harmonic efficiencies and their spatial properties [91, 92]. This precise control will be effective only when the main driving laser has very high temporal contrast, so that it does not produce any long pre-plasmas. Achieving this high temporal contrast of the driving laser needs a temporal cleaning device operable at kHz repetition rate in the beamline.

High spatial contrast at the focal spot. SHHG requires the optimization of the on-target laser intensity at the focal plane. The beam needs precise aberration control as the drive laser is tightly focussed. Additionally, thermal deformations of the reflecting optics, that support the high bandwidth and high flux 1 kHz SYLOS, would also introduce extra aberrations into the main beam. All these factors necessitate use of a high quality wavefront sensor coupled to an adaptive optics assembly that would correct for wavefront aberrations to optimize the focal spot. The standard adaptive optics is usually a deformable mirror with feedback control, and only corrects for aberrations at the central wavelength (or any other predefined λ) of the drive pulse. How this relates to wavefront correction in the case of a broadband pulse is a matter for further investigation. The beamline envisions using spatio-temporal coupling of the main pulse to control the spatial dispersion of attosecond pulses [137], and this is well known to affect the focal spot shape and intensity [132]. Aberration correction of a laser with spatio-temporal couplings will also need special attention.

Generation of isolated attosecond pulses from PM. A CEP stabilized single cycle pulse is required to generate a single attosecond pulse. For a many-cycle pulse, methods like the polarization gating [70] can be used but it has yet to be tested for SHHG. The generation of single isolated attosecond

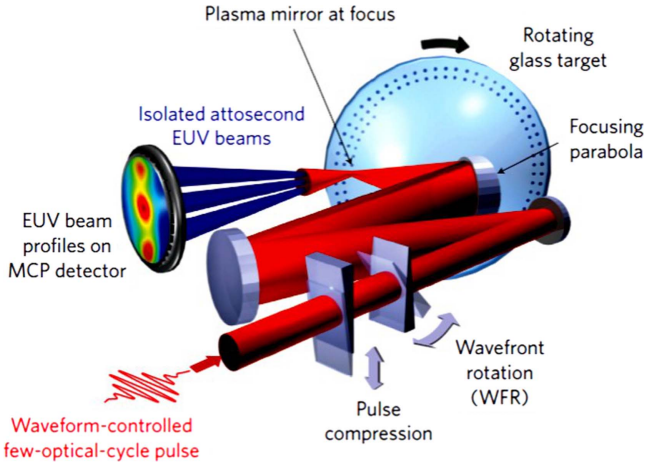

Figure 27. A waveform-controlled few-cycle IR laser pulse is focused onto a rotating optically polished target surface creating a plasma mirror. XUV radiation, in the form of an attosecond pulse train, is non-linearly generated in the direction of the reflected laser beam through the process of either coherent wake emission or relativistic oscillating mirror. Wavefront rotation (WFR) is introduced at focus by tilting one of the prisms used before focusing on target. The spatial beam profile of the XUV radiation is directly imaged onto an MCP detector. Increase in WFR at focus, splits the generated XUV beam into spatially separated beamlets, each embodying a single isolated attosecond pulse. [94] (2017) Figure reprinted with permission of Springer.

pulses has not yet been explored in SHHG, and only one such experimental attempt has been reported [93].

Isolated attosecond pulse generation has been reported by Wheeler *et al* [94]. The authors have introduced a technique known as the attosecond lighthouse to disperse attosecond light pulses from an attosecond pulse train [81, 94] generated by the interaction of a plasma mirror and an intense multi-cycle laser pulse, by using instantaneous wavefront rotation at the focus. The wavefront rotation was introduced by tilting a prism in the main beam path as shown in figure 27.

The basic principle of the attosecond lighthouse [81] is depicted in figure 28. When an intense few-cycle laser pulse, without any wavefront rotation, interacts non-linearly with a plasma mirror, the sub-cycle modulation of the temporal laser wavefronts is associated with the generation of a train of attosecond light pulses, which all propagate in a collimated beam along the direction normal to the laser wavefronts at focus as shown in figure 28(a). The situation is completely different when wavefront rotation in time at focus is introduced by a tilting prism. Each attosecond pulse of the train is emitted in a slightly different direction. When the wavefront rotation angle is greater than the divergence of an individual attosecond pulse, as described in [81], this scheme produces a manifold of spatially isolated and temporally synchronized attosecond pulses.

Time domain metrology of attosecond pulses from PM. Most attosecond measurement techniques are developed for high-order harmonics generated from gaseous media. Attosecond pulse measurement for SHHG is challenging because of the following reasons:

(i) SHHG sources are driven by higher power lasers, which are limited by their lower repetition rate. Almost all attosecond measurement techniques require large statistics. Therefore, these attosecond measurement techniques can be applied to SHHG-produced harmonic radiation only after major modifications. Well established techniques, like autocorrelation, for time domain metrology for SHHG [93] need more control at high intensity.

(ii) Both odd and even order harmonics are present in the harmonics spectrum. Current attosecond measurement techniques such as RABITT cannot be directly used [125]. A promising alternative would be phase retrieval by omega oscillation filtering (PROOF) [125, 138], which operates in the perturbative regime and can measure arbitrary XUV pulse shapes.

(iii) The majority of SHHG experiments have been performed using many-cycle laser pulses due to the limited availability of few-cycle high peak power lasers. Under the prevailing conditions, these drivers generally produce APTs rather than isolated pulses. Pulse characterization techniques like attosecond streaking [3, 125, 139] with a fundamental laser streaking field require a long and precise pump–probe delay scan for the complete determination of the attosecond pulse profile. A streaking-type measurement can also characterize an APT very well, as long as the spectral resolution is sufficient and an accurate scan is carried out over quite a wide temporal overlap. These methods need to be adapted for the case of attosecond pulse trains generated at comparatively lower repetition rate. A promising possibility would be to employ a THz or far-IR streaking field, which can be used to map an attosecond pulse train [140, 141] in a single shot.

Focusing SHHG on target. The focusing of attosecond light pulses is a stringent requirement for attosecond pump–probe experiments. This is challenging due to optical aberration, which spreads the attosecond light pulses in both time and space. All focusing optics (in this case, spherical or toroidal mirrors) can induce geometric aberrations due to the geometric shape of the mirrors [142]. However, tight focusing is a mandatory requirement for achieving high intensity in attosecond XUV pulses, and this must drive R&D on the correct approach for XUV focusing and space-time matching of the different pump–probe configurations.

3.5.4. A brief description of SHHG SYLOS development beamline. The SYLOS laser will be able to deliver laser pulses with enough intensity to drive SHHG via CWE as well as ROM; such an intense CEP controlled, few-cycle laser at kHz repetition rate has never been utilized for SHHG. Therefore the design of the proposed SHHG SYLOS development beamline would capitalize on the state-of-the-art

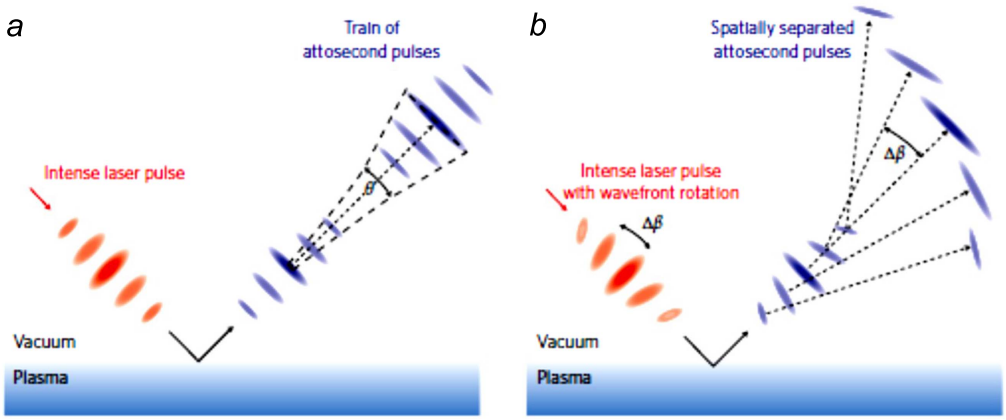

Figure 28. The basic principle of the attosecond lighthouse. (a) Attosecond pulse train from pulses without wavefront rotation. (b) Attosecond pulse train from pulses with wavefront rotation. [94] (2017) Figure reprinted with permission of Springer.

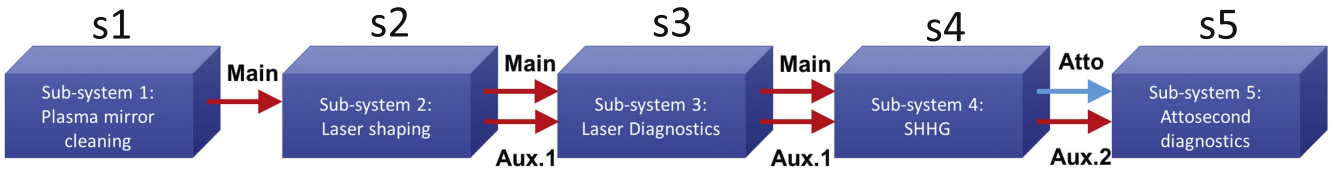

Figure 29. Block diagram of the proposed SYLOS SHHG beamline at ELI-ALPS. Red arrows indicate the Main and Auxiliary IR pulses while the blue arrow indicates the attosecond XUV pulses.

SHHG developments, and adapt them by extending the system to the unique parameters of SYLOS. The recently developed plasma mirror target technology [143] for SHHG sources driven by intense waveform-controlled few-cycle laser pulses [94, 99] would be scaled up to accommodate the SYLOS parameters. This beamline consists of a single flexible design capable of driving SHHG in both CWE and ROM regimes by only changing the focusing conditions:

- **Low Contrast mode** (**LC**)—The initial laser contrast is not modified and soft focusing is used ($f\# > f/6$) to limit IR intensity on the target to $<10^{18}$ W cm^{-2} and to restrict SHHG to the CWE regime ($E_{\text{photon}} \approx$ 8–45 eV).
- **High Contrast mode** (**HC**)—The initial laser contrast is enhanced by sending the beam through the PM contrast cleaning stage and tight focusing is used ($f\# \approx f/1.5$) to reach on-target intensities $\sim 10^{19}$–10^{20} W/cm^2 and to push SHHG into the ROM regime ($E_{\text{photon}} \approx$ 8–100 eV).

The generated harmonics and their attosecond temporal structure will be controlled via the following parameters:

(i) **Laser properties**—Driving laser intensity, polarization, pre-pulse contrast etc are the parameters that could affect the surface harmonics generation and will be investigated thoroughly and then implemented in the SHHG beamline. Spatial and temporal shaping of the laser beam will also be implemented.

(ii) **Plasma properties**—Plasma properties have a dramatic effect in high-order harmonics generation, most notably the plasma scale length which changes the collimation and cut-off of the harmonics. Furthermore, a plasma grating will be implemented to determine the XUV source size [135].

The beamline is divided into five sub-systems (figure 29):

s1—**Plasma Mirror Contrast Cleaning** for switching between LC and HC modes.
s2—**Laser Shaping** for spatio-temporal shaping of main and auxiliary IR beams.
s3—**Laser Diagnostics** for spatio-temporal characterization of main and auxiliary IR beams.
s4—**SHHG** for generating XUV attosecond pulses from an IR-driven plasma mirror.
s5—**Attosecond Diagnostics** for spatio-temporal characterization of the attosecond XUV pulses.

The detailed functional diagram and the three-dimensional design of the beamline is presented in figure 30. The SYLOS laser beam propagates into the first vacuum chamber (sub-system s1, figure 30), where it can be directed through a single-pass PM device synchronized with SYLOS at 1 kHz, which improves the laser temporal contrast by $>10^2$ and enables the beamline to operate in HC mode. In LC mode, the beam passes through the chamber unaffected. This unit features all-reflective attenuation optics for alignment purposes as well as automated beam pointing correction and stabilization optics.

The main beam (Main) then propagates into a second vacuum chamber (sub-system s2), where the first auxiliary IR beam (Aux. 1) is generated by extracting a fraction of the high-energy Main beam. Aux. 1 is spatially shaped and sent through a variable delay line, with respect to Main, in order to

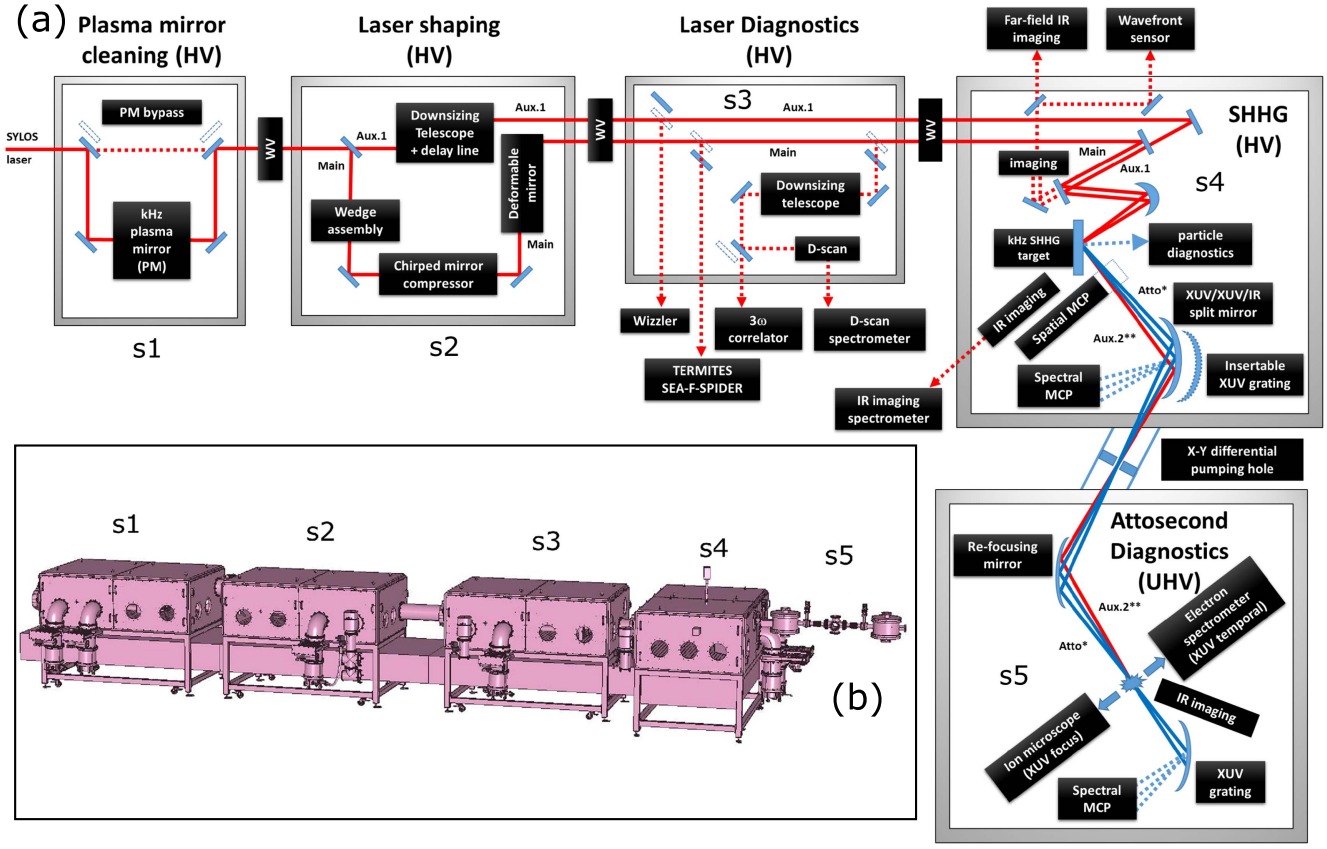

Figure 30. (a) Schematic optical layout of the beamline. (b) 3D view of the SHHG SYLOS beamline design showing the different sub systems s1-5. The SYLOS laser entry to the beam line is from the left of the figure.

control the plasma density gradient on the SHHG target downstream in sub-system s4. The Main beam is sent through a wedge pair assembly to achieve spatially isolated SAP generation via the attosecond lighthouse effect [81, 94]. Subsequently it then goes through a chirped mirror compressor in order to optimize temporal compression on the SHHG target in sub-system s4 while minimizing B-integral effects inside the bulk material of the wedges. Main is finally sent onto a deformable mirror to correct wavefront aberrations and to optimize the focus on the SHHG target in sub-system s4.

The Main and Aux. 1 beams then propagate into the third vacuum chamber (sub-system s3) which contains insertable beam sampling optics used to send the IR pulses to be characterized in the following manner:

- Temporal profile of Aux. 1 (Wizzler by FASTLITE or FROG outside the chamber)
- Temporal profile of Main under vacuum (D-SCAN [144] with spectrometer outside the chamber, Wizzler inside the chamber)
- Temporal contrast of Main (SEQUOIA by Amplitude Technologies or TUNDRA by Ultrafast Innovations outside the chamber)
- Spatio-temporal couplings of Main (TERMITES [145] or SEA-F-SPIDER [146] outside the chamber)

Sub-system s3 also recombines the Main and Aux. 1 beams and they co-propagate side-by-side into the fourth vacuum chamber (sub-system s4) which features:

- Online beam sampling to measure the Main beam wavefront
- Online beam sampling to optimize both focusing and overlap of Main and Aux. 1 beams on target
- Two focusing configurations (for Main and Aux. 1) to switch between LC and HC modes
- An optically stabilized SHHG plasma mirror target device synchronized with SYLOS at 1 kHz
- Online electron and ion detectors to optimize the laser-plasma interaction conditions
- Insertable spatial and spectral detectors to optimize the SHHG regime
- Attosecond XUV pulses (Atto) generated by SHHG
- Few-femtosecond auxiliary IR pulse (Aux. 2): A selected part of the Main beam reflected by the SHHG plasma mirror
- Split-mirror assembly, synchronizing and refocusing Atto and Aux. 2 pulses into sub-system s5.

Both Atto and Aux. 2 pulses are then sent into a fifth chamber (sub-system s5) where they can be used for attosecond pump–probe experiments. Both XUV and IR beams are focused through a mm size differential pumping hole ensuring UHV conditions inside the sub-system s5

where both the Atto and Aux. 2 pulses can be spatially, spectrally and temporally characterized. This chamber can be easily modified to accommodate user experiments.

3.5.5. Detailed description of the five sub-systems of SHHG SYLOS development beamline. The complete beamline with all the separate sub-systems is shown in figure 30. The functionality (figure 30(a)) and the constituent components (figure 30(b)) of each of the five sub-systems are discussed below in detail.

Sub-system s1: Plasma mirror for pulse contrast cleaning. This part of the system improves the temporal contrast of the driving laser beam by suppressing pre-pulses and preceding pulse pedestals. High-power lasers contain nanosecond-advanced pre-pulse and picosecond-wide pedestals which, when focused on a solid surface, produce a pre-plasma and diminish the steepness of the plasma mirror (increased plasma scale length), with highly detrimental effects on the spatio-temporal properties as well as the efficiency of the SHHG process [92]. Hence a driving laser pulse with high temporal contrast is desired so that no pre-plasma is created. A plasma mirror for pre-pulse cleaning will be developed [100, 147], based on a rotating round (∅ 40 cm) optically polished substrate [99] with sub-500 μrad angular stability. The high temporal contrast already provided by the SYLOS laser will enable this PM device to work in a regime of significantly higher peak intensity than previous implementations. This allows for a smaller laser spot size and closer shot spacing and thus optimizes the available PM surface which is refreshed for each laser shot at 1 kHz repetition rate.

Sub-system s2: Main and Auxiliary laser beam shaping. This sub-system spatio-temporally shapes the few-cycle driving beam. The SYLOS pulses will enter the beamline with a negative chirp, that is fully compensated for by a combination of a pair of quartz wedge plates and a set of dielectric chirped mirrors. The wedges also introduce the angular dispersion used in the attosecond lighthouse method [81]. Any other spatial and temporal shaping required for experiments can also be introduced in this area. The Main pulse will be wavefront shaped by a deformable mirror. The influence of spatial and temporal beam shaping has never been investigated for SHHG in the past and will open a new SHHG research domain. Furthermore, in this sub-system, the auxiliary laser beam is split off the Main beam before being spatially shaped, delayed or advanced with respect to the Main pulse with <10 fs precision over a 1 ns range.

Sub-system s3: Laser Diagnostics. This sub-system is dedicated to complete spatio-temporal characterization of the driving laser beam. Here, the Main and auxiliary laser beams are recombined to co-propagate side by side further into sub-system s4. The Main beam can once more be attenuated by a factor 10^2 or 10^4 for alignment and diagnostics purposes, before recombination. Insertable mirrors send the Main beam to a range of spatio-temporal diagnostics, section 3.5.4.

Sub-system s4: SHHG for generating XUV attosecond pulses. SHHG generation will occur within this sub-system by the interaction of the tightly focused Main beam on a polished solid target at 1 kHz repetition rate. Each pulse will hit an identical fresh spot on the target surface. The circular target will thus be rotated at high rotational speed, figure 27 and will generate high-order harmonics for at least an hour. This will be realized with a similar rotating target holder developed for the PM contrast cleaning in sub-system s1. However, the tight laser focusing and corresponding very short Rayleigh length needed for SHHG require that the rotating target's position normal to its surface needs to be actively stabilized with nanometer precision.

The beams Main and Aux.1 will be focused onto the target at 45° incidence by the same off-axis parabolic mirror. The ROM and CWE regimes of SHHG will be achieved in the same interaction chamber by changing the focusing geometry between f/1.5 and f/6 focusing i.e., using two different parabolic mirrors with different focal lengths with the same incoming Main beam diameter.

The plasma gradient scale length, controlled via the properties and the delay of the Aux.1 pulse preceding the Main pulse, will be measured with spatial domain interferometry (SDI) [148]. For this measurement, the Main pulse is transformed to a plasma expansion probe pulse by adding an intensity mask in the Main beam path prior to the focusing parabola. This mask is a simple blocker with periodic holes which causes a diffraction pattern in the focal plane. The spacing between the zero-order peak and the first-order ring is chosen so that only the former be reflected by the expanding plasma prepared by the Aux.1 pulse before and the latter provides a constant reference. This ultimately leads to intensity modulations in the Main beam far-field depending on the plasma gradient scale length and can be controlled by the Aux.1-Main delay and other parameters. These spatial intensity modulations thus allow retrieval of the shape of the plasma and its expansion velocity.

To capture the XUV spatial profile, an MCP and a phosphor screen assembly will be inserted directly into the beam path before the spectrometer grating. The phosphor screen signal will be imaged by another CCD camera. The XUV spectrum is measured at the end of sub-system s5.

Electron and ion diagnostics can be placed between the specular direction and the target normal and to a lesser extent between the specular direction and the target grazing direction.

A gold coated elliptical or toroidal mirror (100×282 mm^2) used at grazing incidence for broadband XUV reflectivity will image the XUV source (on the SHHG target surface) in a 2f–2f geometry onto an exit pinhole leading to sub-system s5. In order to enable both XUV–IR and XUV–XUV pump–probe schemes with attosecond resolution, the mirror is sub divided into a central (60-mm high) and an outer part which reflect XUV and IR light, respectively. The central component is further divided into an upper and a lower half, which can each be displaced, by piezoelectric elements, relative to one another and the outer part in the direction normal to the mirror surface with $\sim$100 nm precision.

Sub-system s5: Attosecond Diagnostics. This part of the beamline is dedicated to spatio-temporal and spectral characterization of the attosecond XUV pulses. It will provide UHV conditions and is connected to sub-system s4 via a millimeter-sized differential pumping pinhole placed around

Table 11. Targeted initial specifications for SHHG SYLOS development beamline.

Attosecond pulse specs	SYLOS Phase 1		SYLOS Phase 2	
	APT	SAP	APT	SAP
Spectral range[a]	8–40 eV	6–20 eV	8–60 eV	6–40 eV
Pulse energy at the SHHG source[a]	1–10 μJ	0.3–3 μJ	3–30 μJ	1–10 μJ
Pulse energy at the end station interaction region[a]	0.3–3 μJ	0.1–1 μJ	1–10 μJ	0.3–3 μJ
Pulse duration at the end station interaction region[a]	$<$10 fs	$<$1 fs	$<$5 fs	$<$1 fs
Spot size at the end station interaction region	$<$10 μm	$<$10 μm	$<$10 μm	$<$10 μm
Beam divergence emitted from SHHG source	$<$1 rad			
Polarization state	linear, horizontal			

[a] Estimations based on single-shot long-pulse high-energy laser experiments.

Table 12. Possible initial pump–probe combinations available for SHHG SYLOS development beamline.

Implemented pump–probe schemes				
	SYLOS Phase 1		SYLOS Phase 2	
	APT	SAP	APT	SAP
SHHG interaction region	IR—IR (Main–Aux.1)			
End station interaction region	XUV—IR (Atto–Aux.2)	XUV—IR (Atto–Aux.2)	XUV—IR (Atto–Aux.2)	XUV—IR (Atto–Aux.2)
End station interaction region	—	XUV–XUV (Atto–Atto in lighthouse mode)	—	XUV–XUV (Atto–Atto in lighthouse mode)

the intermediate XUV-source image created by the grazing incidence focusing mirror mentioned in subsection s4. A second mirror, identical to the previous focusing mirror without the split configuration, will create a second XUV source image further downstream where detectors can be suitably placed. A combined electron and ion TOF spectrometer and an ion microscope [149, 150] will be the default detectors placed in this sub-system for regular temporal and spatial characterization of the XUV pulses.

Attosecond temporal characterization of the SHHG will be performed either by using the FROG-CRAB (streaking) [151] or the PROOF [138] technique, using the electron TOF. An alternative approach for temporal metrology is single-shot autocorrelations using the technique described in [152] with the ion microscope. The XUV focal spot size and the peak intensity would be calibrated using the ion microscope [150].

At the end of this sub-system, an XUV spectrometer will be placed in the diverging XUV beam for an online measurement of the XUV spectrum. It will consist of an entrance slit, a flat field spherical XUV grating (1200 l/mm, 112 $\times$ 282 mm^2—suitable for several attosecond lighthouse beamlets) and an MCP with a phosphor screen assembly (10 $\times$ 10 cm^2). The signal on the phosphor screen will be imaged by a sensitive 12-bit CCD camera.

3.5.6. Initial specifications of SHHG SYLOS. Table 11 summarizes the initially targeted SHHG source parameters which will be further optimized and developed through additional R&D.

3.5.7. Pump–probe experiments with implementation phase beamline. The XUV attosecond beam parameters available during the initial phase of the SHHG SYLOS are expected to be sufficient to perform XUV pump and XUV probe experiments. Different pump–probe configurations are envisioned in view of diverse potential experiments [97] and also to develop a flexible beamline. Details about the pump–probe configurations which will be available in the SHHG SYLOS beamline are summarized in the table 12.

3.5.8. Conclusions. The new approach of creating and controlling plasma mirrors for SHHG provides opportunity for exciting new science, potential applications and also serious technological challenges to overcome. The unique properties of SHHG promises to generate extremely high intensity coherent attosecond XUV emission. This new intensity level in attosecond XUV pulses might open areas to explore the physics of XUV-XUV non-linear optics [97, 153] and ultrafast probing of superdense plasmas [98].

4. End stations

The spectral range and pulse parameters described in the previous sections will provide access to a range of dynamical processes, and to facilitate such measurements, different types of experimental end stations will be available at ELI-ALPS. Each beamline is equipped with a basic set of tools that are primarily used for pulse diagnostics, as previously described, but can equally well be applied to user experiments. These comprise micro-focusing units (for 6 μm spot diameters), effusive gas jets, cold particle beams, photoelectron and ion mass spectrometers (45° acceptance angle, 20–200 eV energy range, $<$1% resolution), photon spectrometers (VUV and XUV

spectral range, <0.2 nm resolution) and an ion microscope (spatial resolution of 1 μm). The instrument design permits flexibility in the choice of the photon source through compatibility with any of the XUV-D and CAMP chambers of the SYLOS beamlines or the CH-03 chambers of the HR beamlines. For more advanced experiments, ELI-ALPS will also maintain a range of specialized end stations, as described in the following.

4.1. Reaction microscope

The reaction microscope (ReMi, also known as *cold target recoil ion momentum spectrometer* COLTRIMS) permits the simultaneous correlated detection of positively and negatively charged photoreaction fragments [154]. It consists of a cold particle beam source, a 3D detector and mass spectrometer for ions and a 3D detector for electrons. Magnetic confinement is used to achieve a 4π collection solid angle up to 200 eV. As a result, experiments involving a single atom, molecule or cluster interacting with a definite number of photons can be realized. In this case, the momentum vector of all fragments can be reconstructed, providing full kinematic information about the photoreaction event [155]. A prominent example is the two-photon double ionization of He; a two-photon process that results in a doubly charged He ion and two photoelectrons that share the excess energy in a distinct manner depending on the pulse parameters. This energy sharing is a result of electron correlations during and after the two-photon absorption. In a similar manner, the doubly differential yield of the photodissociation of molecular hydrogen can provide full access to the freely evolving dynamics of the electronic and nuclear system of the molecule after photon interaction [156]. While these particular systems may be considered primarily of academic interest, they are highly significant and central to the modeling and interpretation of photoreactions in larger systems, e.g. multi-electron atoms and molecules. Non-linear experiments of this type [157, 158] require high peak intensities on the order of 10^{14} W cm^{-2}, variable pulse durations or pump–probe schemes and a controlled XUV photon energy range. This unique flexibility in pulse parameters will be provided by the SYLOS driven beamlines. The apparent limitation of the 1 kHz repetition rate resulting in longer acquisition times is offset by the high pulse-to-pulse and long-time stability of the photon sources. When the ReMi is attached to the HR beamlines, it will be able to harness the full potential of the 100 kHz pulse repetition rate to generate data with unprecedented levels of statistics. There is a strong emphasis on two-color XUV/IR/UV-VIS, IR multi-photon and strong-field interactions. These schemes can investigate the dynamics of molecular photodissociation in free [8] or in coupled (dressed) condition [159], charge migration and energy transport across molecules and culminate in charge directed reactivity and coherent control of photoreactions [160].

4.2. Condensed phase and surface science end station

Investigations of electronic processes in solids on the attosecond time scale have only recently begun [6, 41, 161, 162], but are expected to dramatically increase with the availability of suitable sources and instruments. At ELI-ALPS, there will be a powerful and versatile end station dedicated to ultrafast surface and bulk dynamics in condensed matter. Its central part will be a photoelectron emission microscope (PEEM) with enhanced lateral, energy, momentum and spin resolving capabilities. This device can operate in different modes: as a PEEM without energy resolution (<50 nm lateral resolution), an energy filtered PEEM (<50 meV resolution, 0–1800 eV range) alternatively with both electrostatic and TOF analyzers, an averaging or local photoelectron spectrometer, and as a momentum microscope (local ARPES) to map the *k*-space (10 m$\mathring{A}^{-1}$ resolution, 4 $\mathring{A}^{-1}$ range). To ensure reproducible and well controlled sample quality, the PEEM chamber is coupled to an *in situ* sample preparation and characterization unit. Common usages of this device are the selection of a specific location of a specimen from a 2–1000 μm region, the imaging of the near-surface morphology with optional chemical selectivity, the analysis of the chemical composition through the photoemission spectrum from a spatial region down to 80 nm, and the mapping of the band structure, all in a well controlled environment without disrupting the surface chemistry. All these measurements can also be time-resolved, and access to the dynamical properties of these quantities is again provided by various pump–probe schemes that become possible with the ELI-ALPS primary and secondary sources and their fine synchronization. This combination will permit the study of the dynamics of photoemission (tr-PE), electronic correlations and collective excitations, electron transport, transient and unoccupied states (tr-2PPE), band structures and molecular orbitals (tr-ARPES). An exciting aspect of the sub-fs time resolution is that processes can be observed before dephasing, scattering or breakdown become significant.

This end station, in combination with attosecond light pulses, is also a powerful tool to study electronic excitations and transport in plasmonic and excitonic nanostructures and interfaces. The high temporal and spatial resolution overcomes ensemble averaging and ultrafast dephasing, which are characteristic to these systems, and permits exploring possibilities to apply their ultrafast response to information processing applications. Other advanced opportunities for this end station can be found in strongly correlated systems, where photoinduced electronic phase transitions are predicted to proceed on the sub-fs time scale. In order to gain access to the spin degree of freedom—and thus to magnetisation dynamics—the end station can be equipped with a spin polarizer located just after the energy filter [163]. Moreover, it was recently demonstrated that the RABITT approach is also applicable to solid surfaces, e.g. for the analysis of photoemission delays [164]. At the future condensed matter end station of ELI-ALPS, similar measurements will be feasible with lateral, angular and spin resolution.

Narrow-band pulses in the few fs range (0.1–1 eV), described in section 3.2, will be available by spectral selection using a time-preserving monochromator. This, combined with the long wavelength IR-MIR-THz pulses, will permit selective addressing of the spin, electronic or nuclear sub-systems and investigating their couplings, thus

enabling full access to condensed matter science with the resources of ELI-ALPS.

4.3. Velocity map imaging spectrometers

The VMI spectrometer has become a standard tool in AMO science if information about the angular or momentum distribution of photo-ejected electrons or ions is required. The basic idea of the VMI is to measure the 3D velocity distribution of a charged particle from its 2D projection on an imaging detector. The standard design of a VMI was proposed in the 90s by Parker *et al* [165]; it consists of three electrodes creating an inhomogeneous electric field that accelerates charged particles (ions or electrons) towards a two dimensional position sensitive detector, usually composed of microchannel plates followed by a phosphor screen and a CCD camera. In its normal functioning mode, the three electrodes create an electrostatic potential that acts as a lens to focus the trajectories of particles having identical momentum on a specific position of the detector. This focusing effect requires that the energy acquired by the particle because of the electric field is much higher than its initial kinetic energy. In that case, the particles have ballistic trajectories, and there is a simple bijective relation between the 2D projection and the initial 3D momentum distribution. Optimal operation of a VMI spectrometer also requires that the particles are emitted from a small volume of typically 1 mm^3 size (interaction volume between the light and the target), above which the energy resolution is deteriorated. In usual 3D momentum spectroscopy, the 3D momentum components are extracted from three co-ordinates (for instance: the two position co-ordinates of the particle on the detector and its arrival time). In standard VMI spectrometry, one coordinate is lost due to the high electric field required for the projection (i.e. the arrival time is determined by the field strength, not by the initial momentum of the particle). However, by assuming that the momentum distribution has a cylindrical symmetry, it is possible to recover the 3D velocity distribution from its 2D projection. In practice, cylindrical symmetry can be assumed if the light polarization is linear and set parallel to the detector plane. Consequently, on the contrary to direct 3D spectrometry (such as reaction microscope) where each measured particle carries all information of its 3D momentum vector, in VMI, a large number of particles have to be recorded to access the entire projection and thereby allow momentum reconstruction. A number of algorithms (for example Abel Inversion, Onion Peeling and polynomial fitting procedure) accomplish this reconstruction of the momentum distribution with varying convergence efficiency and accuracy.

Other experimental approaches allow avoiding the 3D to 2D projection effect by recording the position and arrival time of the particle on a time resolving detector. This has been used both for ion and electron momentum measurement, and is known as 3D momentum imaging. One of the advantages of the VMI is its simplicity and versatility. It has a 4π collection efficiency, with equal detection efficiency for slow and high-energy particles. This means that is it better than usual spectrometry for phenomena where slow electrons (<eV) are involved. It can handle a large number of particles per shot when no coincidence mode is used (it can work in basic analog mode). The typical resolution $\Delta E/E$ is a few percent, and can be improved by using a series of additional electrostatic lenses, so that the particle energy range that the VMI can detect rises from a few meV up to keV. ELI-ALPS will host a VMI end station with two VMI spectrometers, one designed for low (eV) and the other for high (keV) energy charged particles. The installation will be combined with cold particle jets and high density effusive sources [166] operating in pulsed or continuous mode. These several configurations will be suited for 100 kHz (HR) and 1 kHz (SYLOS) beamlines. The VMI spectrometers will also be adaptable to the Mid-IR source.

The interest of measuring energy and angular distribution of electrons and ions in strong field and attosecond experiments is highlighted by the many results obtained in many labs all over the world, and arises from the fact that they deal with light electric fields with specific temporal structure and symmetries (linear, circular) that interact with quantum objects that themselves carry specific symmetries. As a result, the output of a reaction carries specific angular distributions and energy structures. To mention a few examples, ion angular distribution was used to reveal attosecond coherent control of molecular dissociation and charge localization using CEP stable pulses or two-color XUV-IR attosecond pulse schemes. Electron measurements were used to extract phase information of electron wavepackets or record complex interference patters arising from scattering, holographic or diffraction processes. In combination with VMI spectroscopy, ELI-ALPS' attosecond beamlines will allow similar experiments to be carried out on much more complex—and a larger variety of—targets, including biomolecules, nanoparticles, clusters and molecular assemblies.

4.4. Magnetic bottle electron spectrometer

Non-linear photo effects are weak processes, and despite the high peak intensities of the ELI-ALPS XUV sources, care must be taken to collect the photoelectrons efficiently, with the lowest possible noise and the highest possible resolution. These requirements can be simultaneously fulfilled by a magnetic bottle TOF [167]. This consists of a high-resolution TOF spectrometer combined with a strong, inhomogeneous magnetic field in the interaction region for collimation and a low magnetic field in the drift region for guidance of the electron trajectories. As a result, a collection solid angle of π and an energy resolution around 0.1% are achieved. Correlated photoelectron detection is conceivable on the SYLOS beamlines with a real-time readout. Another advantage is that the interaction region can be free of electric fields, which permits the undisturbed observation of field-sensitive processes. This instrument will facilitate dynamical studies of above-threshold ionization, autoionization and interatomic Coulomb decay in clusters and molecules.

5. Conclusions

The primary, secondary sources and end stations that will be available at the ELI-ALPS international facility have been presented. The unique characteristics of the laser sources will enable the beamlines to scale the characteristics of attosecond pulses generated in gases at an unprecedented level of intensity for high repetition rates (>1 kHz). The availability of different beamlines will secure reliable operation for user experiments whilst generating the possibility to test new technological solutions for advancing the characteristics of attosecond pulses, in terms of pulse energy and duration. Novel solutions for the generation of highly intense attosecond pulses will be explored using harmonic generation from surfaces. The presence of permanent end stations will make it possible to extend attosecond spectroscopy to systems of increasing complexity and will give the opportunity to access challenging attosecond technology to a large scientific community.

Acknowledgments

This project has received also funding from the European Union's Horizon 2020 research and innovation programme under the Marie Sklodowska-Curie grant agreement no. 641789 MEDEA. The researchers from Lund University acknowledge partial support from the Swedish Research Council, the Swedish Foundation for Strategic Research, and the European Research Council (PALP). ELI-ALPS is supported by the European Union and co-financed by the European Regional Development Fund (GINOP-2.3.6-15-2015-00001). We acknowledge funding from the ERC Starting Research Grant UDYNI (grant agreement no. 307964, EC Seventh Framework Programme), ERC grant STARLIGHT (no. 637756) and from the Italian Ministry of Research and Education (ELI project - ESFRI Roadmap).

ORCID

Michele Devetta https://orcid.org/0000-0002-3806-3475
Erik Månsson https://orcid.org/0000-0003-3567-2985
Caterina Vozzi https://orcid.org/0000-0002-0212-0191
Sylvain Maclot https://orcid.org/0000-0001-5587-7182

References

[1] Stillman J D B, Muybridge E and Stanford L 1882 *The Horse in Motion* (Boston, MA: J R Osgood)
[2] Zewail A H 2000 *Angew. Chem. Int. Ed.* **39** 2586–631
[3] Krausz F and Ivanov M 2009 *Rev. Mod. Phys.* **81** 163–234
[4] Drescher M, Hentschel M, Kienberger R, Uiberacker M, Yakovlev V, Scrinzi A, Westerwalbesloh T, Kleineberg U, Heinzmann U and Krausz F 2002 *Nature* **419** 803–7
[5] Sansone G *et al* 2010 *Nature* **465** 763–6
[6] Cavalieri A L *et al* 2007 *Nature* **449** 1029–32
[7] Schultze M *et al* 2010 *Science* **328** 1658–62
[8] Calegari F *et al* 2014 *Science* **346** 336–9
[9] Kraus P M *et al* 2015 *Science* **350** 790–5
[10] Schiffrin A *et al* 2013 *Nature* **493** 70–4
[11] Chang Z, Corkum P B and Leone S R 2016 *J. Opt. Soc. Am.* B **33** 1081–97
[12] Calegari F, Sansone G, Stagira S, Vozzi C and Nisoli M 2016 *J. Phys. B: At. Mol. Opt. Phys.* **49** 062001
[13] Limpert J *et al* 2005 *Opt. Expr.* **13** 1055–8
[14] Limpert J, Stutzki F, Jansen F, Otto H-J, Eidam T, Jauregui C and Tünnermann A 2012 *Light Sci. Appl.* **1** e8
[15] Seise E, Klenke A, Limpert J and Tünnermann A 2010 *Opt. Exp.* **18** 27827–35
[16] Nisoli M, Stagira S, De Silvestri S, Svelto O, Sartania S, Cheng Z, Lenzner M, Spielmann C and Krausz F 1997 *Appl. Phys.* B **65** 189–96
[17] Hädrich S *et al* 2016 *Opt. Lett.* **41** 4332–5
[18] Eidam T, Hoffmann A, Hädrich S, Rothhardt J, Varállyay Z, Osvay K, Tünnermann A and Limpert J 2016 Concept for cep-stable few-cycle pulses at 100 W average power *In High-Brightness Sources and Light-Driven Interactions* OSA Technical Digest (online) page HS3B.3. Optical Society of America (https://doi.org/10.1364/HILAS.2016.HS3B.3)
[19] Zou J P *et al* 2015 *High Power Laser Sci. Eng.* **3** e2
[20] Kalashnikov M, Cao H, Osvay K and Chvykov V 2016 *Opt. Lett.* **41** 25–8
[21] Chvykov V, Nagymihaly R S, Cao H, Kalashnikov M and Osvay K 2016 *Opt. Exp.* **24** 3721–33
[22] Chvykov V, Cao H, Nagymihaly R, Kalashnikov M P, Khodakovskiy N, Glassock R, Ehrentraut L, Schnuerer M and Osvay K 2016 *Opt. Lett.* **41** 3017–20
[23] Shiner A D *et al* 2013 *J. Mod. Opt.* **60** 1458–65
[24] Rudawski P *et al* 2013 *Rev. Sci. Instrum.* **84** 073103
[25] Boutu W *et al* 2011 *Phys. Rev.* A **84** 063406
[26] Hergott J-F, Kovacev M, Merdji H, Hubert C, Mairesse Y, Jean E, Breger P, Agostini P, Carré B and Saliéres P 2002 *Phys. Rev.* A **66** 021801
[27] The Scientific Case of ELI-ALPS 2015, http://eli-hu.hu/?q=en/node/248 (Accessed 17 August 2016)
[28] Helml W *et al* 2014 *Nat. Photonics* **8** 950–7
[29] Allaria E, Callegari C, Cocco D, Fawley W M, Kiskinova M, Masciovecchio C and Parmigiani F 2010 *New J. Phys.* **12** 075002
[30] Ferrari E *et al* 2016 *Nat. Commun.* **7** 10343
[31] Tanaka T 2013 *Phys. Rev. Lett.* **110** 084801
[32] Prat E, Löhl F and Reiche S 2015 *Phys. Rev. ST Accel. Beams* **18** 100701
[33] Sansone G *et al* 2006 *Science* **314** 443–6
[34] Zhao K, Zhang Q, Chini M, Wu Y, Wang X and Chang Z 2012 *Opt. Lett.* **37** 3891–3
[35] Takahashi E J, Lan P, Mücke O D, Nabekawa Y and Midorikawa K 2013 *Nat. Commun.* **4** 2691
[36] Feldhaus J, Krikunova M, Meyer M, Möller T, Moshammer R, Rudenko A, Tschentscher T and Ullrich J 2013 *J. Phys. B: At. Mol. Opt. Phys.* **46** 164002–19
[37] Mücke O D *et al* 2015 *IEEE J. Sel. Top. Quantum Electron.* **21** 1–12
[38] Yoshii K, Kiran A J and Katsuragawa M 2013 *Light Sci. Appl.* **2** e58
[39] Baker S, Walmsley I A, Tisch J W G and Marangos J P 2011 *Nat. Photon.* **5** 664–71
[40] Ghimire S, Ndabashimiye G, Di Chiara A D, Sistrunk E, Stockman M I, Agostini P, Di Mauro L F and Reis D A 2014 *J. Phys. B: At. Mol. Opt. Phys.* **47** 204030
[41] Luu T T, Garg M, Kruchinin S Y, Moulet A, Hassan M T and Goulielmakis E 2015 *Nature* **521** 498–502
[42] Takahashi E J, Hasegawa H, Nabekawa Y, Nagata Y and Midorikawa K 2004 High-throughput, high-damage-threshold broadband beam splitter for high-order harmonics

Conf. on Lasers and Electro-Optics/International Quantum Electronics Conf. and Photonic Applications Systems Technologies Technical Digest (CD) pages JMD3–. Optical Society of America
[43] Sola I J *et al* 2006 *Nat. Phys.* **2** 319–22
[44] Peatross J, Chaloupka J L and Meyerhofer D D 1994 *Opt. Lett.* **19** 942–4
[45] Poletto L, Tondello G and Villoresi P 2001 *Rev. Sci. Instrum.* **72** 2868–74
[46] Poletto L, Tondello G and Villoresi P 2003 *Appl. Opt.* **42** 6367–73
[47] Poletto L, Bonora S, Pascolini M and Villoresi P 2004 *Rev. Sci. Instrum.* **75** 4413–8
[48] Stefan Kaesdorf GmbH, http://kaesdorf.de/electrontof.html
[49] Poletto L, Frassetto F, Calegari F, Anumula S, Trabattoni A and Nisoli M 2013 *Opt. Expr.* **21** 13040–51
[50] Kim K T, Zhang C, Shiner A D, Schmidt B E, Légaré F, Villeneuve D M and Corkum P B 2013 *Nat. Photon.* **7** 958–62
[51] Poletto L and Frassetto F 2010 *Appl. Opt.* **49** 5465–73
[52] Poletto L, Frassetto F and Villoresi P 2012 *IEEE J. Sel. Top. Quantum Electron.* **18** 467–78
[53] Poletto L, Villoresi P, Frassetto F, Calegari F, Ferrari F, Lucchini M, Sansone G and Nisoli M 2009 *Rev. Sci. Instrum.* **80** 123109
[54] Poletto L and Villoresi P 2006 *Appl. Opt.* **45** 8577–85
[55] Pascolini M, Bonora S, Giglia A, Mahne N, Nannarone S and Poletto L 2006 *Appl. Opt.* **45** 3253–62
[56] Mc Pherson A, Gibson G, Jara H, Johann U, Luk T S, McIntyre I A, Boyer K and Rhodes C K 1987 *J. Opt. Soc. Am.* B **4** 595–601
[57] Ferray M, L'Huillier A, Li X F, Lompre L A, Mainfray G and Manus C 1988 *J. Phys. B: At. Mol. Opt. Phys.* **21** L31–5
[58] Kazamias S, Weihe F, Douillet D, Valentin C, Planchon T, Sebban S, Grillon G, Augé F, Hulin D and Balcou P 2002 *Eur. Phys. J.* D **21** 353–9
[59] Takahashi E, Nabekawa Y, Otsuka T, Obara M and Midorikawa K 2002 *Phys. Rev.* A **66** 021802(R)
[60] Skantzakis E, Tzallas P, Kruse J, Kalpouzos C and Charalambidis D 2009 *Opt. Lett.* **34** 1732–4
[61] Dahlström J M, Fordell T, Mansten E, Ruchon T, Swoboda M, Klünder K, Gisselbrecht M, L'Huillier A and Mauritsson J 2009 *Phys. Rev.* A **80** 033836
[62] Kruse J E, Tzallas P, Skantzakis E, Kalpouzos C, Tsakiris G D and Charalambidis D 2010 *Phys. Rev.* A **82** 021402
[63] Constant E, Garzella D, Breger P, Mével E, Dorrer C, Le Blanc C, Salin F and Agostini P 1999 *Phys. Rev. Lett.* **82** 1668–71
[64] Takahashi E J, Nabekawa Y, Mashiko H, Hasegawa H, Suda A and Midorikawa K 2004 *IEEE J. Sel. Top. Quantum Electron.* **10** 1315–28
[65] Krause J L, Schafer K J and Kulander K C 1992 *Phys. Rev.* A **45** 4998–5010
[66] Krause J L, Schafer K J and Kulander K C 1992 *Phys. Rev. Lett.* **68** 3535–8
[67] Gaarde M B and Schafer K J 2002 *Phys. Rev. Lett.* **89** 213901
[68] Seres J, Yakovlev V S, Seres E, Streli C, Wobrauschek P, Spielmann C and Krausz F 2007 *Nat. Phys.* **3** 878–83
[69] Willner A *et al* 2011 *Phys. Rev. Lett.* **107** 175002
[70] Corkum P B, Burnett N H and Ivanov M Y 1994 *Opt. Lett.* **19** 1870–2
[71] Kolliopoulos G, Carpeggiani P A, Rompotis D, Charalambidis D and Tzallas P 2012 *Rev. Sci. Instrum.* **83** 063102
[72] Chang Z 2007 *Phys. Rev.* A **76** 051403(R)
[73] Tzallas P, Charalambidis D, Papadogiannis N A, Witte K and Tsakiris G D 2003 *Nature* **426** 267–71
[74] Nikolopoulos L A A, Benis E P, Tzallas P, Charalambidis D, Witte K and Tsakiris G D 2005 *Phys. Rev. Lett.* **94** 113905
[75] Paul P M, Toma E S, Breger P, Mullot G, Auge F, Balcou P, Muller H G and Agostini P 2001 *Science* **292** 1689–92
[76] Kienberger R *et al* 2002 *Science* **297** 1144–8
[77] Heyl C M, Güdde J, L'Huillier A and Höfer U 2012 *J. Phys. B: At. Mol. Opt. Phys.* **45** 074020
[78] Heyl C M *et al* 2016 *Optica* **3** 75–81
[79] Takahashi E, Nabekawa Y and Midorikawa K 2002 *Opt. Lett.* **27** 1920–2
[80] Manschwetus B *et al* 2016 *Phys. Rev.* A **93** 061402R
[81] Vincenti H and Quéré F 2012 *Phys. Rev. Lett.* **108** 113904
[82] Heyl C M, Bengtsson S N, Carlström S, Mauritsson J, Arnold C L and L'Huillier A 2014 *New J. Phys.* **16** 052001
[83] Brizuela F, Heyl C M, Rudawski P, Kroon D, Rading L, Dahlström J M, Mauritsson J, Johnsson P, Arnold C L and L'Huillier A 2013 *Sci. Rep.* **3** 1410
[84] Paul A, Bartels R A, Tobey R, Green H, Weiman S, Christov I P, Murnane M M, Kapteyn H C and Backus S 2003 *Nature* **421** 51–4
[85] Ferrari F, Calegari F, Lucchini M, Vozzi C, Stagira S, Sansone G and Nisoli M 2010 *Nat. Photon.* **4** 875–9
[86] Campi F, Coudert-Alteirac H, Miranda M, Rading L, Manschwetus B, Rudawski P, L'Huillier A and Johnsson P 2016 *Rev. Sci. Instrum.* **87** 023106
[87] López-Martens R *et al* 2005 *Phys. Rev. Lett.* **94** 033001
[88] Strueder L *et al* 2010 *Nucl. Instr. Meth. Phys. Res.* **614** 483–96
[89] Dromey B *et al* 2006 *Nat. Phys.* **2** 456–9
[90] Quéré F, Thaury C, Monot P, Dobosz S, Martin P, Geindre J-P and Audebert P 2006 *Phys. Rev. Lett.* **96** 125004
[91] Vincenti H, Monchocé S, Kahaly S, Bonnaud G, Martin P and Quéré F 2014 *Nat. Comm.* **5** 3403
[92] Kahaly S, Monchocé S, Vincenti H, Dzelzainis T, Dromey B, Zepf M, Martin P and Quéré F 2013 *Phys. Rev. Lett.* **110** 175001
[93] Nomura Y *et al* 2009 *Nat. Phys.* **5** 124–8
[94] Wheeler J, Borot A, Monchocé S, Vincenti H, Ricci A, Malvache A, Lopez-Martens R and Quéré F 2012 *Nat. Photon.* **6** 829–33
[95] Yeung M *et al* 2014 *Phys. Rev. Lett.* **112** 123902
[96] Yeung M *et al* 2015 *Phys. Rev. Lett.* **115** 193903
[97] Reduzzi M *et al* 2015 *J. Electron. Spectrosc. Relat. Phenom.* **204** 257–68
[98] Leblanc A, Monchocé S, Bourassin-Bouchet C, Kahaly S and Quéré F 2015 *Nat. Phys.* **12** 301–5
[99] Borot A, Malvache A, Chen X, Jullien A, Geindre J-P, Audebert P, Mourou G, Quéré F and Lopez-Martens R 2012 *Nat. Phys.* **8** 416–21
[100] Lévy A *et al* 2007 *Opt. Lett.* **32** 310–2
[101] Thaury C *et al* 2007 *Nat. Phys.* **3** 424–9
[102] Thaury C and Quéré F 2010 *J. Phys. B: At. Mol. Opt. Phys.* **43** 213001
[103] Teubner U and Gibbon P 2009 *Rev. Mod. Phys.* **81** 445–79
[104] Von Der Linde D and Rzazewski K 1996 *Appl. Phys.* B **506** 499–506
[105] Baeva T, Gordienko S and Pukhov A 2006 *Phys. Rev.* E **74** 1–11
[106] Drake R P 2006 *High-Energy-Density Physics: Fundamentals, Inertial Fusion, and Experimental Astrophysics* (Berlin: Springer)
[107] Remington B A 2005 *Plasma Phys. Control. Fusion* **47** A191–203
[108] Kahaly S, Mondal S, Kumar G R, Sengupta S, Das A and Kaw P K 2009 *Phys. Plasmas* **16** 043114
[109] Mondal S *et al* 2012 *Proc. Natl Acad. Sci.* **109** 8011–5
[110] Thévenet M, Leblanc A, Kahaly S, Vincenti H, Vernier A, Quéré F and Faure J 2015 *Nat. Phys.* **12** 355–60

[111] Bocoum M, Thévenet M, Böhle F, Beaurepaire B, Vernier A, Jullien A, Faure J and Lopez-Martens R 2016 *Phys. Rev. Lett.* **116** 185001
[112] Kahaly S, Yadav S K, Wang W M, Sengupta S, Sheng Z M, Das A, Kaw P K and Kumar G R 2008 *Phys. Rev. Lett.* **101** 145001
[113] Mondal S *et al* 2011 *Phys. Rev.* B **83** 035408
[114] Hamster H, Sullivan A, Gordon S, White W and Falcone R W 1993 *Phys. Rev. Lett.* **71** 2725–8
[115] Liao G-Q, Li Y-T, Li C, Mondal S, Hafez H A, Fareed M A, Ozaki T, Wang W-M, Sheng Z-M and Zhang J 2016 *Phys. Plasmas* **23** 013104
[116] Malvache A, Borot A, Quéré F and Lopez-Martens R 2013 *Phys. Rev.* E **87** 035101
[117] Dromey B *et al* 2007 *Phys. Rev. Lett.* **99** 085001
[118] Mourou G, Tajima T and Bulanov S 2006 *Rev. Mod. Phys.* **78** 309–71
[119] Bulanov S V, Naumova N M and Pegoraro F 1994 *Phys. Plasmas* **1** 745
[120] Lichters R, Meyer ter Vehn J and Pukhov A 1996 *Phys. Plasmas* **3** 3425
[121] Paul A, Gibson E A, Zhang X, Lytle A, Popmintchev T, Zhou X, Murnane M M, Christov I P and Kapteyn H C 2006 *IEEE J. Quantum Electron.* **42** 14–26
[122] Shiner A D, Trallero-Herrero C, Kajumba N, Bandulet H-C, Comtois D, Légaré F, Giguère M, Kieffer J-C, Corkum P B and Villeneuve D M 2009 *Phys. Rev. Lett.* **103** 073902
[123] Balcou P, Saliéeres P, L'Huillier A and Lewenstein M 1997 *Phys. Rev.* A **55** 3204–10
[124] Kazamias S, Douillet D, Weihe F, Valentin C, Rousse A, Sebban S, Grillon G, Augé F, Hulin D and Balcou P 2003 *Phys. Rev. Lett.* **90** 193901
[125] Chang Z 2011 *Fundamentals of Attosecond Optics* (Boca Raton, FL: CRC Press)
[126] Dubrouil A, Hort O, Catoire F, Descamps D, Petit S, Mével E, Strelkov V V and Constant E 2014 *Nat. Comm.* **5** 4637
[127] Corkum P B and Krausz F 2007 *Nat. Phys.* **3** 381–7
[128] Smirnova O, Mairesse Y, Patchkovskii S, Dudovich N, Villeneuve D, Corkum P and Ivanov M Y 2009 *Nature* **460** 972–7
[129] Quéré F, Thaury C, Geindre J P, Bonnaud G, Monot P and Martin P 2008 *Phys. Rev. Lett.* **100** 095004
[130] Dromey B *et al* 2009 *Nat. Phys.* **5** 146–52
[131] Dollar F, Cummings P, Chvykov V, Willingale L, Vargas M, Yanovsky V, Zulick C, Maksimchuk A, Thomas A G R and Krushelnick K 2013 *Phys. Rev. Lett.* **110** 175002
[132] Kahaly S, Monchocé S, Gallet V, Gobert O, Réau F, Tcherbakoff O, D'Oliveira P, Martin P and Quéré F 2014 *Appl. Phys. Lett.* **104** 054103
[133] Carman R L, Rhodes C K and Benjamin R F 1981 *Phys. Rev.* A **24** 2649–63
[134] Antoine P, L'Huillier A and Lewenstein M 1996 *Phys. Rev. Lett.* **77** 1234–7
[135] Monchocé S, Kahaly S, Leblanc A, Videau L, Combis P, Réau F, Garzella D, D'Oliveira P, Martin P and Quéré F 2014 *Phys. Rev. Lett.* **112** 145008
[136] Geissler M, Rykovanov S, Schreiber J, Meyer ter Vehn J and Tsakiris G D 2007 *New J. Phys.* **9** 218
[137] Quéré F *et al* 2014 *J. Phys. B: At. Mol. Opt. Phys.* **47** 124004
[138] Chini M, Gilbertson S, Khan S D and Chang Z 2010 *Opt. Expr.* **18** 13006–16
[139] Itatani J, Quéré F, Yudin G, Ivanov M, Krausz F and Corkum P 2002 *Phys. Rev. Lett.* **88** 173903
[140] Frühling U, Wieland M and Gensch M 2009 *Nat. Photon.* **3** 523–8
[141] Ardana-Lamas F, Erny C, Stepanov A G, Gorgisyan I, Juranić P, Abela R and Hauri C P 2016 *Phys. Rev.* A **93** 043838
[142] Bourassin-Bouchet C, Mang M M, Delmotte F, Chavel P and De Rossi S 2013 *Opt. Expr.* **21** 2506–20
[143] Borot A, Douillet D, Iaquaniello G, Lefrou T, Audebert P, Geindre J P and Lopez-Martens R 2014 *Rev. Sci. Instrum.* **85** 013104
[144] Miranda M, Arnold C L, Fordell T, Silva F, Alonso B, Weigand R, L'Huillier A and Crespo H 2012 *Opt. Express* **20** 18732–43
[145] Pariente G, Gallet V, Borot A, Gobert O and Quéré F 2016 *Nat. Photon.* **10** 547–53
[146] Witting T, Austin D R and Walmsley I A 2009 *Opt. Lett.* **34** 881–3
[147] Dromey B, Kar S, Zepf M and Foster P 2004 *Rev. Sci. Instrum.* **75** 645–9
[148] Bocoum M, Böhle F, Vernier A, Jullien A, Faure J and Lopez-Martens R 2015 *Opt. Lett.* **40** 3009–12
[149] Schultze M, Bergues B, Schröder H, Krausz F and Kompa K L 2011 *New J. Phys.* **13** 033001
[150] Tsatrafyllis N *et al* 2016 *Sci. Rep.* **6** 21556
[151] Quéré F, Mairesse Y and Itatani J 2005 *J. Mod. Opt.* **52** 339–60
[152] Kolliopoulos G, Tzallas P, Bergues B, Carpeggiani P A, Heissler P, Schröder H, Veisz L, Charalambidis D and Tsakiris G D 2014 *J. Opt. Soc. Am.* B **31** 926–38
[153] Sansone G, Poletto L and Nisoli M 2011 *Nat. Photon.* **5** 655–63
[154] Rudenko A *et al* 2010 *J. Phys. B: At. Mol. Opt. Phys.* **43** 194004
[155] Ullrich J, Moshammer R, Dorn A, Dörner R, Schmidt L P H and Schmidt-Böcking H 2003 *Rep. Prog. Phys.* **66** 1463–545
[156] Palacios A, Gonzalez-Castrillo A and Martin F 2014 *Proc. Natl Acad. Sci.* **111** 3973–8
[157] Palacios A, Horner D A, Rescigno T N and McCurdy C W 2010 *J. Phys. B: At. Mol. Opt. Phys.* **43** 194003
[158] Feist J, Nagele S, Pazourek R, Persson E, Schneider B I, Collins L A and Burgdoerfer J 2009 *Phys. Rev. Lett.* **103** 063002
[159] Chini M, Wang X, Cheng Y, Wu Y, Zhao D, Telnov D A, Chu S-I and Chang Z 2013 *Sci. Rep.* **3** 1105
[160] Sansone G, Calegari F and Nisoli M 2014 Electron localization in hydrogen *Progress in Ultrafast Intense Laser Science* (*Springer Series in Chemical Physics*) ed K Yamanouchi, G G Paulus and D Mathur vol 106 (Basel: Springer) pp 17–32
[161] Neppl S *et al* 2015 *Nature* **517** 342–6
[162] Chew S H *et al* 2012 *Appl. Phys. Lett.* **100** 051904
[163] Tusche C, Ellguth M, Krasyuk A, Winkelmann A, Kutnyakhov D, Lushchyk P, Medjanik K, SchÃnhense G and Kirschner J 2013 *Ultramicroscopy* **130** 70–6
[164] Locher R, Castiglioni L, Lucchini M, Greif M, Gallmann L, Osterwalder J, Hengsberger M and Keller U 2015 *Optica* **2** 405–10
[165] Eppink A T J B and Parker D H 1997 *Rev. Sci. Instrum* **68** 3477–84
[166] Ghafur O, Siu W, Johnsson P, Kling M F, Drescher M and Vrakking M J J 2009 *Rev. Sci. Instrum.* **80** 033110
[167] Zhang Q, Zhao K and Chang Z 2014 *J. Electron. Spectrosc. Relat. Phenom.* **195** 48–54